AFOSR 67-1581

CRUSTAL STUDIES

CONTINUATION OF BASIC RESEARCH IN CRUSTAL STUDIES

FINAL REPORT

Max K. Miller, Project Scientist
FL 7-5411, Ext. 317

A. Frank Linville   Hugh K. Harris

TEXAS INSTRUMENTS INCORPORATED
Science Service Division
P. O. Box 5621
Dallas. Texas 75222

Contract No.: AF 49(638)-1588
Date of Contract: 1 January 1966
Contract Expiration Date: 31 May 1967
Amount of Contract: $110,420.00

Prepared for

AIR FORCE OFFICE OF SCIENTIFIC RESEARCH (SRPG)
1400 Wilson Boulevard
Arlington, Virginia 22209

Sponsored by

ADVANCED RESEARCH PROJECTS AGENCY
ARPA Order No. 292, Amendment 20
Project Code No. 8652

15 July 1967

CRUSTAL STUDIF,

CONTINUATION OF BASIC RESEARCH IN CRUSTAL STUDIES

FINAL REPORT

Max K. Miller, Project Scientist
FL 7-5411, Ext. 317

A. Frank Linville   Hugh K. Harris

science services division

Requests for additional copies by agencies of the Department of Defense, their contractors, or other government agencies should be directed to

DEFENSE DOCUMENTATION CENTER (DDC)
CAMERON STATION
ALEXANDRIA, VIRGINIA 22314

Department of Defense contractors must be established by the cognizant military agency of their project or contract.

All other persons and organizations should apply to the

Clearinghouse for Federal Scientific and
Technical Information (CFSTI)
Sills Building
5285 Port Royal Road
Springfield, Virginia 22151

science services division

ABSTRACT

The final report of work performed under the Crustal Studies Contract AF 49(638)-1588 is divided into two main areas: (1) theoretical dispersion calculations and experimental measurements of the fundamental Rayleigh wave at the Large Aperture Seismic Array (LASA) in Montana, and (2) a study of teleseismic signals using analog model data.

Two earthquakes, recorded on the long-period seismometers at LASA, were used for dispersion analysis. Epicenters of these two events were located off the northern California coast and in the Greenland Sea.

Good agreement in the dispersion estimates was obtained using three recording stations. The significance of the results, which covered a frequency band of 0.025 through 0.0625 cps, lies in the fact that this frequency band is, theoretically, where the greatest dispersion occurs. The results obtained agree qualitatively with previously known results.

An analog model having a crustal layer with an abrupt thickness change (3 to 5 cm) was used for studies of surface-wave scattering from surface irregularities and a lateral inhomogeneity. The analysis of surface-wave scattering was a continuation of work previously done.

The model also was used for a study of teleseismic signals by placing the source crystal on the bottom of the model.

For an upcoming-plane P wave, reverberation effects, the lateral inhomogeneity (including the expected focusing of energy into the thick end by the dipping segment of the crustal layer), and P- and S-wave conversions at the crustal layer interface caused a complex interference pattern that was observed on the surface recordings.

The principal investigator for this contract was

Milo M Backus

The principal authors are

Max K. Miller
Hugh K. Harris
A. Frank Linville

TABLE OF CONTENTS

APPENDIX

SUMMARY OF CRUSTAL STUDIES ANNUAL REPORT,
JANUARY 1967

LIST OF ILLUSTRATIONS

science services division

LIST OF ILLUSTRATIONS (CONTD)

LIST OF TABLES

SECTION I
SUMMARY

This final report of the work performed under the Crustal Studies Contract AF 49(638)-1588 is divided into two main areas: (1) theoretical dispersion calculations and experimental measurements of the fundamental Rayleigh wave at the Large Aperture Seismic Array (LASA) in Montana, and (2) a study of teleseismic signals using analog model data. Primarily covered in this report is work not discussed in the Crustal Studies Annual Report (January 1967);[1] however, the summary of the annual report is contained in the Appendix.

A. DISPERSION ESTIMATES

Two earthquake recordings on long-period seismometers at LASA were used for dispersion analysis. The epicenter of one event was located off the coast of northern California and has an epicentral distance of about 1800 km; the epicenter of the other event was located in the Greenland Sea and has an epicentral distance of approximately 5000 km. The vertical component of motion was used to estimate dispersion. By time-partitioning the Rayleigh-wave portion of the seismograms and computing transfer functions between pairs of stations (seismometers), the phase velocity of the fundamental Rayleigh mode was determined. Dispersion results obtained using pairs of stations showed large variations.

To improve the dispersion estimates, three recording stations were used so that the direction of propagation of the surface wavefront need not be known exactly. The variation in dispersion estimates obtained from several three-seismometer sets was greatly reduced for both events, compared to the two-station results. There was approximately a 4-percent variation of the phase velocities computed from both events, using the triangulation system.

science services division

For the California event, seismometer stations were selected so that independent measurements could be made for LASA-north and LASA-south. The dispersion results showed a lower velocity at 0.0625 cps, the highest calculated frequency, for LASA-south than for LASA-north.

The variation in the propagation vectors at different stations agreed closely with that expected from a wavefront originating in Northern California.

Propagation vectors computed using the Greenland event showed a wider spread than those computed from the California event. This was partly due to the fact that the propagation vector was close to one leg of the triangle used — a poor arrangement for computing the angle of the propagation vector.

The experimentally determined propagation vector of the California event differed from the assumed great-circle azimuth by approximately 5°. The importance of the three-station estimates is noted; and the relatively poor results of the two-station estimates are attributed to an uncertainty in the direction of wavefront propagation.

The results obtained from the two events agree qualitatively with those of Steinhart and Meyer.[2] After the dispersion estimates were made using three recording stations, the LASA crustal model was perturbed to obtain better agreement between theory and experimental dispersion data. The model perturbed was based on measurements of Steinhart and Meyer. The results obtained cover a frequency band of 0.025 through 0.0625 cps. Theory predicts that the greatest dispersion for the fundamental Rayleigh mode can be observed in this band, and tl.us some significance can be attached to the results.

By using more events, phase velocity estimateions can be made to give a more detailed analysis of LASA. A contour map of LASA, made with velocities computed using a tripartite system of recording, could be constructed for all of LASA. A complete crustal model for LASA then could be obtained by inversion of the dispersion results. This is recommended for a future study.

B. ANALOG MODEL STUDIES

An analog model having a crustal layer with an abrupt thickness change (transition zone) was used to perform scattering studies. Data was recorded (along the top of the model) with the source located on the surface of the thick (5-cm) end of the model. Theoretical travel times were computed and compared to measured values obtained from the records.

Some refinements were made in the analysis performed on the recorded data using surface scatterers.[1] For this experimental setup, two small brass scatterers were used. Each scatterer was centered on the thin (3-cm) end of the analog model, which became, in effect, a single layer with a surface irregularity over a half-space.

Vertical recordings were made along the surface of the model with each scatterer in position. Wide-band velocity filtering results showed that the only observable scattered energy from the incident Rayleigh wave was a backscattered Rayleigh pulse. Power spectra were computed for the incident Rayleigh and backscattered Rayleigh waves. The values of power spectra of the backscattered energy were typically 18 to 36 db below the values of the incident energy.

Transfer functions which change the incident Rayleigh energy into backscattered energy were computed for each scatterer. The transfer functions indicate that higher frequencies interact more with the scatterers than do low frequencies.

science services division

The effect of a lateral inhomogeneity in a layered crust on an upcoming plane P wave was studied by attaching the source crystal to the bottom of the analog model. Horizontal and vertical recordings were made along a 40-cm interval on the surface of the model. The recordings were made 20-cm each side of the transition zone's center. Theoretical travel times were computed for several arrivals and compared with measured values.

The effects of the lateral inhomogeneity on the upcoming wave were observed on the output records. This complex interference pattern includes the expected focusing of energy into the thick end by the dipping segment of the brass layer, P- and S-wave conversions at the crustal layer interface, and reverberation effects.

Theoretical horizontal and vertical amplitude spectra for surface displacements were computed for an upcoming plane P wave for two mathematical models. The models used were for a layer over a half-space and correspond to the thick (5-cm) and thin (3-cm) ends of model H-6. Calculations were made for phase velocities of 25.10, 33.15, 49.39, and 98.38 mm/μsec. Seismograms for each layer thickness (3 cm or 5 cm) and for each phase velocity were obtained by Fourier transforming the amplitude spectra.

Comparisons were made between the theoretically computed spectra and experimental spectra. Two difficulties occurred in attempting this comparison. First, the experimental-source spectrum was very narrow-band, so one would expect to see only two or three peaks in the frequency band where energy was present. Second, the source spectrum was highly peaked, making it difficult to determine if the peaks were due to the shape of the source spectrum or to the layering effect.

To obtain a more realistic comparison between theory and experiment, the theoretical spectra were shaped with the P pulse observed in the steel half-space of the model. The theoretical vertical spectra were

notably smoother than experimental spectra. The complexity of the theoretical and experimental horizontal spectra was comparable. The horizontal spectra showed more structure than the vertical spectra. In both cases, where power was concentrated in the frequency band, there were noticeable peaks in the curves which were comparable to peaks in the experimental spectra.

To eliminate adverse source-receiver spectral interference and to isolate the fine structure caused by crustal reverberation, the experimental amplitude spectra were whitened by application of the inverse P-pulse spectrum. The results indicated that the reverberatory character of the theoretical data was not present. There are three possible reasons for these results.

First, the placement of the receiver transducer might be slightly in error. Theoretical amplitude spectra were computed for a receiver 2 mm below the surface of the model. Results indicated that the change in receiver depth did not critically affect the spectral structure in the frequency band of interest.

Next, the possibility that the epoxy bond at the layer interface might alter the spectra was investigated. Results showed that a thin layer of epoxy bond can exert appreciable influence on the magnitude of the peaks, although the relative position of the peaks remains comparatively stable.

Finally, the presence of the lateral discontinuity in model H-6 made a legitimate comparison of these spectra possible only at the lowest phase velocity.

BLANK PAGE

SECTION II
DISPERSION ESTIMATES FOR LASA

A. LASA CRUSTAL STRUCTURE

The Crustal Studies Annual Report[1] presented LASA high-frequency dispersion and excitation curves developed from Steinhart and Meyer's 1959 measurements of the Montana crust.[2] From that 1959 investigation, two essentially different crustal models are derived. On of the models corresponds to the crust under the southern part of the Large Aperture Seismic Array (LASA) in Eastern Montana, shown on the map in Figure II-1. The other model corresponds to the crust under the northern part of LASA. Physical parameters for the LASA-north and LASA-south crusts are given in Table II-1.

The upper three layers of the LASA-south crust were used for the high-frequency calculations in the annual report, and the entire crustal model also was included in that report for completeness. Low-frequency normal and leaky-mode dispersion curves were determined for the LASA-south crust (Figure II-2). Figure II-3 displays the M11 shear-mode dispersion between 0.0 and 0.1 cps for the LASA-north crust.

B. LONG-PERIOD LASA EVENTS

Dispersion analysis was performed for two earthquakes recorded by long-period seismometers at LASA. Three channels of long-period data (vertical, horizontal N-S, and horizontal E-W) were recorded at each subarray location. Figure II-1 shows the locations and station codes of the 21 three-component systems, and Figure II-4 gives the long-period seismograph response of the system.

The epicenter of the first event was located off the coast of northern California and had an epicentral distance of about 1800 km. Table II-2 describes associated PDE (Preliminary Determination of Epicenters)

science services division
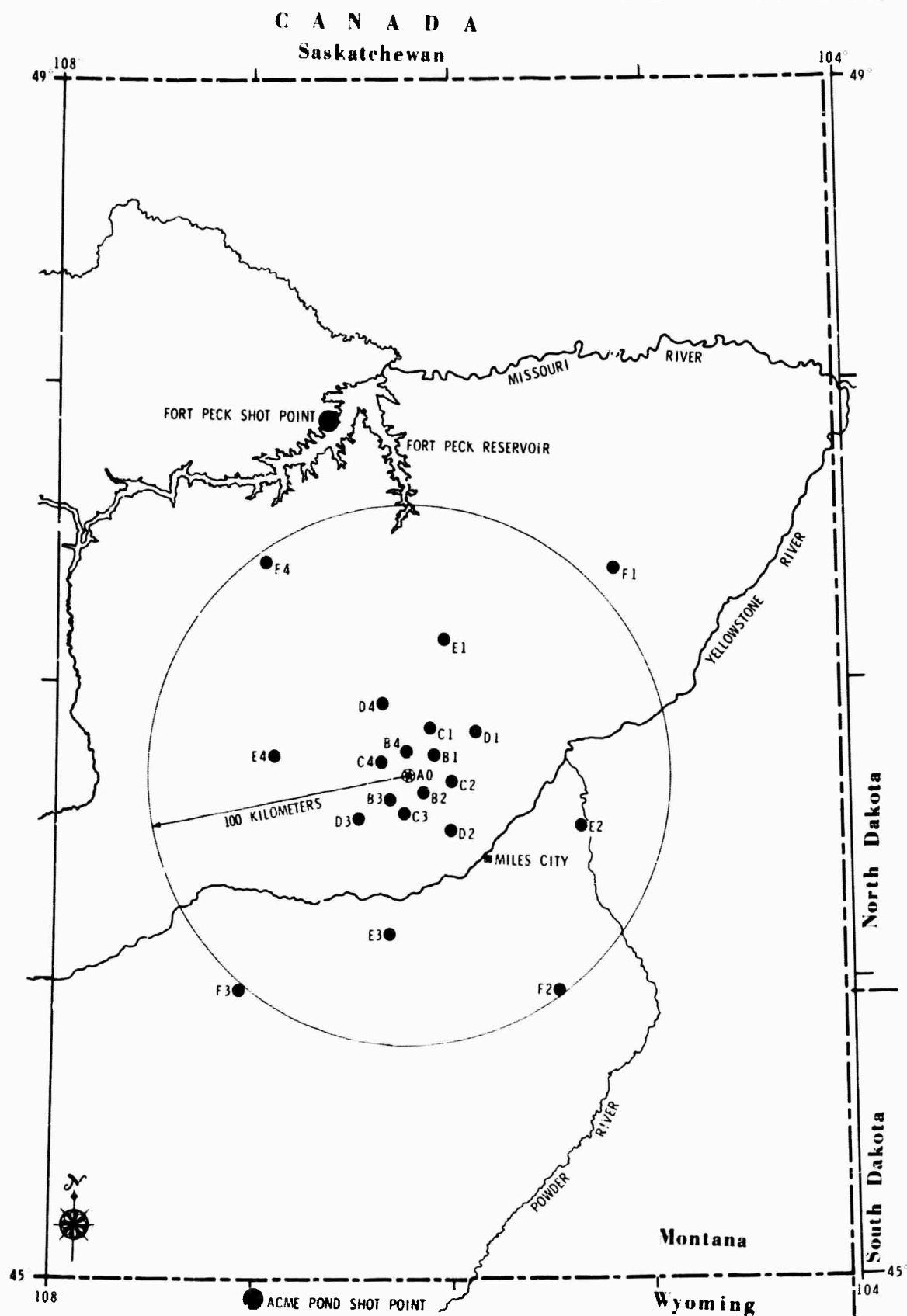
Figure II-1.   Large Aperture Seismic Array in Eastern Montana

science services division

Table II-1

PHYSICAL PARAMETERS FOR LASA CRUSTAL MODELS

(a) LASA-South

Layer	Compressional Velocity, α (km/sec)	Shear Velocity, β (km/sec)	Layer Thickness (km)
1	2.60	1.50	0.3
2	3.70	1.85	3.0
3	6.08	3.51	20.0
4	6.97	4.02	17.0
5	7.58	4.38	10.0
Half-space	8.07	4.66	∞

(b) LASA-North

Layer	Compressional Velocity, α (km/sec)	Shear Velocity, β (km/sec)	Layer Thickness (km)
1	2.60	1.50	0.3
2	3.70	1.85	2.0
3	6.08	3.51	15.0
4	6.97	4.02	17.0
5	7.58	4.38	23.0
Half-space	8.07	4.66	∞
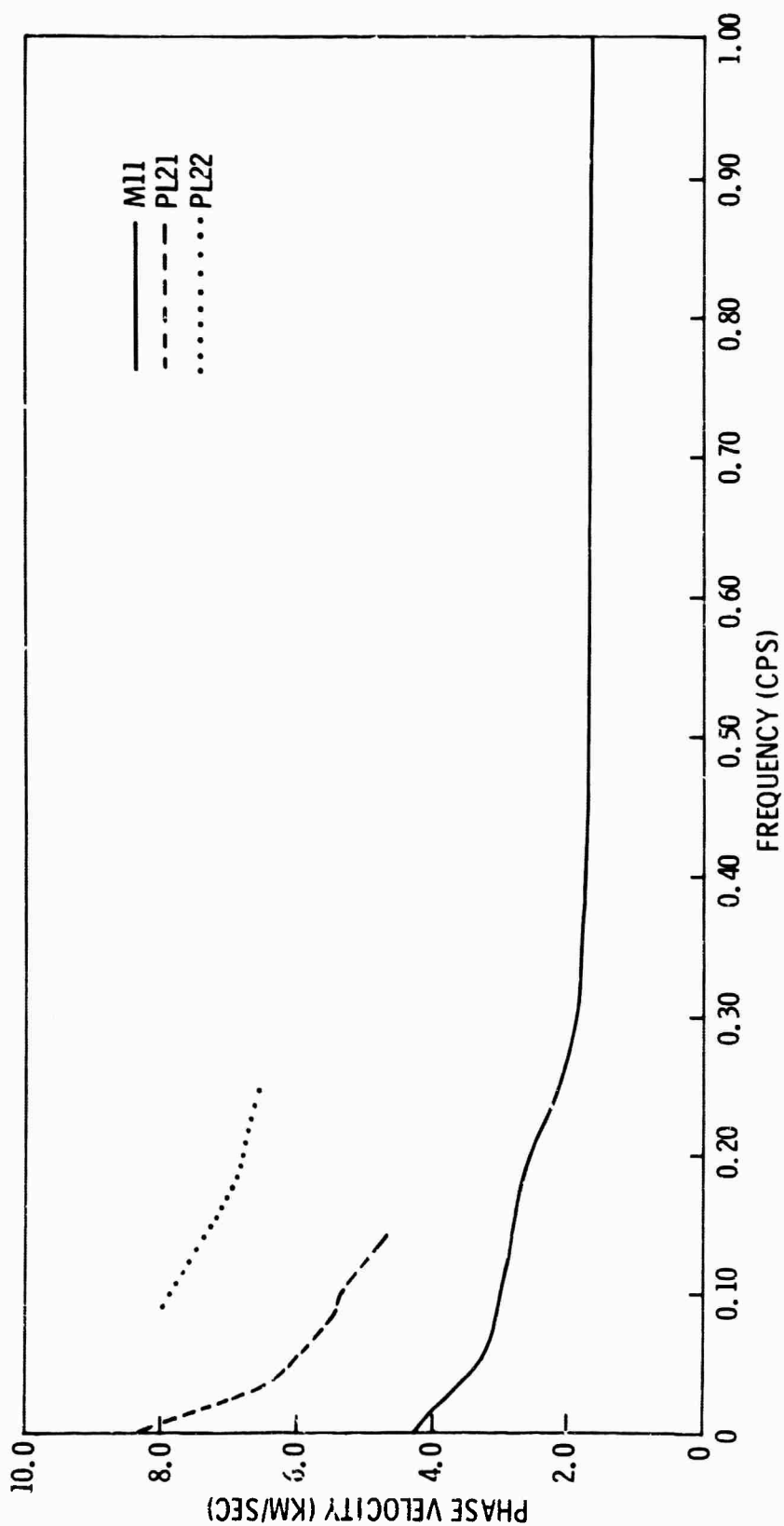
Figure II-2. LASA Low-Frequency Shear- and Leaky-Mode Dispersion Curves
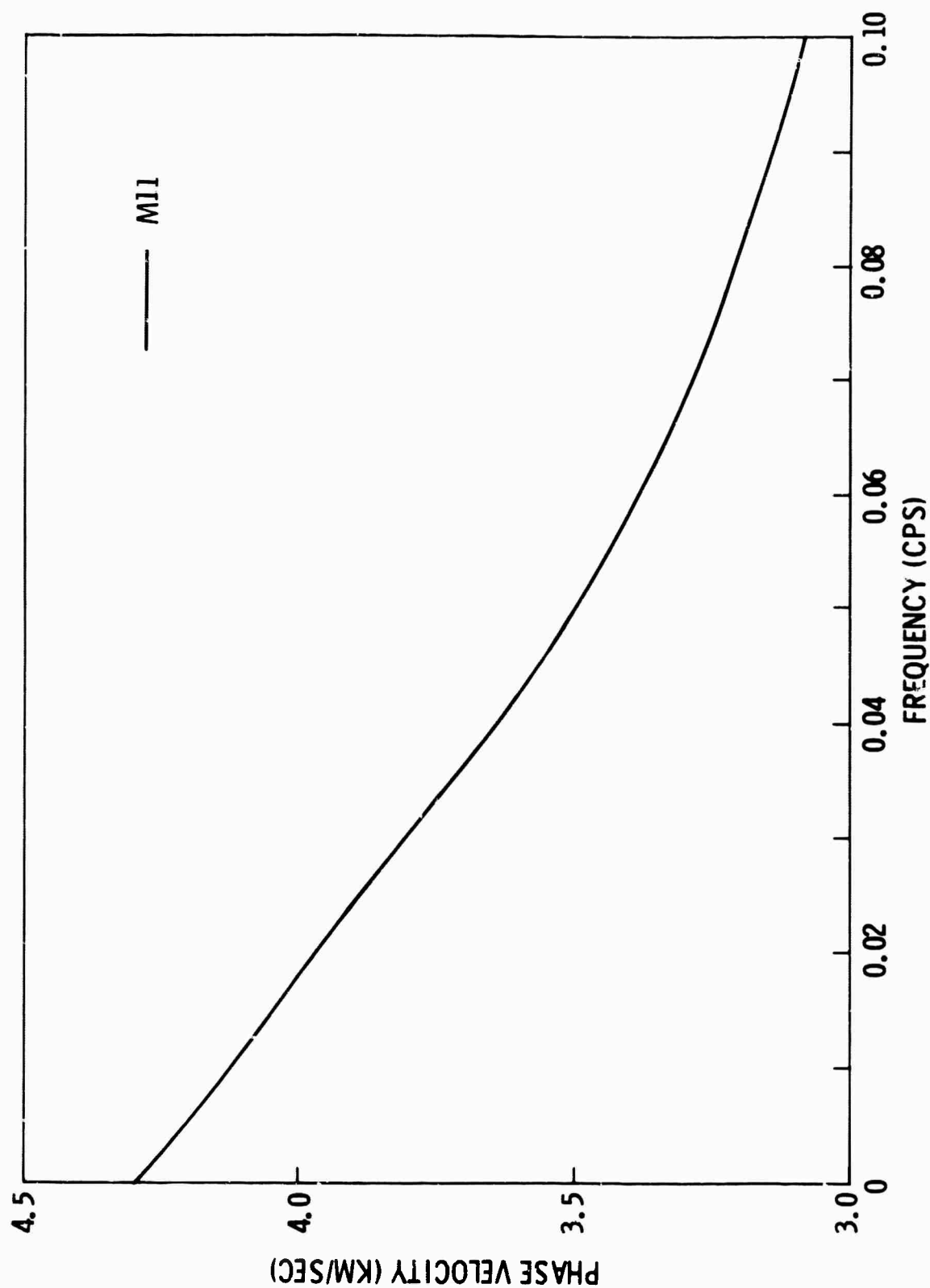
Figure II-3. M11 Shear-Mode Dispersion Curve for LASA-North Crustal Model

science services division
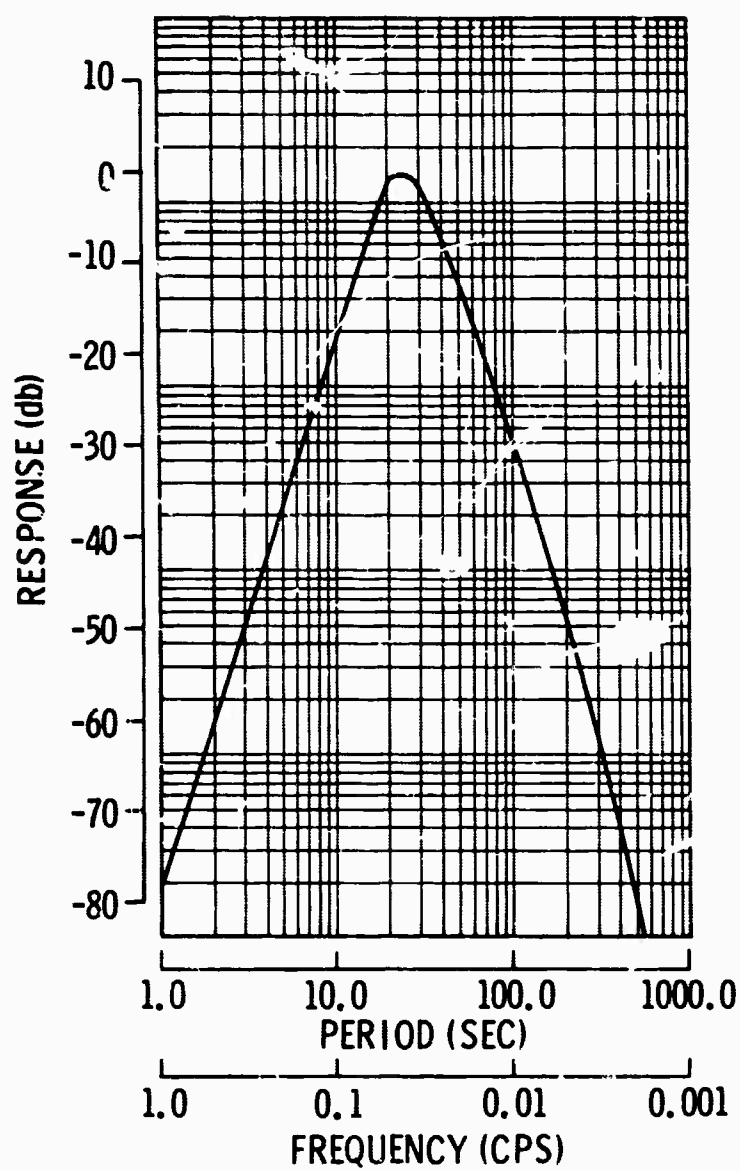
Figure II-4. Long-Period Seismograph Response Measured in Terms of Particle Displacement

science services division

Table II-2

ASSOCIATED PDE INFORMATION

FOR

CALIFORNIA EVENT

Location	Off Coast of Northern California
Date	11 November 1966
Origin time	18:21:05*
Latitude	40.3 N
Longitude	127.1 W
Magnitude	4.5 (CGS), 4.9 (BRK)
Depth	33 P

*Indicates an estimated accuracy of 0.5° in latitude and longitude and 50 km in depth

science services division

information for this earthquake. Vertical, horizontal N-S, and horizontal E-W seismograms of the event are shown in variable-area display in Figures II-5, II-6 and II-7, respectively. Table II-3 gives the channel identification, distance, and azimuth of each recording station. P and S arrivals are seen on the vertical and horizontal E-W recordings, followed by a large amplitude Rayleigh wave. The horizontal N-S component with orientation most nearly transverse to the direction of propagation shows significant Love-wave motion. Higher order modes are not visually apparent on these recordings.

Power spectra for four stations were computed for this event and are shown in Figure II-8. These spectra show that the bulk of the energy lies in the 0.02- to 0.08-cps frequency range. Superimposed on each of these curves is the response for the long-period seismometers used to record the events. Note the good agreement of these two curves in the frequency range where most power lies.

The second event's epicenter was located in the Greenland Sea, and the epicentral distance was about 5700 km. Table II-4 describes the associated PDE information. Vertical, horizontal N-S, and horizontal E-W seismograms of the event are shown in Figures II-9, II-10 and II-11, respectively. Table II-3 gives the distance and azimuth of each recording station for this event. An examination of these recordings shows multiple P and S arrivals, followed by a well-defined large-amplitude Rayleigh wave.

Power spectra for four stations of this event are shown in Figure II-12. The energy is similar to that of the California event.

C. TWO-STATION DISPERSION ESTIMATES

The vertical component of the California event was used for dispersion measurements. The Rayleigh-wave portion of the seismogram was time-partitioned, and transfer functions were computed between pairs of stations (seismometers).
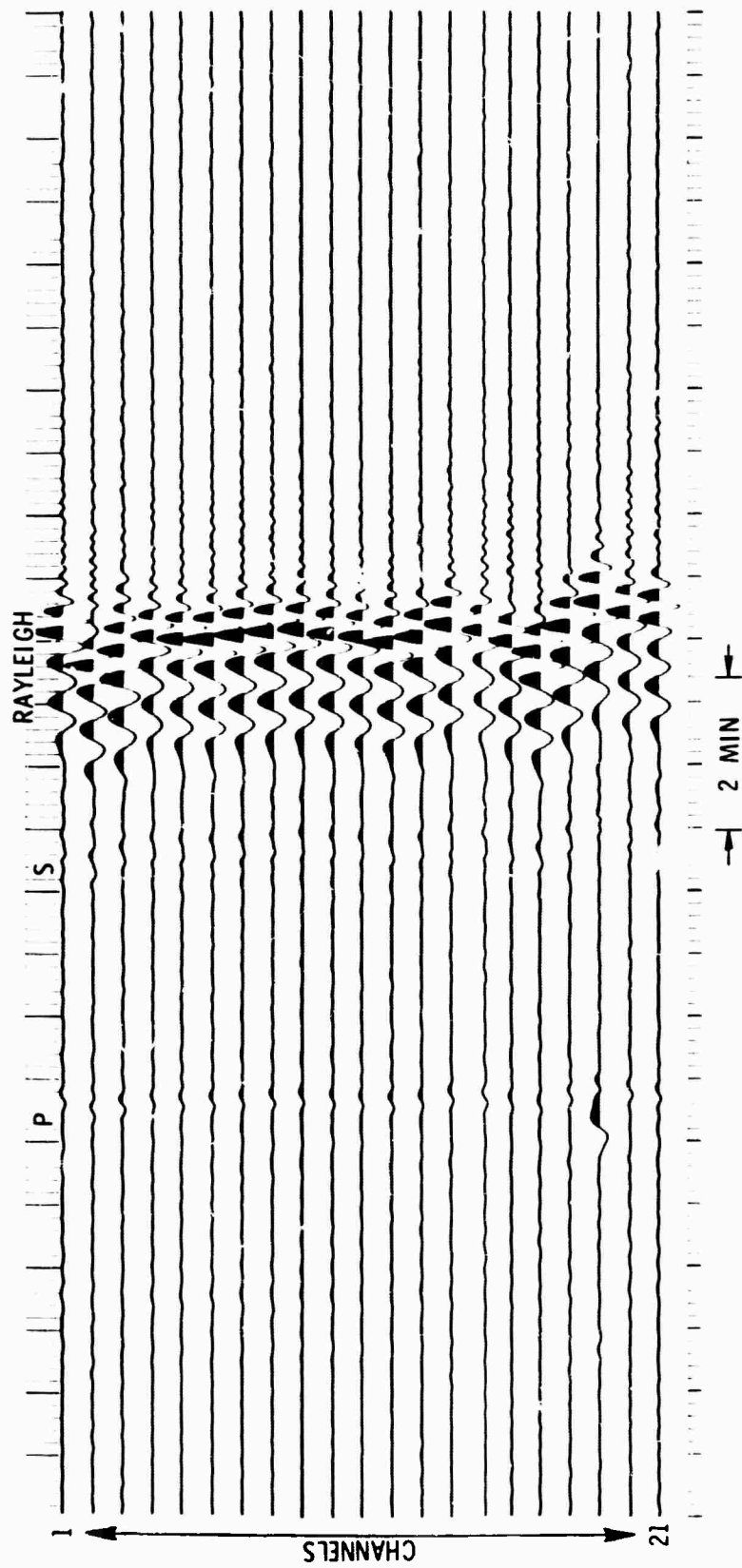
Figure II-5. Vertical Seismogram Recordings of the California Event
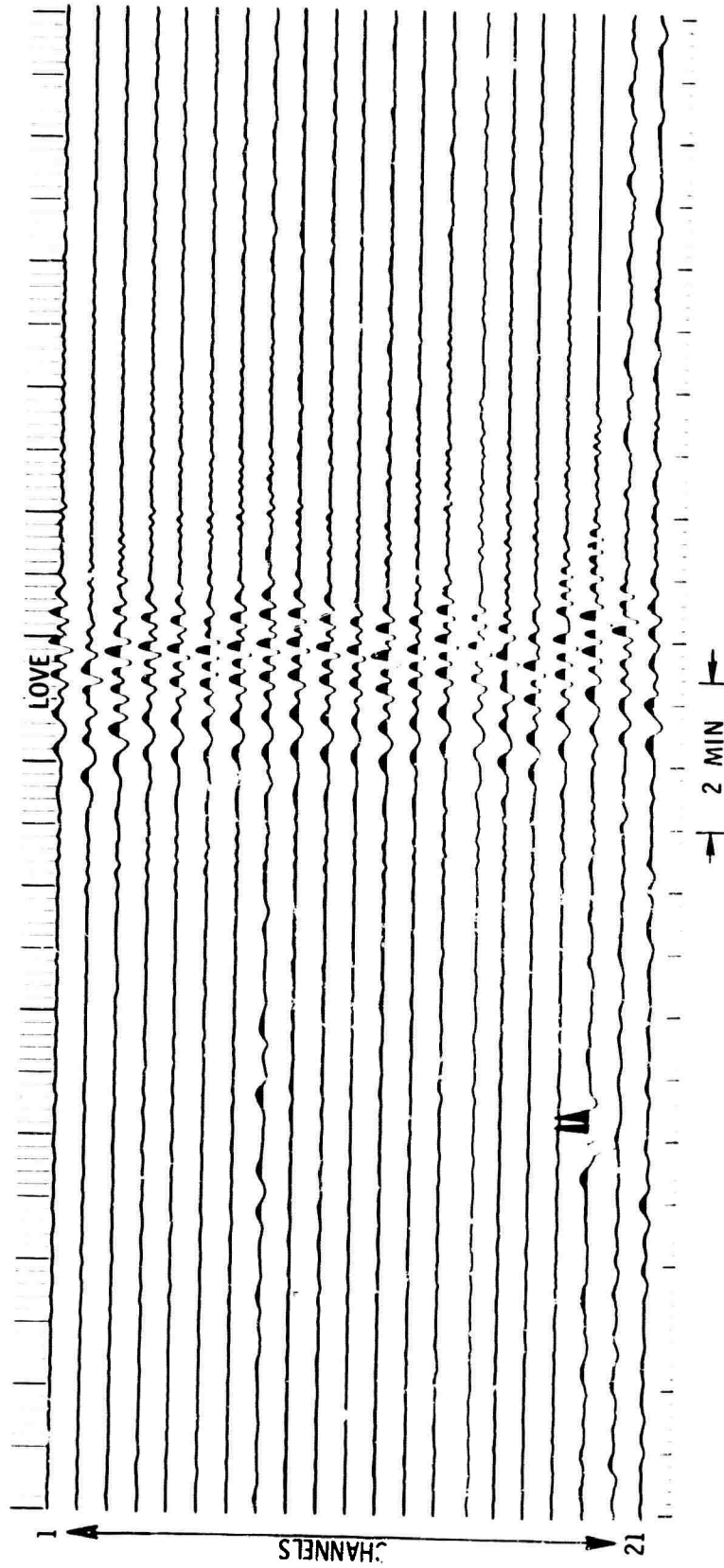
Figure II-6. Horizontal N-S Seismogram Recordings of the California Event

science services division
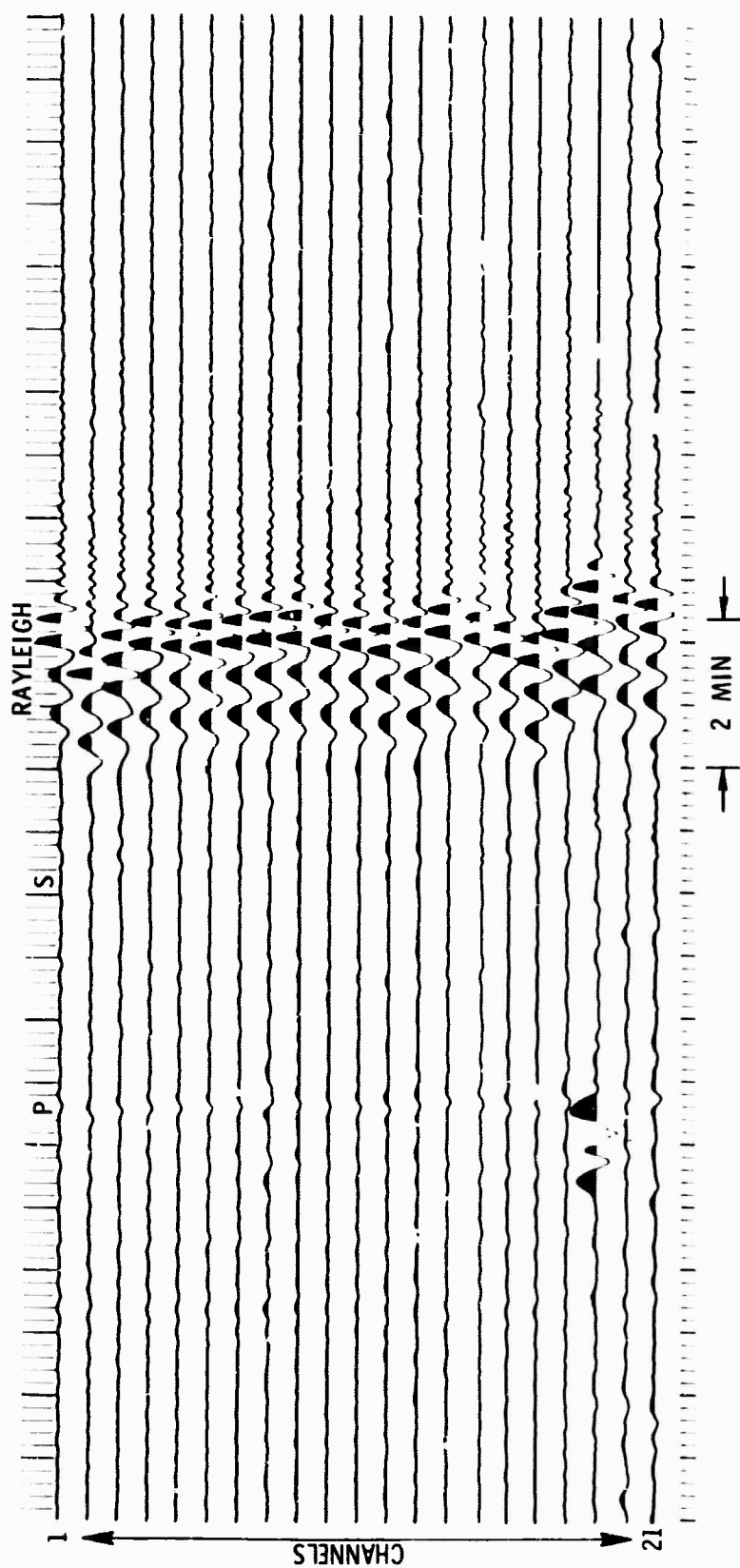
Figure II-7.   Horizontal E-W Seismogram Recordings of the California Event

Table II-3

CHANNEL IDENTIFICATION, DISTANCE, AND AZIMUTH
FOR CALIFORNIA AND GREENLAND EVENTS

Channel No.	Station Code	California Event		Greenland Event	
		Distance (km)	Azimuth to Epicenter (°)	Distance (km)	Azimuth to Epicenter (°)
1	B1	1835.71	254.62	5754.40	19.70
2	F3	1739.99	255.92	5861.48	19.28
3	F4	1795.33	251.27	5707.24	19.69
4	A0	1824.21	254.65	5764.42	19.65
5	B3	1816.36	254.62	5769.93	19.62
6	C4	1814.43	254.29	5763.43	19.63
7	B4	1825.03	254.36	5756.64	19.67
8	C1	1835.67	254.29	5746.19	19.71
9	C2	1839.14	254.99	5761.02	19.69
10	B2	1827.04	254.91	5768.50	19.65
11	C3	1818.85	254.99	5777.11	19.61
12	D3	1801.08	254.76	5785.59	19.56
13	D4	1820.09	253.60	5742.04	19.68
14	D1	1853.17	254.61	5740.03	19.76
15	D2	1834.56	255.54	5778.39	19.65
16	E3	1800.84	256.29	5823.76	19.49
17	E4	1775.37	253.46	5774.65	19.52
18	E1	1850.90	253.34	5710.53	19.81
19	F1	1920.49	253.87	5666.38	20.06
20	E2	1882.92	256.34	5760.65	19.79
21	F2	1859.01	258.13	5826.92	19.60

Figure II-8. Power Spectra of the California Event Recorded at Stations
F3, E4, F1, and E2

Table II-4

ASSOCIATED PDE INFORMATION

FOR

GREENLAND EVENT

Location	Greenland Sea
Date	18 November 1966
Origin time	18:48:43.9
Latitude	73.4 N
Longitude	6.8 E
Magnitude	4.9 (CGS)
Depth	33 R

science services division
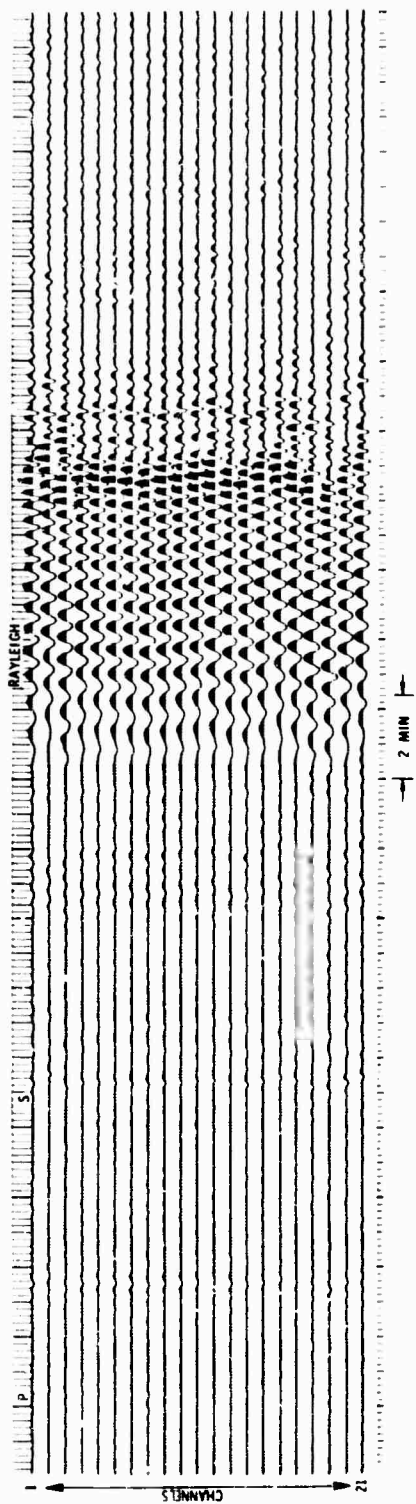
Figure II-9. Vertical Seismogram Recordings of the Greenland Event
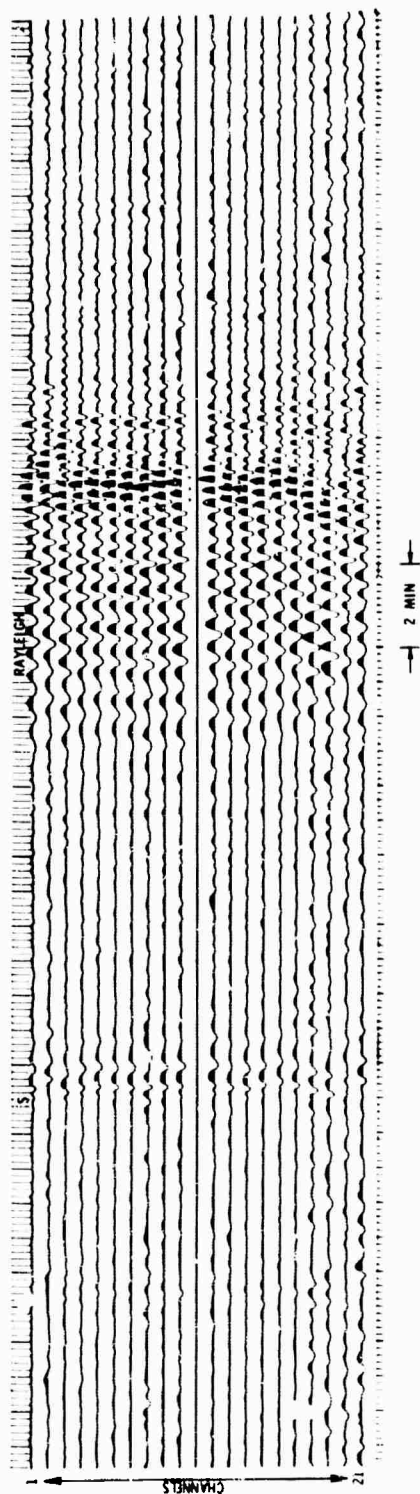
Figure II-10 Horizontal N-S Seismogram Recordings of the Greenland Event

science services division
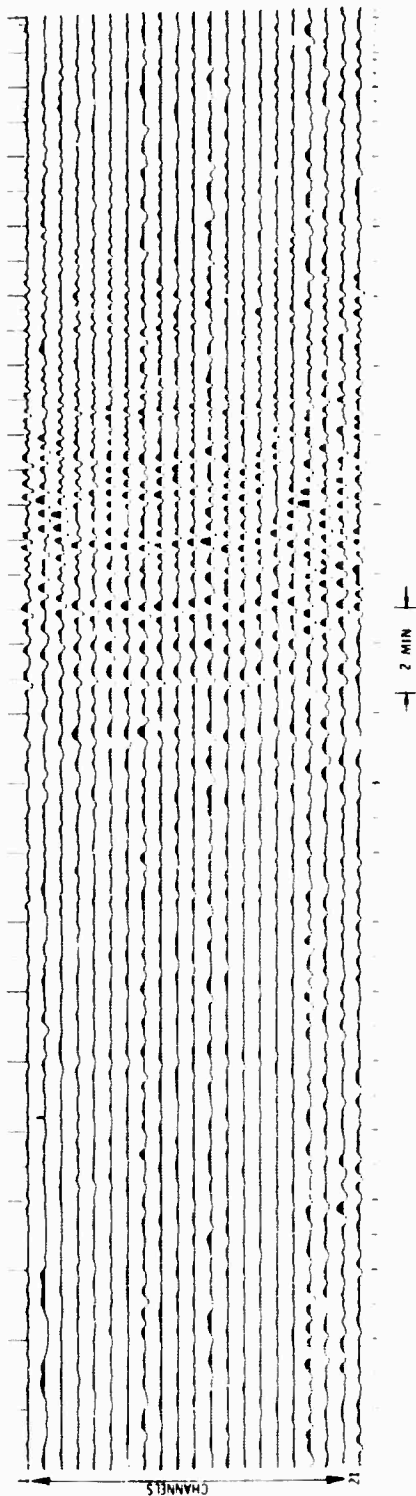
Figure II-11. Horizontal E-W Seismogram Recordings of the Greenland Event

science services division
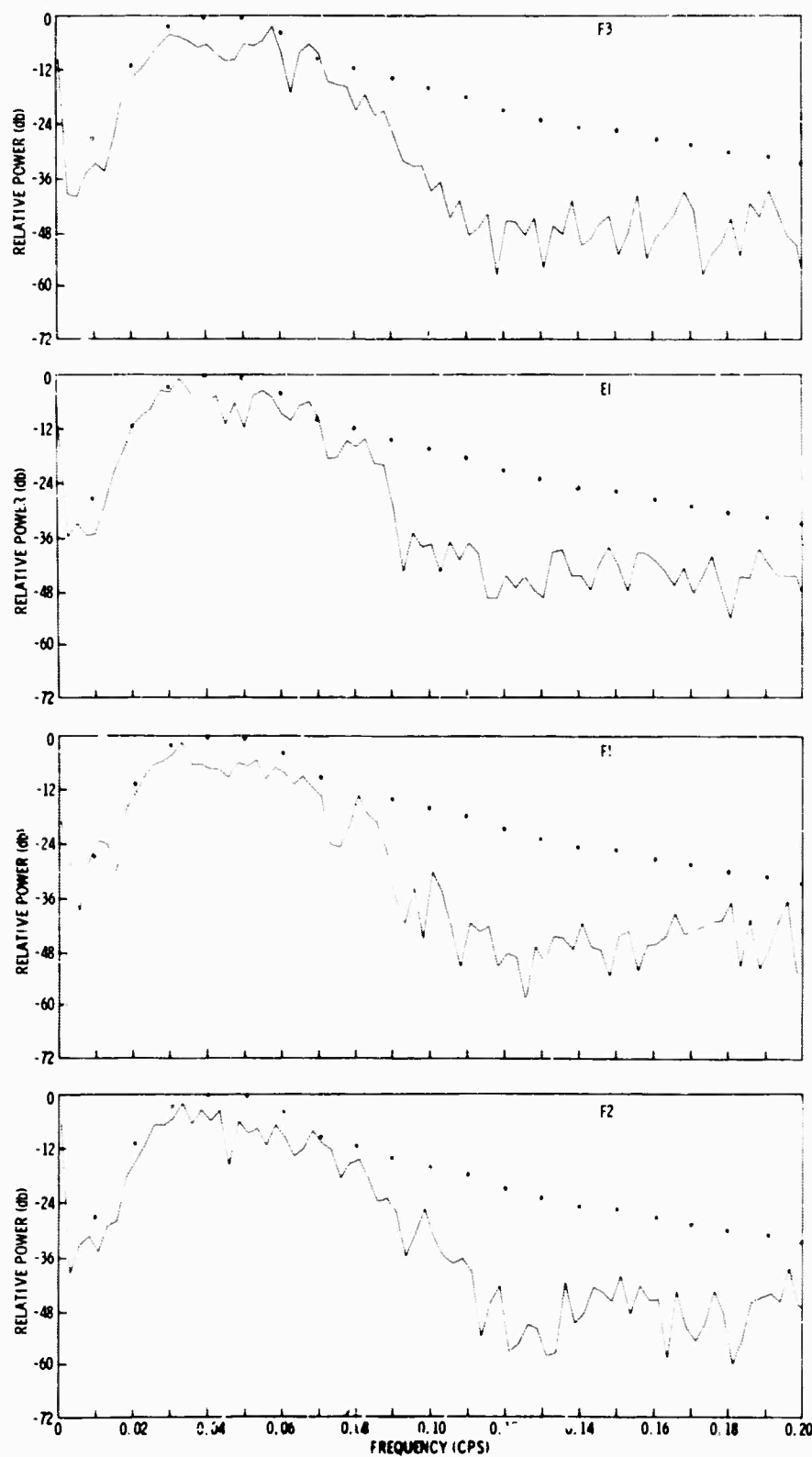
... SEISMOMETER
RESPONSE

Figure II-12. Power-Spectra of the Greenland Event Recorded at Stations F3, F1, F1, and F2

The phase velocity C(f) was then determined using

$$C(f) = \frac{2\pi f \Delta \chi}{2N\pi - \theta(f)}$$

where

$\theta(f)$ is the phase of the transfer function

N is an integer

$\Delta \chi$ is the difference in the computed great-circle distances from the epicenter to the individual stations

As seen in Figure II-13, the dispersion results obtained from four pairs of stations show a large variation. Since the agreement between the estimates was poor, additional dispersion estimates were obtained using other pairs of stations. The variations were, in some cases, even larger than before, and no apparent systematic change was determined which would indicate lateral crustal changes across the array.

The $\Delta \chi$ factor computed in the above manner is valid if the epicenter of the event is correctly known and if the waves propagate along a great-circle path. It is well known that lateral refraction may occur, causing the waves to arrive at an azimuth which deviates by several degrees from the computed great-circle path.. However, this effect may be small when using the large wavelengths measured here. The USC&GS epicenter determination (Table II-2) indicates an estimated accuracy of $0.5°$ in latitude and longitude for this event. This uncertainty in the computed great-circle path due to lateral refraction and epicenter-location error may be removed by a triangulation technique using three stations, as explained in the following section.
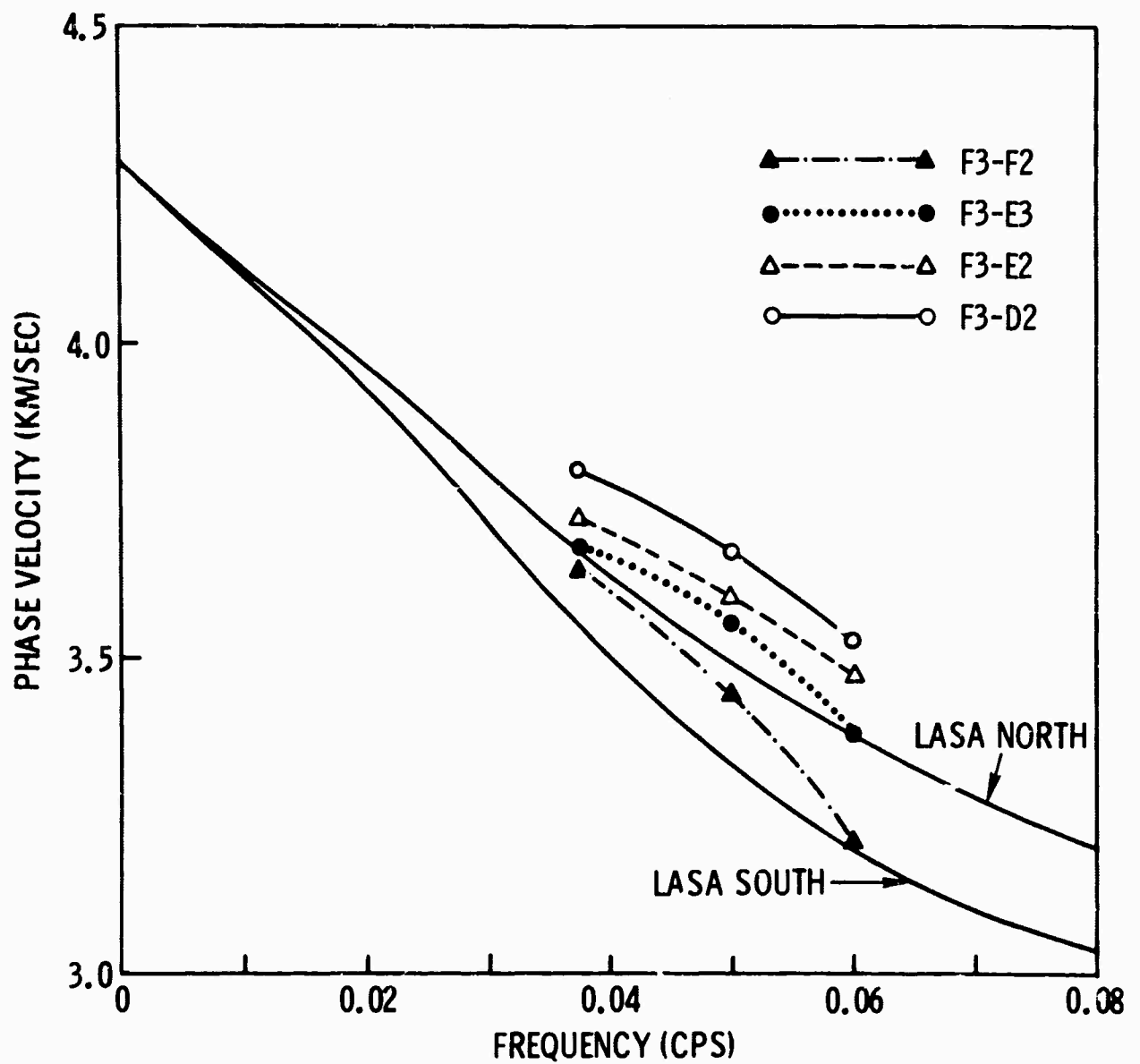
Figure II-13. Rayleigh-Wave Dispersion Estimates Measured frcm the
California Event Using the Two-Station Method

science services division

D. DISPERSION ESTIMATES USING THREE SEISMOMETERS

1. Theory

When the propagation direction of a wavefront is known exactly, phase velocity estimates for plane waves are computed accurately by Fourier tranform methods.[3] However, errors in the direction of wave propagation lead to incorrect results (Figure II-14). The apparent distance traveled is a function of the angle between the true direction and apparent wavefront. The apparent velocity is therefore higher than the actual velocity; hence, the time required for passage of a phase between two seismometers appears less than the actual time required.

To remove uncertainty in the true wavefront direction and to improve dispersion estimates, three seismometers were used. The idea follows that given by Knopoff[4] and is briefly explained as follows.

Consider three seismometers located as shown in Figure II-15. Let $\vec{V}$ be the true phase velocity vector which is unknown. In order to determine $\vec{V}$, it is necessary to determine the scalar magnitude V of $\vec{V}$ and either φ_1 or φ_2, the angle between the phase-velocity vector and V_1 or V_2, respectively.

For a given phase which passes S_1 and S_0, let V_1 be the time required for the phase to pass the distance from S_1 to S_0. Define V_2 similarly.

It then follows that

$$V = V_1 \cos \varphi_1 \tag{2-1}$$

$$V = V_2 \cos \varphi \tag{2-2}$$
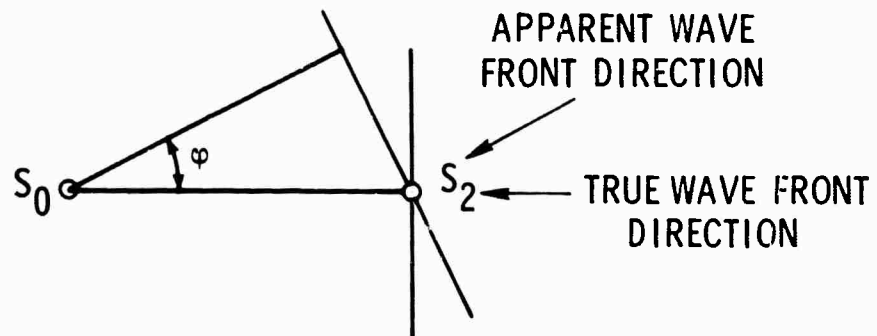
Figure II-14. Effects of Using Erroneous Direction of Propagation
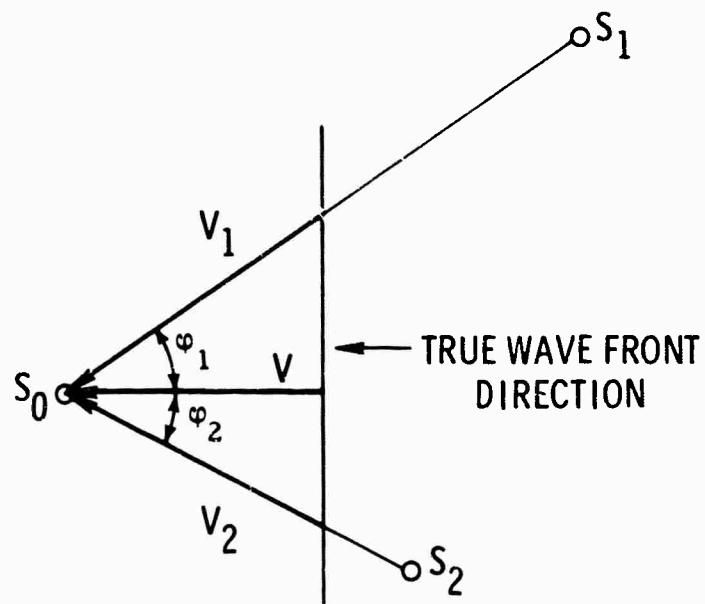
Figure II-15. Use of Three Seismometers to Measure Phase Velocity

science services division

Since V is common to both equations, the equations may be used to solve for V. First, let $\chi = \varphi_1 + \varphi_2$, and from Equations 2-1 and 2-2

$$\frac{V}{V_2} = \cos \varphi_2$$

$$= \cos \chi \cos \varphi_1 + \sin \chi \sin \varphi_1$$

$$= \frac{V}{V_1} \cos \chi + \sqrt{1 - \left(V/V_1\right)^2} \sin \chi$$

Some algebraic manipulation gives

$$\frac{1}{V_1^2} + \frac{1}{V_2^2} = \frac{2 \cos \chi}{V_1 V_2} + \frac{\sin^2 \chi}{V^2} \tag{2-3}$$

Solving this equation for V and simplifying gives

$$V = \left[\frac{V_1^2 V_2^2 \sin^2 \chi}{V_1^2 + V_2^2 - 2V_1 V_2 \cos \chi}\right]^{1/2} \tag{2-4}$$

V_1 and V_2 are measured quantities, and χ is determined from the array geometry.

After V is calculated by use of Equation 2-4, φ_1 and φ_2 are readily determined from Equations 2-1 and 2-2. Hence, the true phase-velocity vector $\vec{V}$ is determined, knowing neither its magnitude nor its direction.

The effect of small first-order errors in measurements of V_1 and V_2 is determined by use of Equation 2-3. From Equation 2-3, after differentiating and rearranging terms,

$$\sin^2 \chi \frac{dV}{V^3} = \left(\frac{1}{V_1} - \frac{\cos \chi}{V_2}\right) \frac{dV_1}{V_1^2} + \left(\frac{1}{V_2} - \frac{\cos \chi}{V_1}\right) \frac{dV_2}{V_2^2} \qquad (2-5)$$

Thus, errors dV_1 and dV_2 made in the measurements of V_1 and V_2 cause a change dV in the true phase velocity V. Multiplication of both sides of Equation 2-5 by $V^2 / \sin \chi$ and algebraic manipulation gives

$$\sin \chi \frac{dV}{V} = \cos \varphi_1 \sin (\chi - \varphi_1) \frac{dV_1}{V_1} + \sin \varphi_1 \cos (\chi - \varphi_1) \frac{dV_2}{V_2} \qquad (2-6)$$

Thus Equation 2-6 shows that dV/V is actually dependent on dV_1 and dV_2 by a weighted average of the small changes in the measured velocities V_1 and V_2.

The smaller φ_1, the less the influence of V_2 on the computation of V. Similar manipulations show that the smaller φ_2, the less the influence of V_1 on the computation of V.

Best results can be obtained by choosing one of the seismometer legs to lie close to the great-circle path of the surface wave in question, thus making the contribution from the other leg small. This is desirable since the computed phase velocity may be associated with the leg in question rather than the entire array.

The chief advantage of using three seismometers to make dispersion estimates is that the propagation direction of the surface wave-front need not be known exactly, which is often the case for earthquakes. This method may be extended to incorporate more than three seismometers to compute phase velocities.

science services division

2. Applications and Results

A flow chart of the dispersion analysis process performed on the LASA data is presented in Figure II-16.

The transfer function[5] between pairs of stations was estimated and apparent phase velocity determined from the phase of the transfer function. Power spectra and coherence were used to determine qualitatively the significant range of the phase data. Three stations were then used to determine the phase velocity and propagation vector from the apparent velocities (described in the previous subsection). The three-station dispersion-analysis results for the California event, along with the stations used, are presented in Figures II-17 and II-18. (The station listed first is at the vertex.) Also shown are the theoretical dispersion curves for the LASA-south and LASA-north crusts, which were discussed previously. Station locations are shown in Figure II-19.

For the California event, the propagation vectors computed using the triangulation method show a station-to-station spread of approximately $6°$, which is in agreement with the expected variation due to the curvature of the wavefront reaching LASA from Northern California. The difference between the propagation vector and assumed great-circle azimuth is approximately $5°$, explaining the large amount of scatter observed in the two-station estimates and emphasizing the importance of using three stations for phase-velocity determination when the epicenter location is uncertain or lateral refraction is suspected.

Stations located generally in the northern or southern portion of LASA were chosen for use in the triangulation method. Results shown in Figure II-17 are for the northern portion of LASA, while the dispersion estimates computed using station F3, E2, F2; F3, D2, F2; and F3, E3, F2 (Figure II-18) are for the southern portion of LASA. Curves E4, E1, C1 and D3, C2, E2 (Figure II-18) are for northern LASA and central LASA, respectively.

science services division
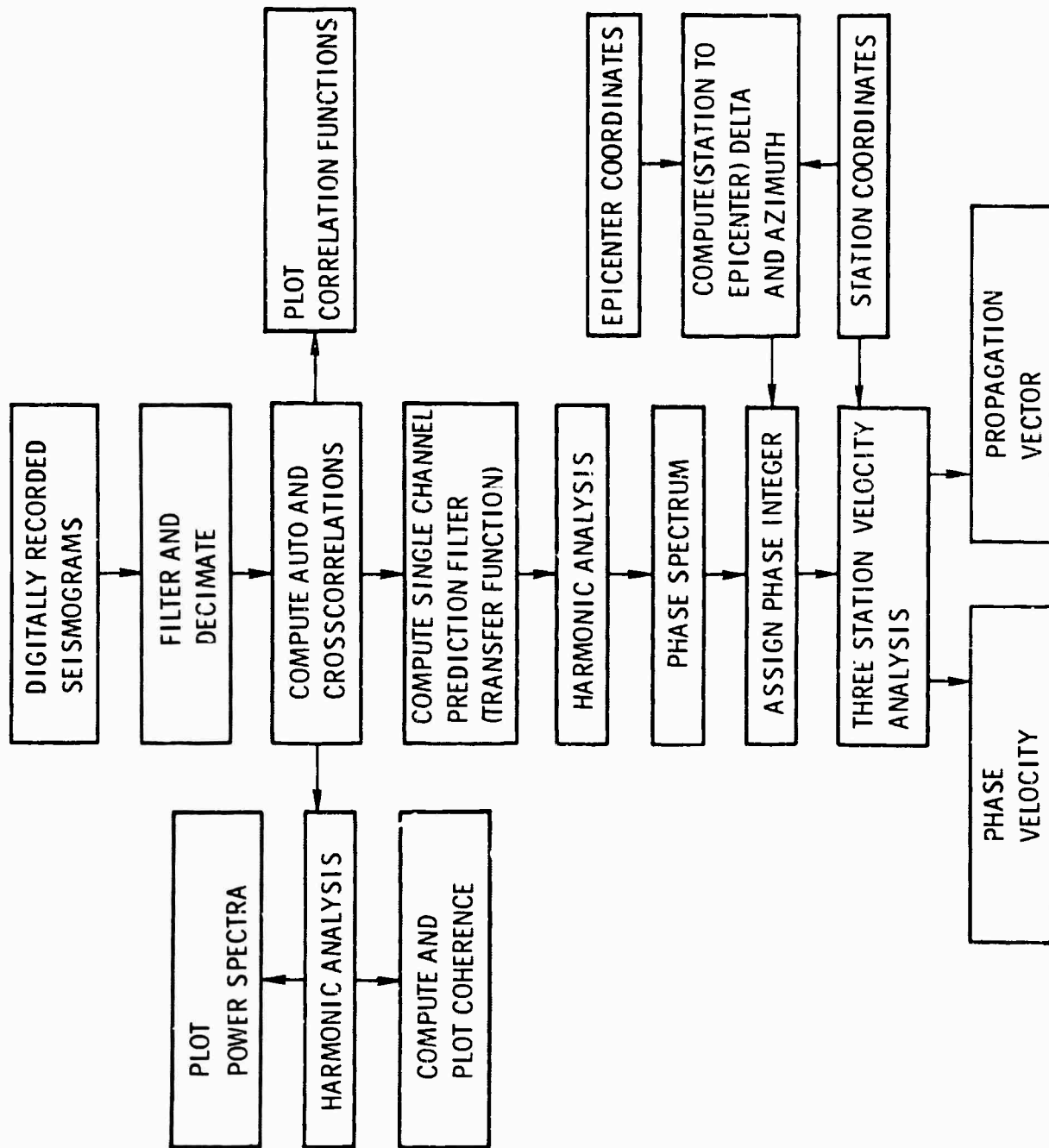
Figure II-16. Dispersion Analysis Flow-Chart

science services division

Figure II-17. Rayleigh-Wave Dispersion Estimates Measured from the
California Event Using the Three-Station Method
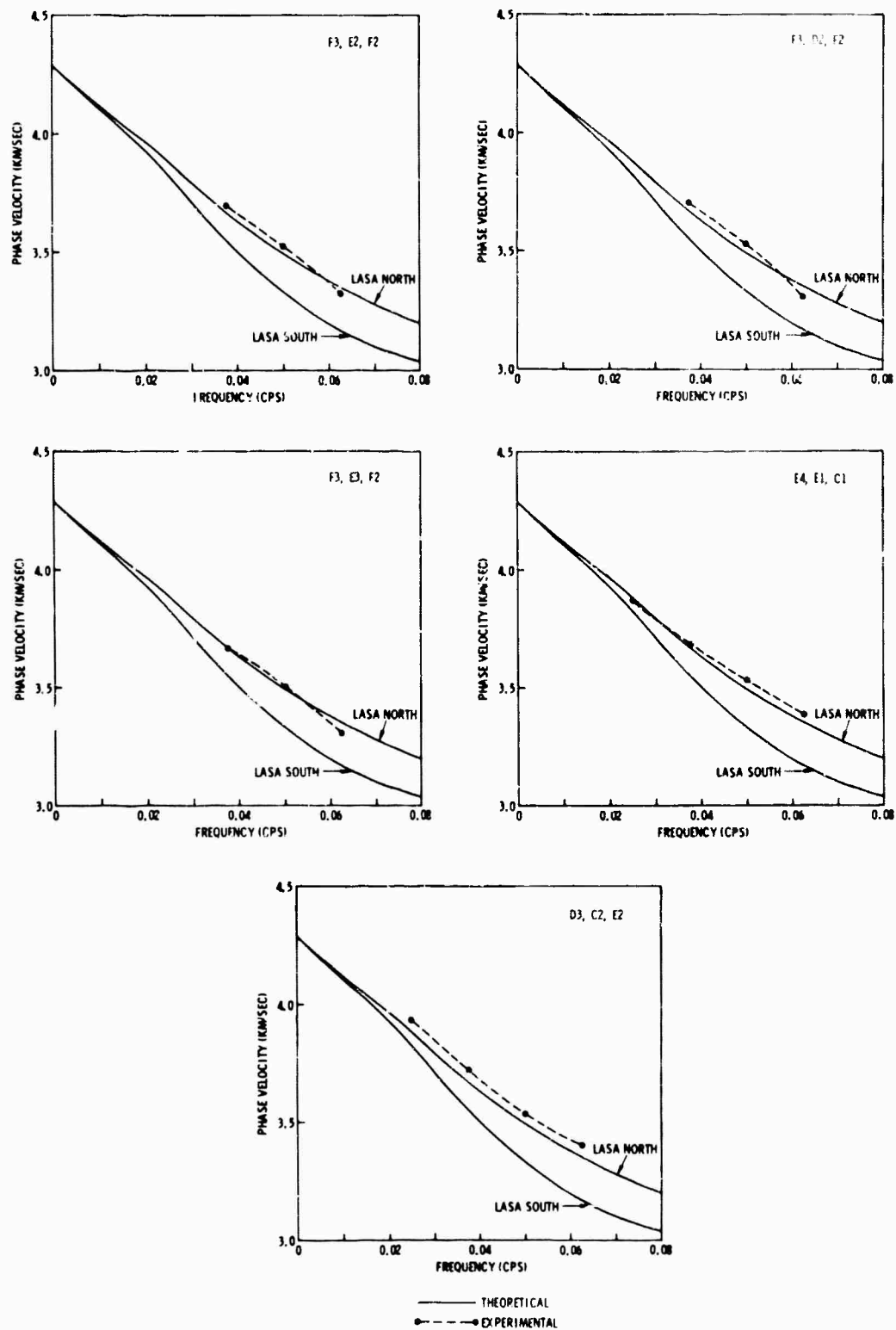
Figure II-18. Rayleigh-Wave Dispersion Estimates Measured from the
California Event Using the Three-Station Method

science services division
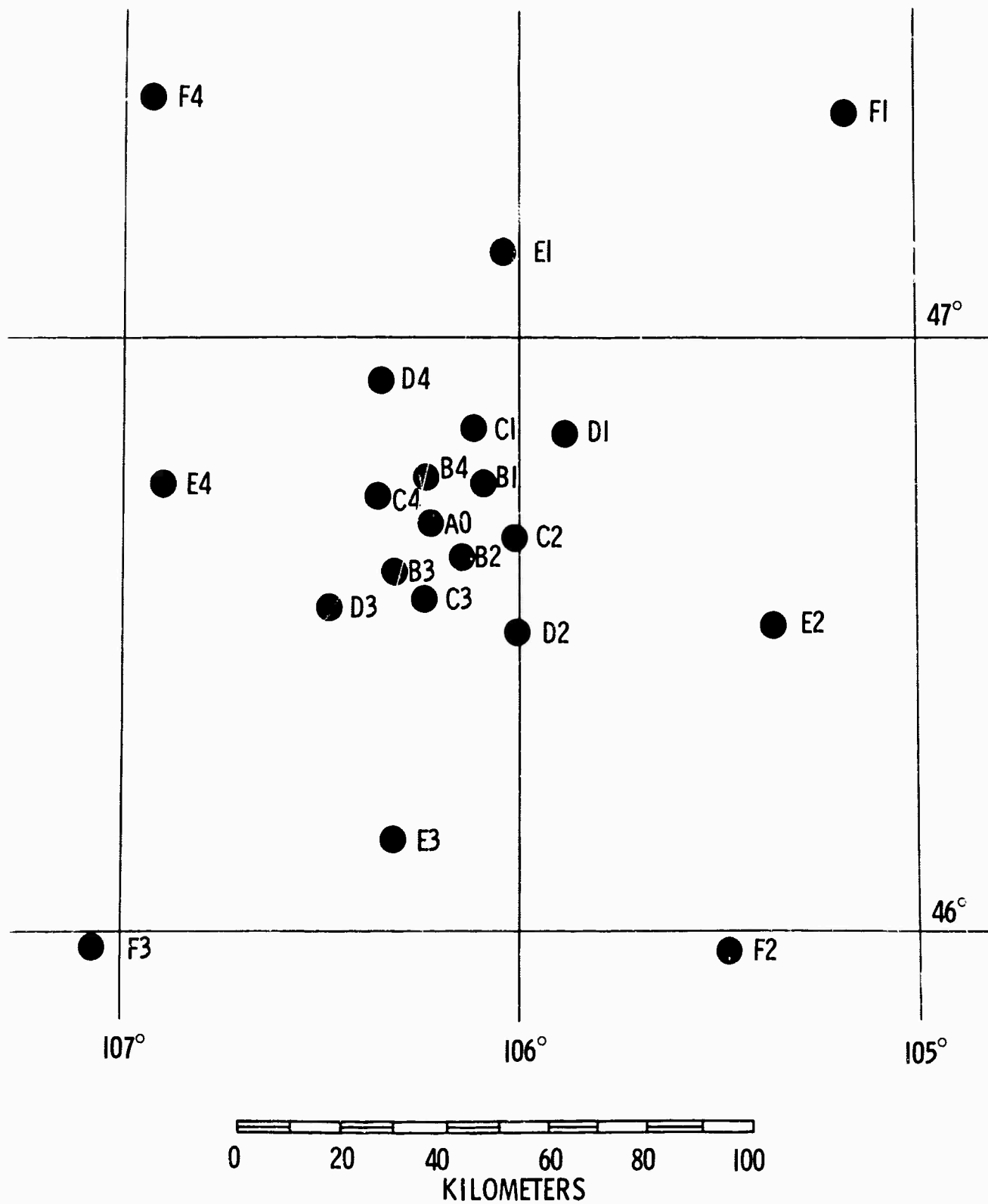
Figure II-19. Large Aperture Seismic Array Long-Period Seismometer Locations

At the highest calculated frequency, 0.0625 cps, the velocity estimates show a definite pattern. The estimates for LASA-south (Acme Pond shotpoint) are approximately 2 percent lower than those for LASA-north (Fort Peck shotpoint). The means of the computed velocities differ by 0.07 km/sec. This result agrees qualitatively with the LASA-north and LASA-south models of Steinhart and Meyer.[2]

For the Greenland event, the dispersion estimates shown in Figures II-20 and II-21 also agreed closely with those determined from the California event.

Propagation vectors computed for the Greenland event showed a wider spread than those computed from the California event. This is partially because the propagation vector in some cases lies close to one leg of the triangle formed by the three recording stations which comprise the tripartite system. The calculation of the angles associated with the propagation vectors is susceptible to errors when this is the case. These errors increase as the angle between the two legs of the tripartite system decreases, as especially observed in the results from the Greenland event. For example, a 1-percent change in V_1 caused up to a 15° change in the angle of the propagation vector.

Total variation in the phase velocity computed using both events was approximately 4 percent, which is considered excellent agreement. The variation is even less at 0.0625 cps, when LASA-north and LASA-south estimates are considered independently. Experimental curves computed for both events lie somewhat above the curve for the LASA-north theoretical model.
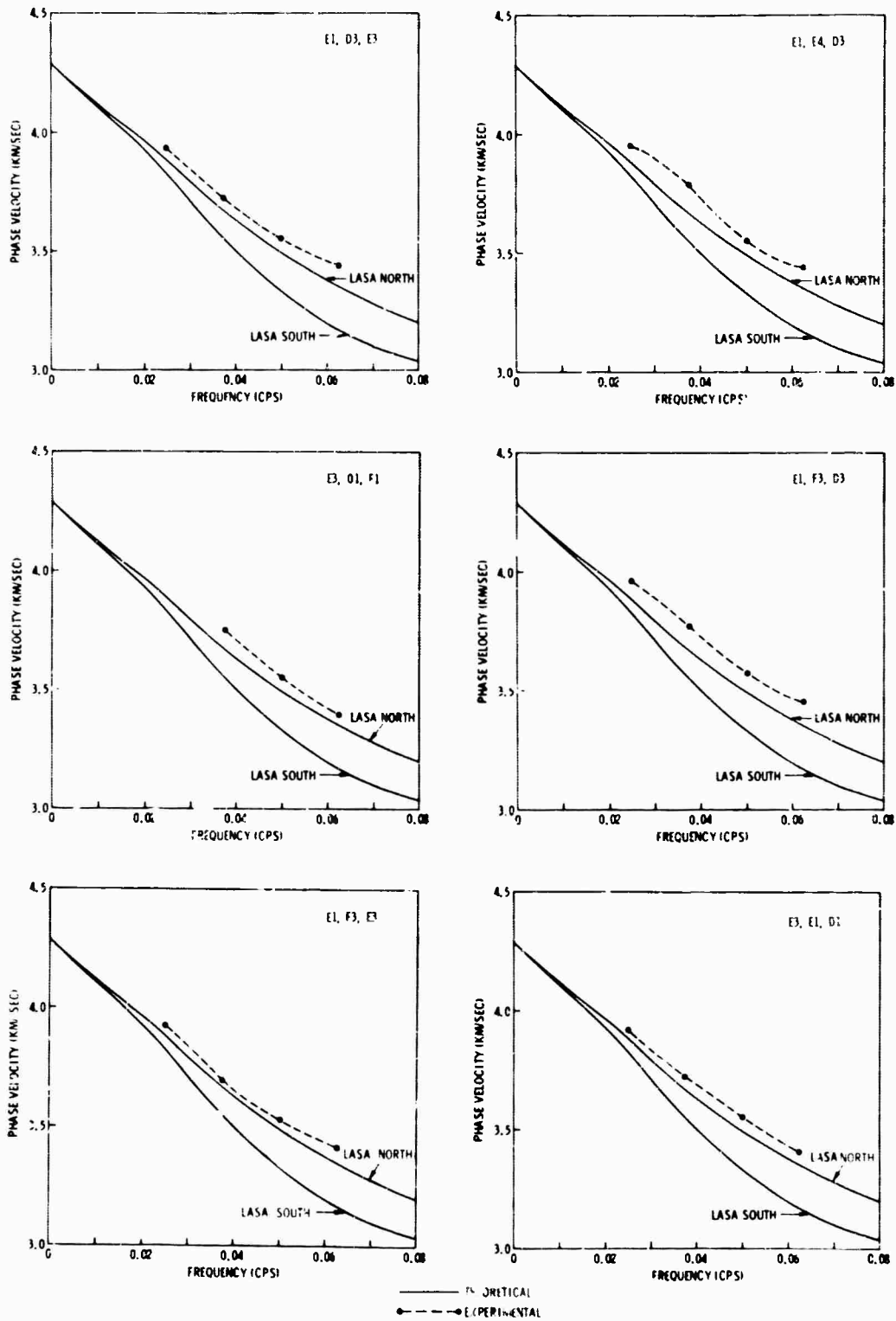
Figure II-_0. Rayleigh-Wave Dispersion Estimates Measured from the Greenland Event Using the Three-Station Method
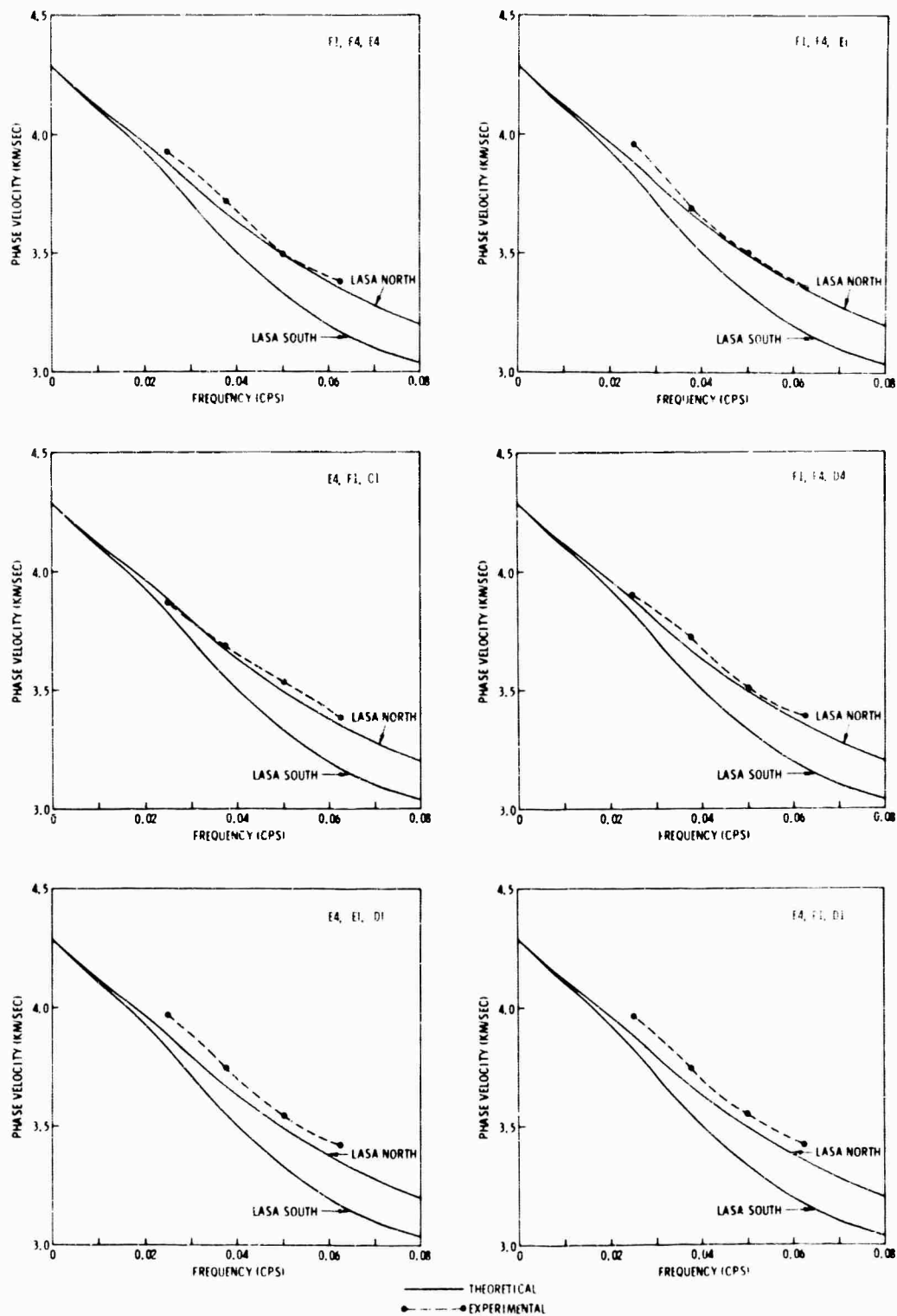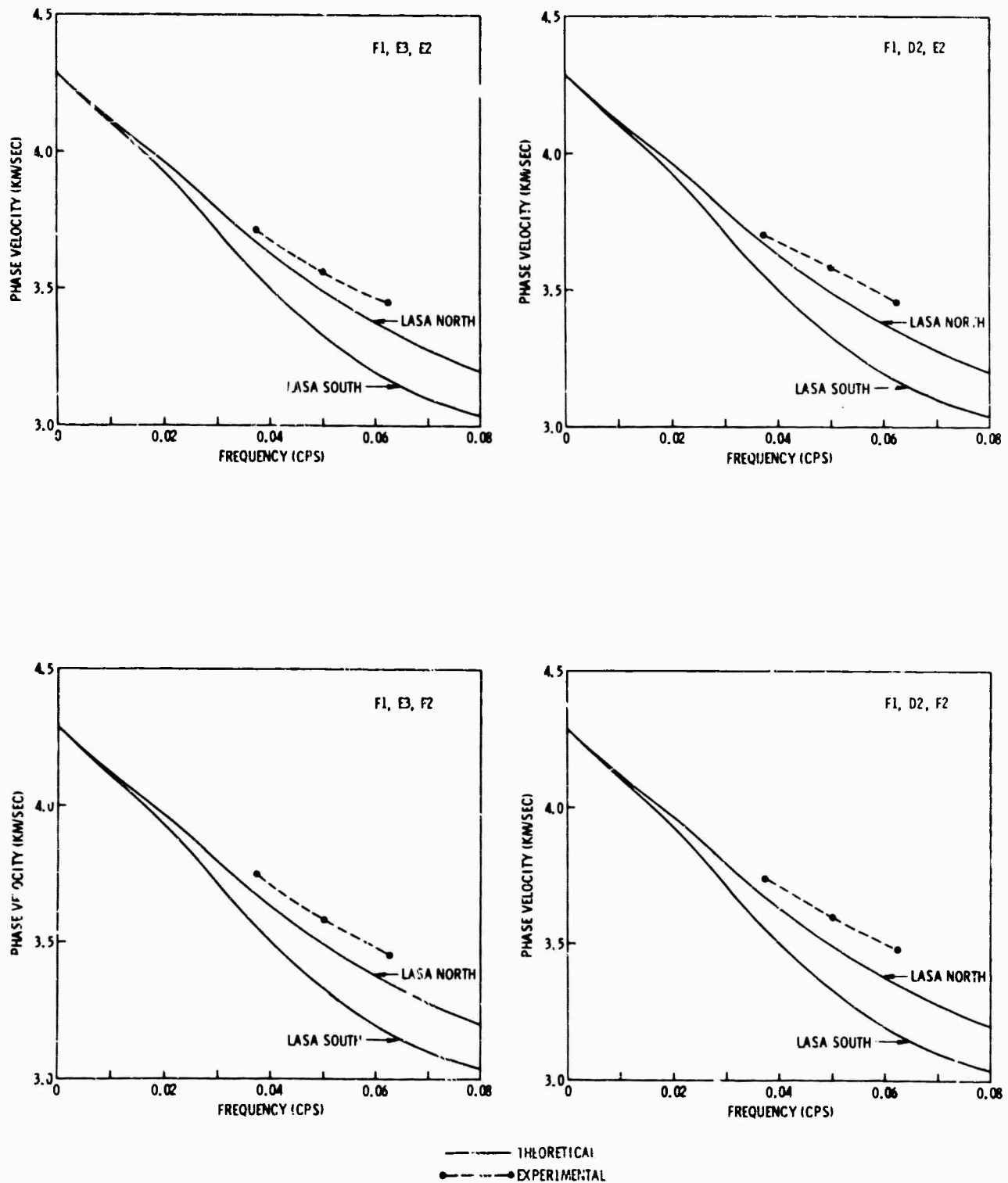
Figure II-21. Rayleigh-Wave Dispersion Estimates Measured from the
Greenland Event Using the Three-Station Method

science services division

E. LASA PERTURBED MODEL

After dispersion estimates were made using three recording seismometers, the LASA crustal model was perturbed in order to obtain better agreement between theoretical and experimental dispersion data.

Data inspection revealed that the most appropriate crustal model from available observations was some variant of the LASA-north crust. This LASA-perturbed crustal model was obtained by varying the shear velocities in layers 4, 5, and 6 for the best mean-square fit to the experimental dispersion points. The model parameters are shown in Table 11-5. As in a previous report,[1] a study of layer derivatives $(dc/d\beta_i)$ reveals that the shear velocities in layers 4, 5, and 6 are of greatest importance in obtaining agreement between theoretical and experimentially computed dispersion curves in this frequency band (Figure II-22).

The M11 dispersion curve obtained from the perturbation of the LASA-north crust is shown in Figures II-23 and II-24. Also shown in these figures are the original curves.

Maximum variations in the experimentally determined dispersion curves at four frequencies are indicated by the vertical bars on the same figures.

F. CONCLUSIONS

By using the triangulation method, much better agreement was obtained in the dispersion analysis than that obtained when only two recording seismometers were used. Uncertainty in the propagation path may cause large errors in the computed dispersion curves, but this uncertainty is satisfactorily resolved by the use of the triangulation method. Extensions to the use of four or more recording stations for dispersion estimates might prove feasible.
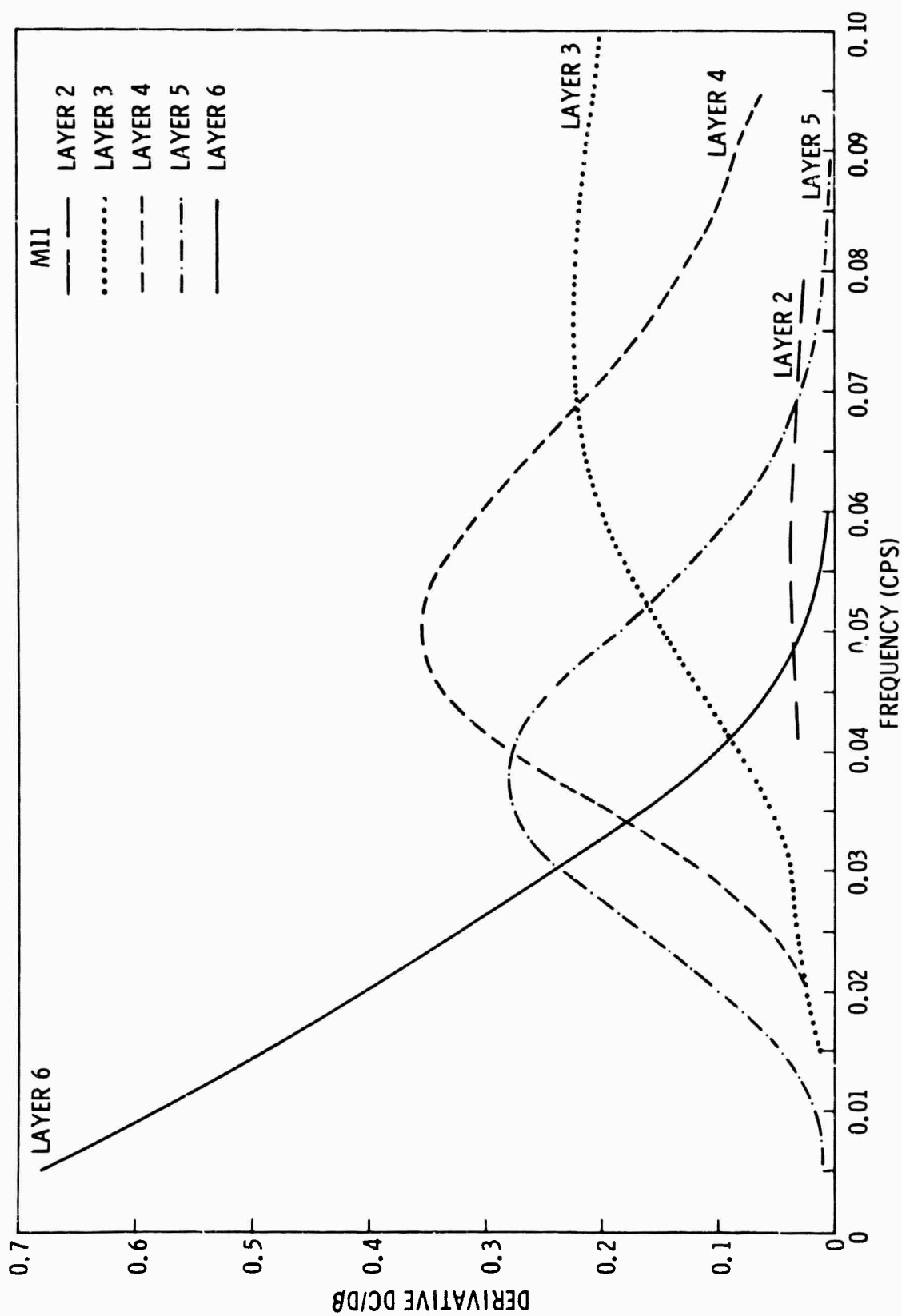
Figure II-22. Normal-Mode M11 Layer Derivatives for LASA-North Crustal Model
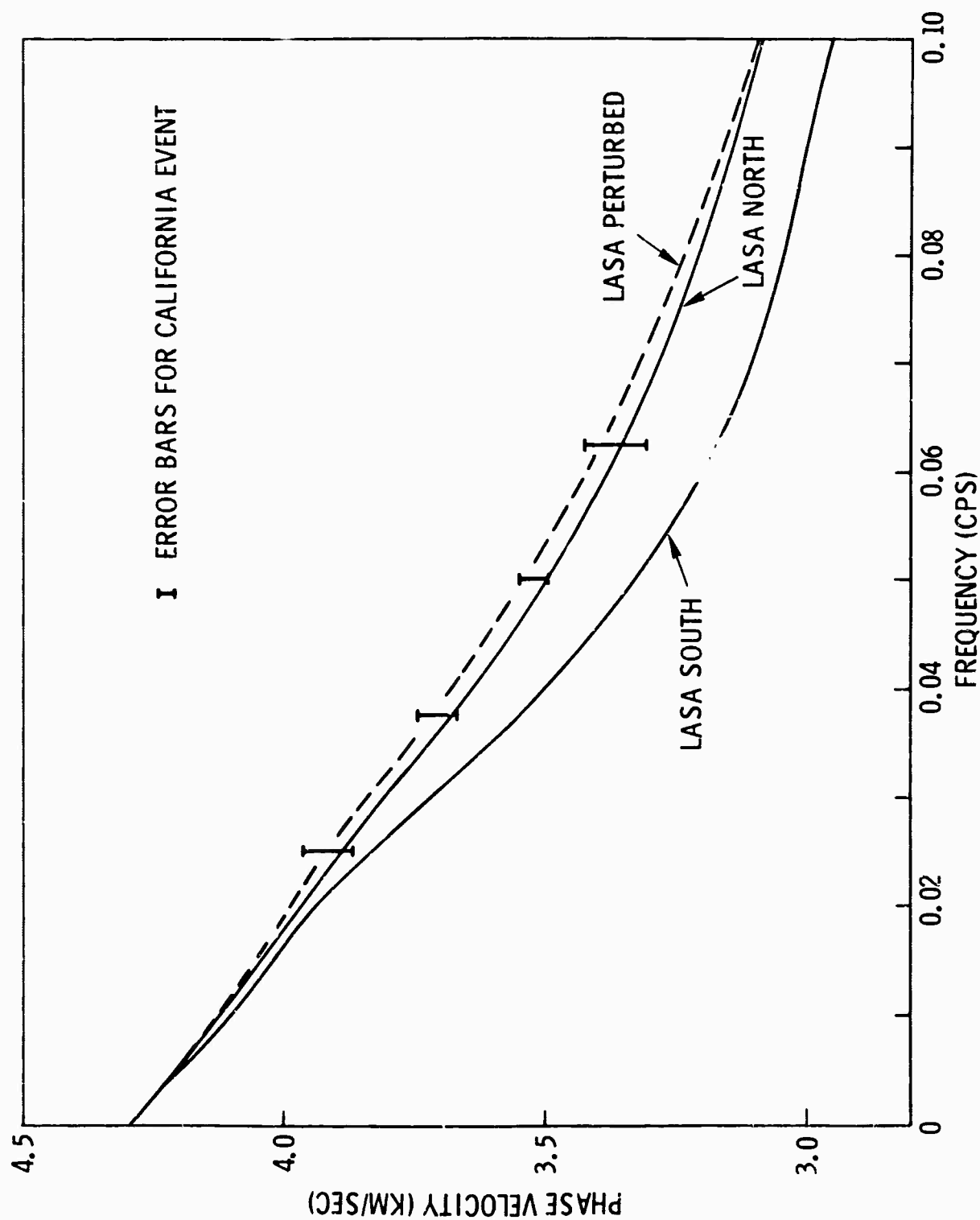
Figure II-23. Rayleigh Dispersion-Error Bars Measured from the California Event (theoretical Rayleigh dispersion curves for three LASA models)
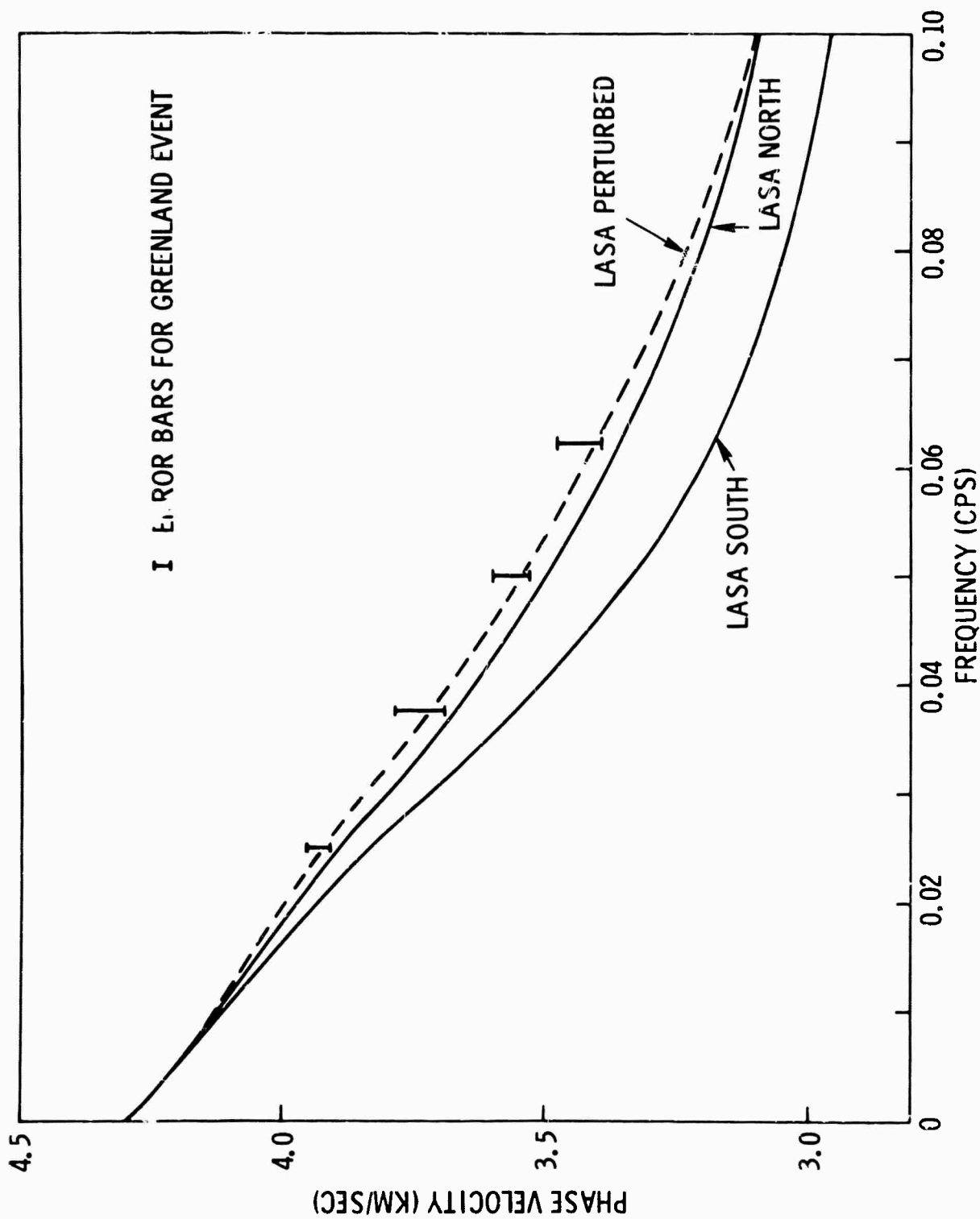
Figure II-24. Rayleigh Dispersion-Error Bars Measured from the Greenland Event (theoretical Rayleigh dispersion curves for three LASA models)

Although the results obtained here cover a narrow frequency band, theoretical predictions, based on the LASA crustal model shown in Table II-5, indicate that the greatest dispersion for the M11 mode is observed in this band. The perturbed LASA model developed here (Table II-5) is the best obtainable model with the available refraction and dispersion data. Higher order modes or additional refraction data from future studies might allow refinements in the present model.

Table II-5

PHYSICAL PARAMETERS

FOR

PERTURBED LASA CRUSTAL MODEL

Layer	Compressional Velocity, α (km/sec)	Shear Velocity, β (km/sec)	Layer Thickness (km)
1	2.60	1.50	0.3
2	3.70	1.85	2.0
3	6.08	3.51	15.0
4	6.97	4.11	17.0
5	7.58	4.47	23.0
Half-space	8.07	4.67	∞

For a future study, it would be useful to plot the relative arrival time of the wavefront at each recording station in the array. This would provide a contour map of the wavefront as it passes across LASA so that the curvature and wavefront changes could be checked. Even more desirable would be to develop a contour map of velocities for LASA by computing dispersion estimates between various tripartite systems.

By selection of events and recording stations so that one leg of the triangle is in line (as nearly as possible) with the event, best velocity estimates can be obtained. The wavefront direction can be obtained best by choosing stations so that the propagation vector lies between the two legs of the triangle.

Using a sufficient number of events, dispersion estimates can be computed accurately for all the LASA sites; therefore, the precise nature of the LASA crustal model can be determined.

The results obtained from the California and Greenland events agree qualitatively with the results of Steinhart and Meyer.[2] As seen in Figure II-1, the dimensions of the array recording these two events are much less than the dimensions available to Steinhart and Meyer.

SECTION III
ANALOG MODEL STUDIES

A. INTRODUCTION

Earthquakes from a given area typically possess the same first motion at a given distant station, making possible establishment of regional patterns for the first part of the observed seismic waveforms. Such empirical observations suggest that the complexity of a teleseismic event may be partially attributed to local and regional geological discontinuities, i.e., to layers and/or irregularities within the crust and the upper mantle.

Observation of seismic surface waves having properties in agreement with Love's theoretical predictions has substantiated the existence of geological layers in the crust. However, while the concept of geological layers is a useful interpretative tool, a clear evaluation of its efficacy is lacking.

Many investigators have submitted evidence for two or more distinct layers within the earth's crust, separated by discontinuities in velocity or by sharp gradients. Others have found this evidence of distinct layers ambiguous and emphasized the incoherent and random character of typical field data. One persistent and important uncertainty is the amount of bodywave conversion into surface waves due to internal (volume) scattering and to topographic scattering.

The implication of such opposing interpretations is that the earth's crust, though layered, is also heterogeneous and aeolotropic, which makes it difficult to isolate and evaluate the numerous parameters associated with a layered crust. Their absolute and relative importance is masked by factors about which little is known.

science services division

To identify and better understand the essential elements of a randomly inhomogeneous earth crust possessing some systematic layering, it is necessary to suppress the statistical, nondeterministic quantities in field seismograms and to deal only with simple layers. One approach is to study a controlled laboratory model of the earth crust rather than real earth crust. The study of scattering and phase conversion, crustal reverberation, and modal propagation becomes considerably more tractable by using model data. Apart from the geometrical and material uniformity posse by such a physical model, more knowledge and control of the all-imp...ant source spectrum are achieved. Much of this report is concerned with the explanation of controlled experiments in seismology, aimed at better understanding the scattering of elastic waves and their propagation in layered media.

The analog model used in these studies (designated model H-6) was described in the Crustal Studies Annual Report.[1]

Recordings from additional source-receiver configurations were obtained using this analog model. Teleseismic signals generated with the source located on the bottom of the model were used to study the effects of lateral inhomogeneity and reverberation. Data were also recorded with the source located on the surface of the 5-cm end of the model to study mode propagation across the lateral inhomogeneity. Figure III-1 shows the analog model (model H-6) and the positions of the source crystal for these two types of studies.

Further calculations were performed using the data recorded with the two surface scatterers in position.

B. SCATTERING OF SURFACE WAVES DUE TO LATERAL INHOMOGENEITY

The analog model was set up as shown in Figure III-1 with the surface source placed on the thick (5-cm) end of model H-6. Results with the source crystal located on the surface of the thin end of the model were shown in the Crustal Studies Annual Report.[1]
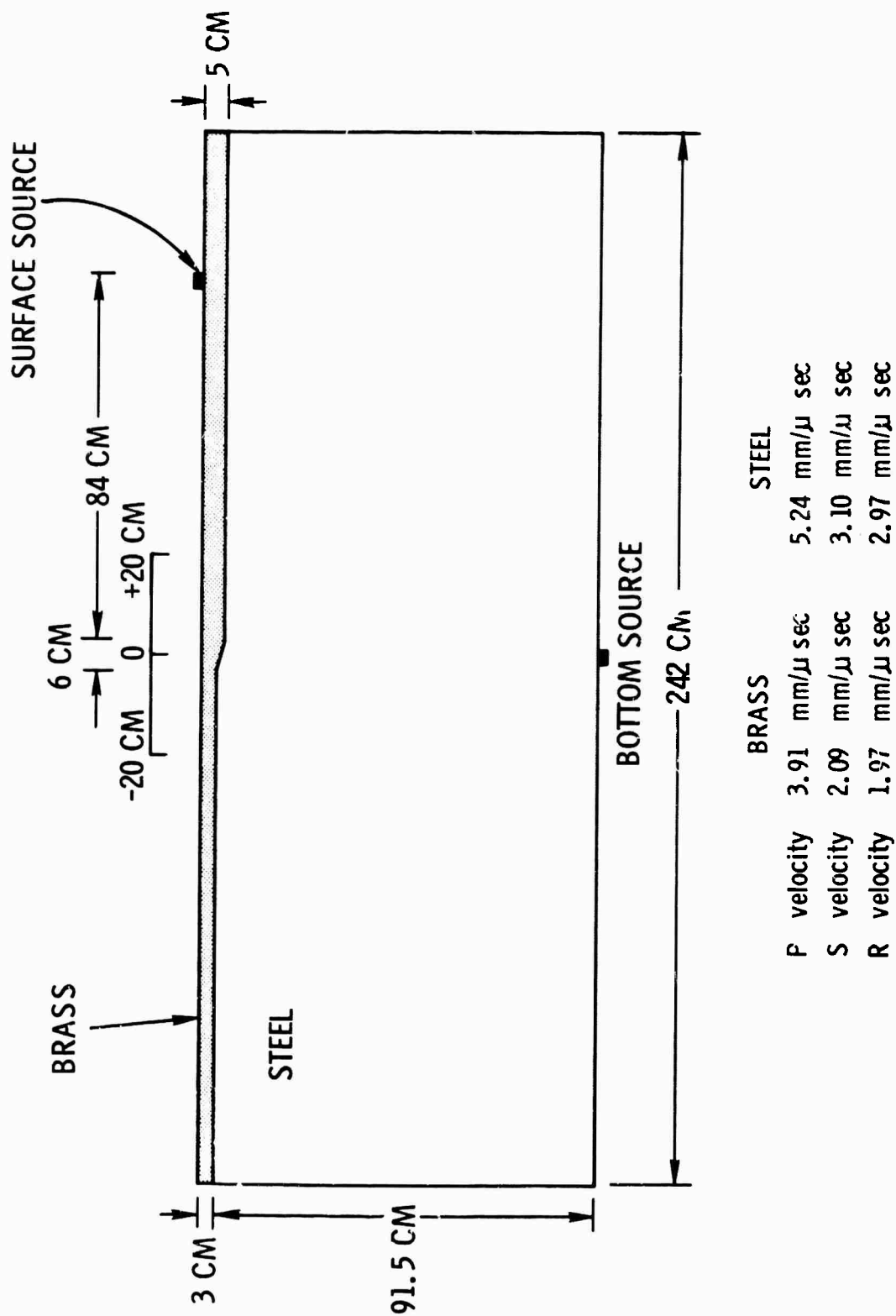
Figure III-1. Diagram of Model H-6

science services division

With the source positioned at the 5-cm end of the model, re-
cordings of the vertical component of motion were made at 1-cm intervals
along the surface of the model. Both high-gain and low-gain recordings
(Figures III-2 and III-3) were made to insure optimum recognition of both
weak and strong signatures.

Refracted energy crossing the dipping segment of the model
has two distinct paths. One path corresponds to a ray, traveling entirely
along the brass-steel interface in the steel half-space. The other path cor-
responds to a ray, propagating directly through the steel half-space, be-
ginning at the thick-crust end of the lateral discontinuity and continuing to
the thin-crust end. Theoretical travel-time curves for the two rays differ
at most by 0.5 μsec and thus are represented by one curve in Figure III-4.
This figure displays theoretical travel-time vs distance for seven rays of
potential physical relevance for the model under consideration. Travel times
obtained from the experimental traces appear as small dots on the calculated
travel-time curves. The curves are graphed for locations on both the thin
and thick sides of the model for the direct P phase and the refracted P phase.
There is a jump in the travel-time curve for the refracted P phase as it tra-
verses the lateral discontinuity. Such a jump has been experimentally veri-
fied for ray propagation in both directions across the dipping segment of the
crust.[1] For a source on the thin-crust side, the refracted P travel-time
curve is offset across the transition region; for a source on the thick-crust
side, the offset is in the opposite direction.

Late arriving pulses were traced across small portions of
the experimental records. Travel times associated with these events are
included in Figure III-4. Such events are associated with either later legs
of preceding phases or multiple bounces of earlier refraction and reflection
arrivals.

BLANK PAGE

DISTANCE (CM)

TRANSITION ZONE
LOCATION

TIME (μ-SEC.)
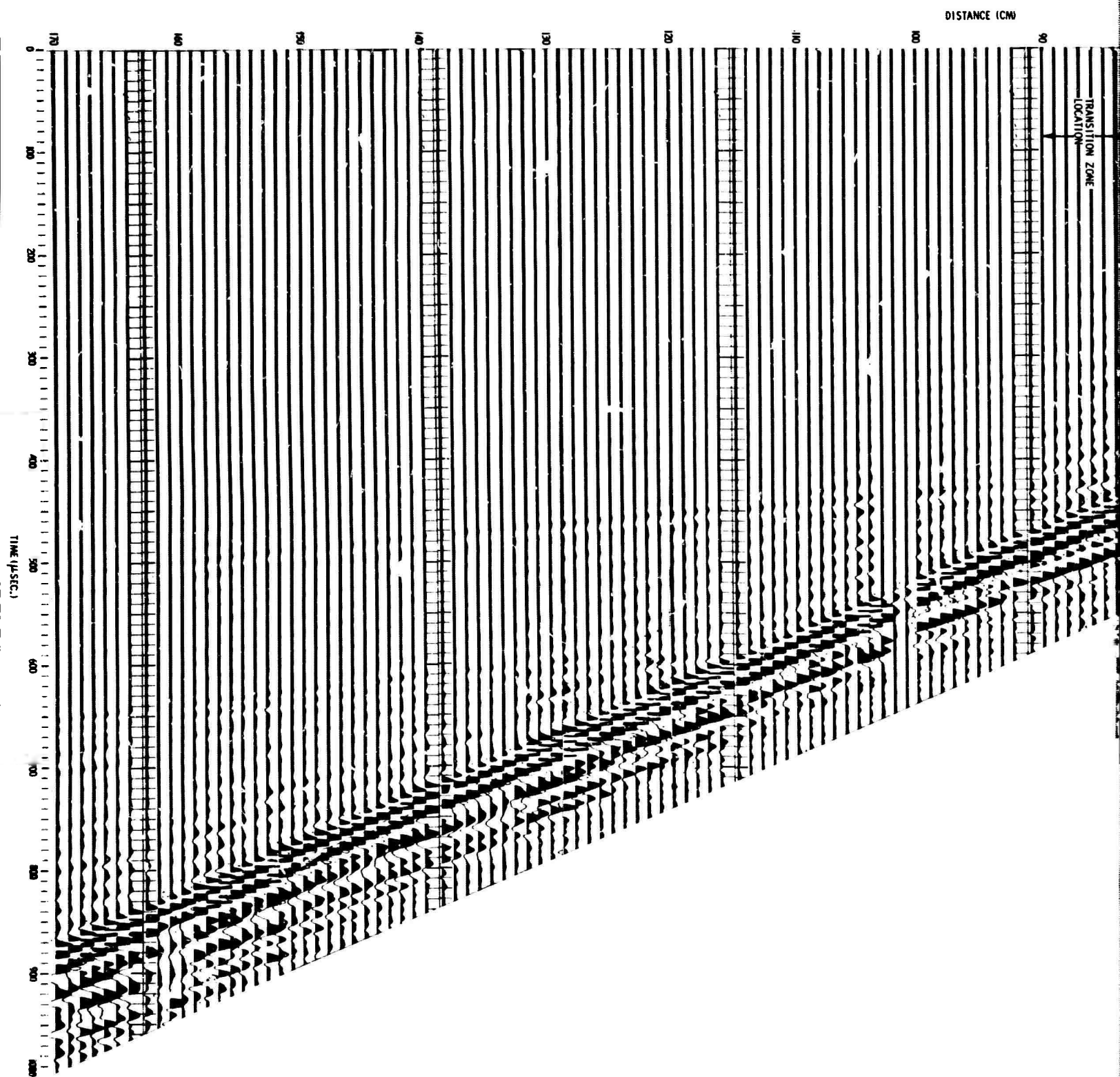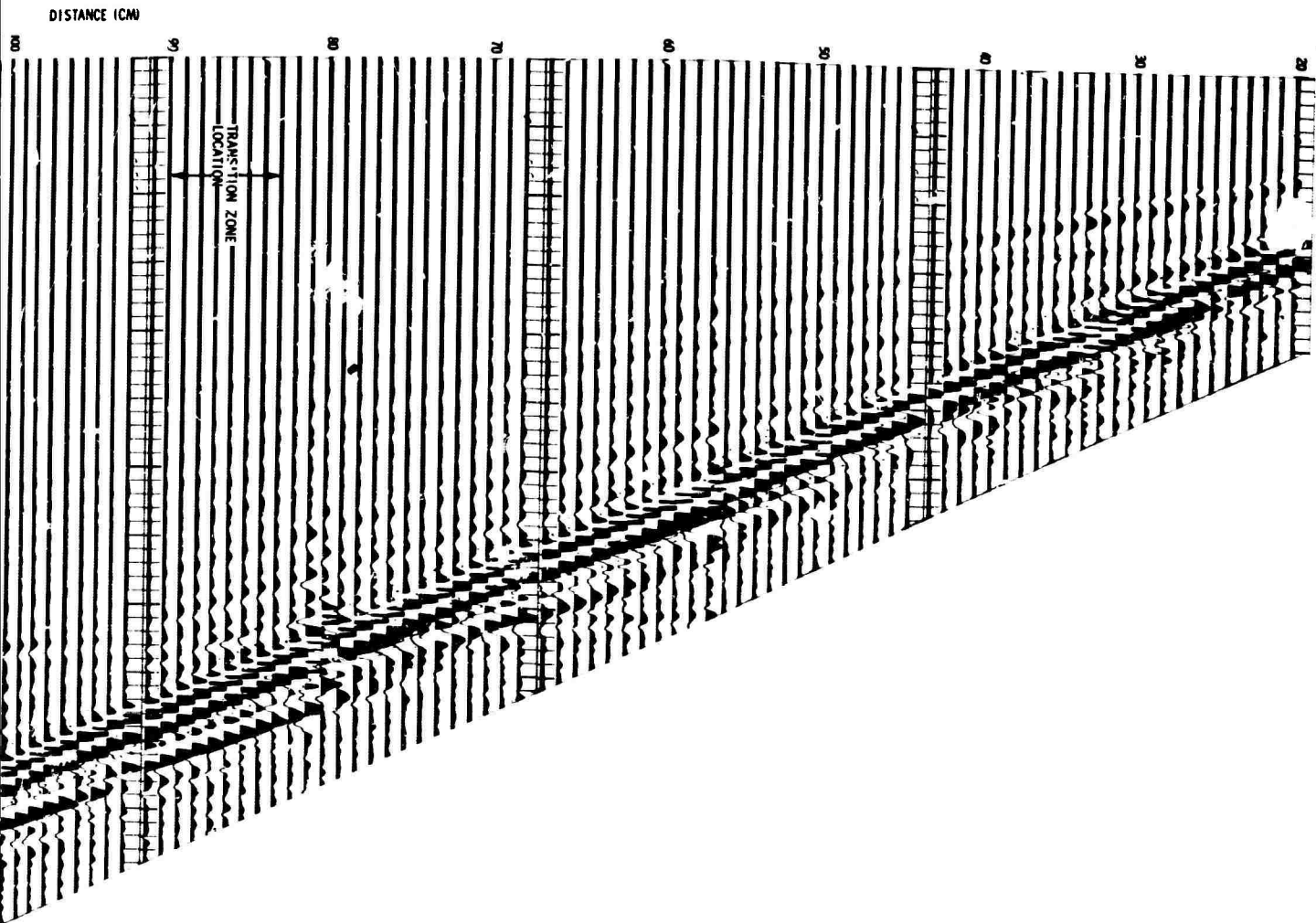
DISTANCE (CM)

Figure III-2. Low-Gain Vertical Recordings Obtained from Model H-6 with the Source Located on the Thick End

DISTANCE (CM)

TRANSITION ZONE LOCATION
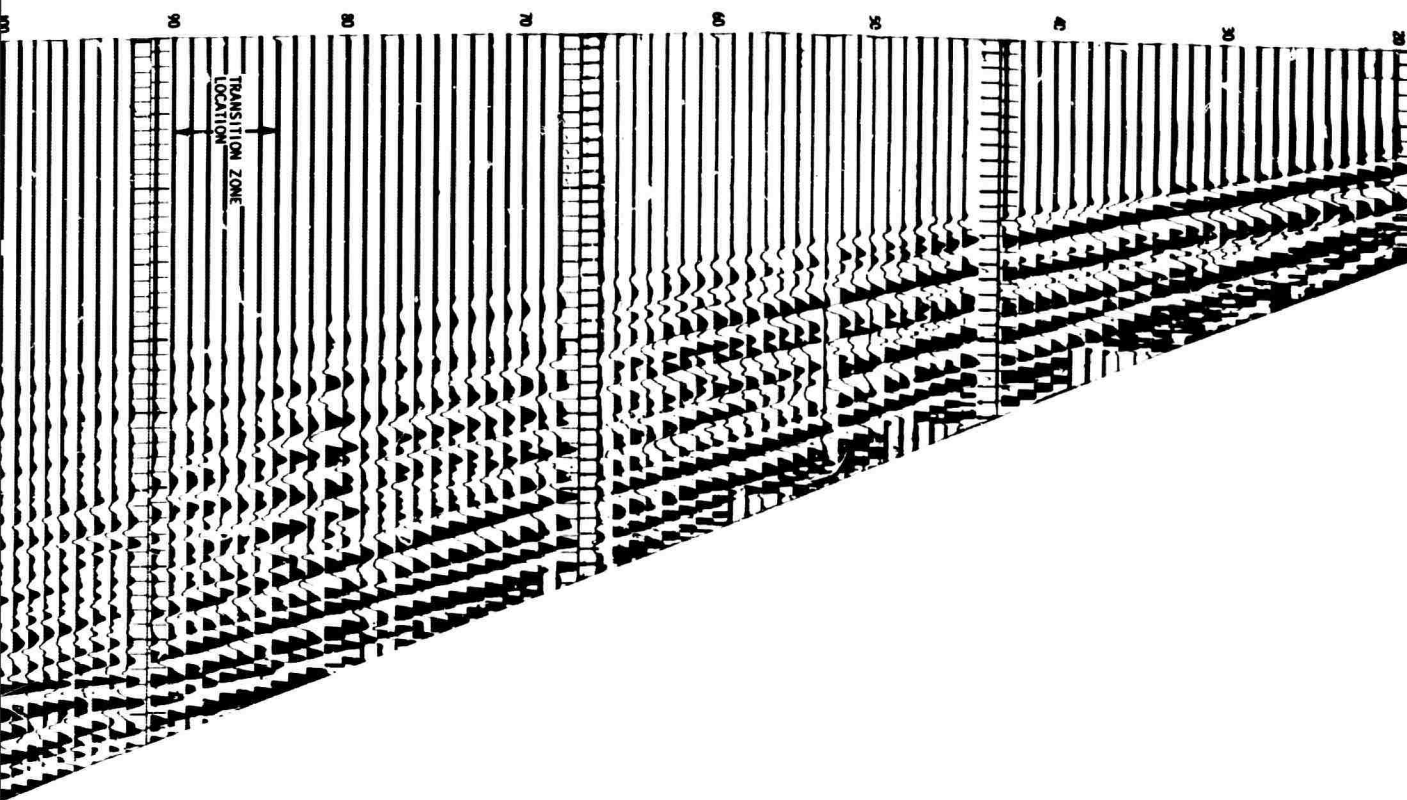
Figure III-3. High-Gain Vertical Recordings Obtained from Model H-6 with the Source Located on the Thick End

BLANK PAGE
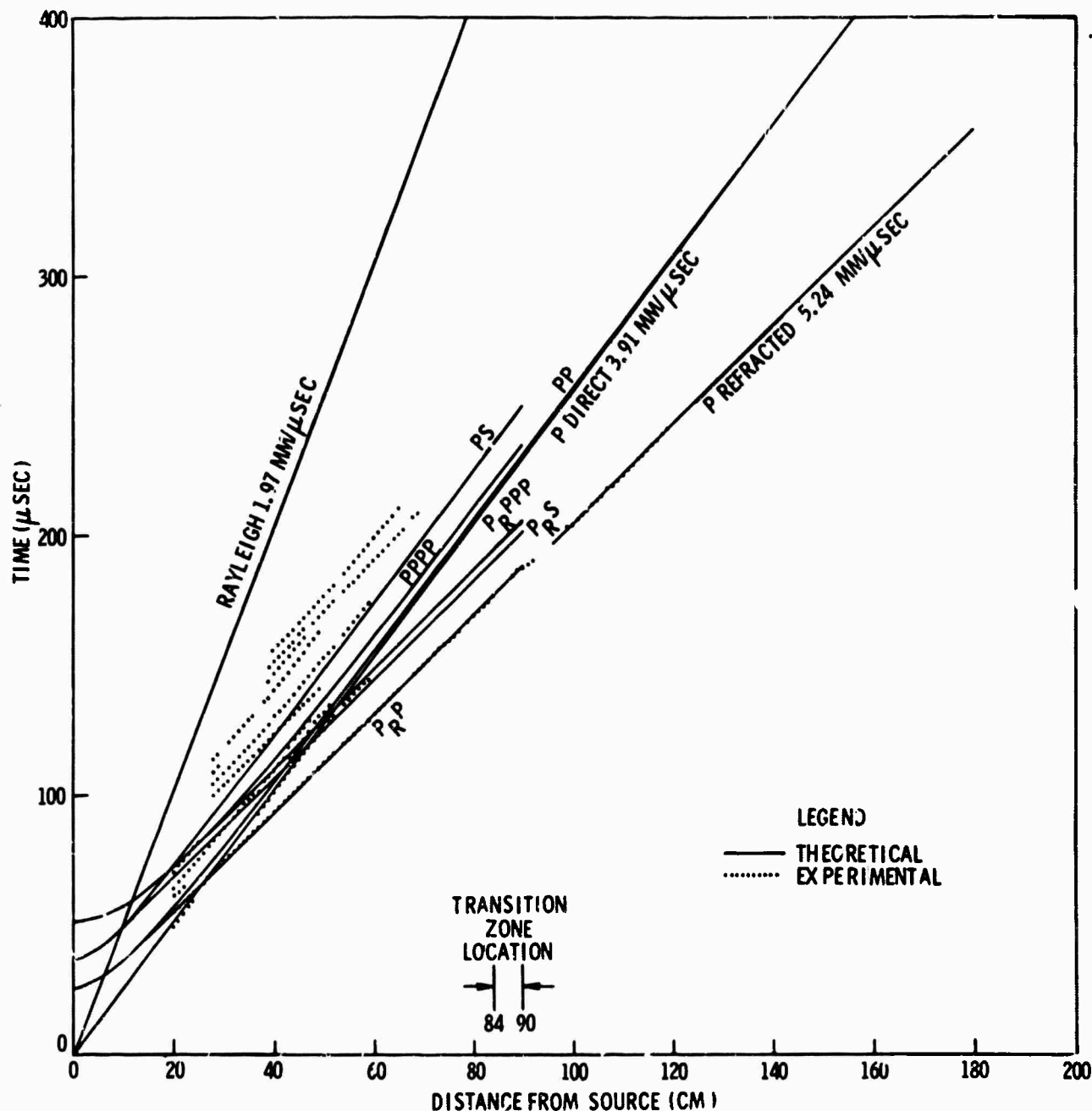
Figure III-4. Travel-Time Curves for Model H-6 with the Source Located on Thick End

Theoretical dispersion curves for the dominant normal and leaking modes of propagation were computed for both the 3-cm and 5-cm end of the crustal model.[1] For reference, the dispersion curves for the 5-cm end are shown in Figure III-5.

Since a complete understanding of a plane-layered model is necessary to fully understand the effects of a lateral inhomogeneity in such models, later subsections deal with plane-layered models from the standpoint of teleseismic signals.

More insight into the nature of the lateral inhomogeneity might be obtained by using different source crystals to excite higher modes of propagation. This is recommended for a future study.

C. SCATTERING FROM SURFACE IRREGULARITIES

Analog model study results of scattering from surface layer irregularities were presented in the annual report.[1] Additional computations using another technique were performed at smaller frequency increments to achieve higher resolution of both the transfer functions and the power spectra.

Figures III-6 through III-11 were shown in the annual report and are presented here for purposes of discussion.

Figure III-6 shows the analog model and the two brass scatterers used.

Figure III-7 shows vertical recordings in variable-area display made along the surface when no scatter was present. The incident Rayleigh mode is the dominant feature of these traces. The nondispersive Rayleigh pulse propagates at 1.97 mm/μsec in the brass layer; higher velocity P- and S-wave energy can be seen earlier on the records but with significantly smaller amplitudes. The high velocity energy appearing later (t = 400 μsec) is a reflection from the bottom of the model.
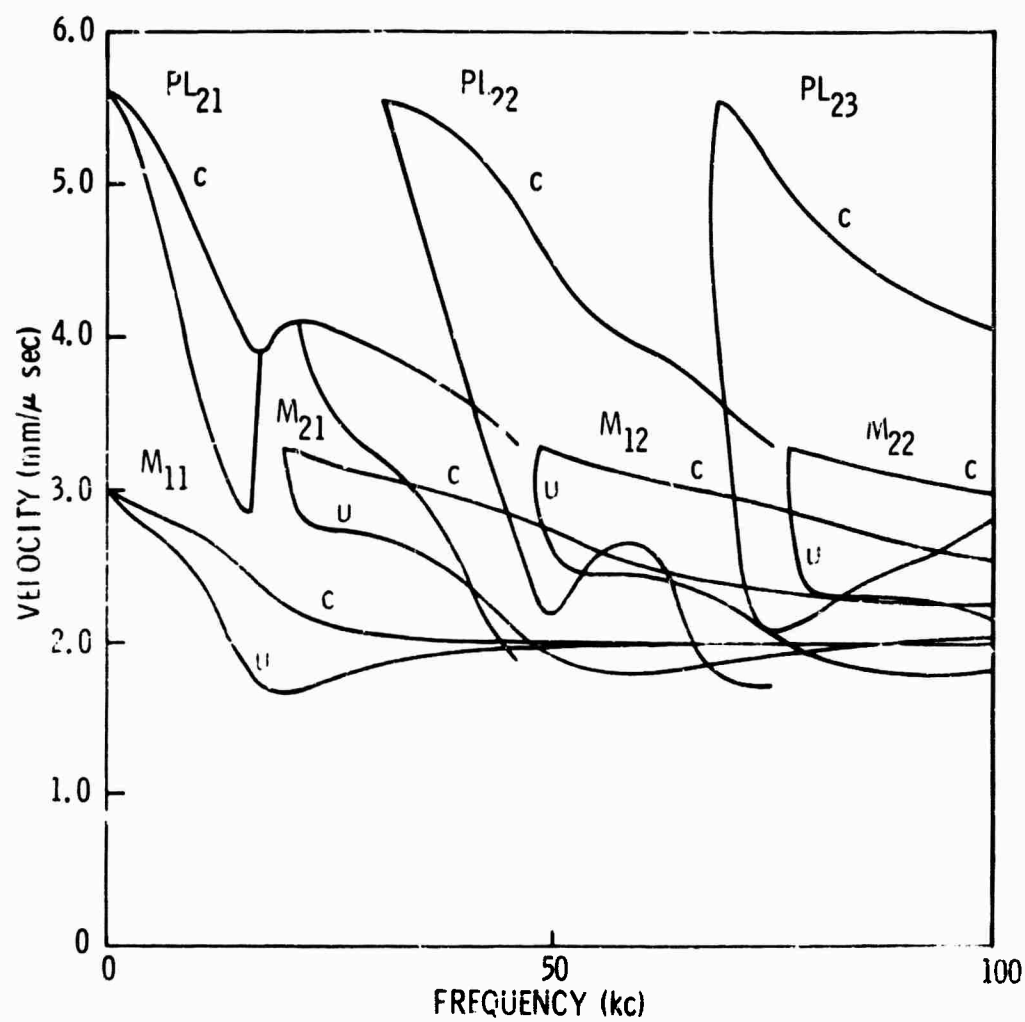
Figure III-5. Dispersion Curves for the Dominant
Normal and Leaky Modes for Model
H-6 (Thick End)

SCATTER
SOURCE   POSITION
BRASS

|←—— 40CM ——→|

3 CM

STEEL

91.5 CM

|←——————— 118 CM ———————→|
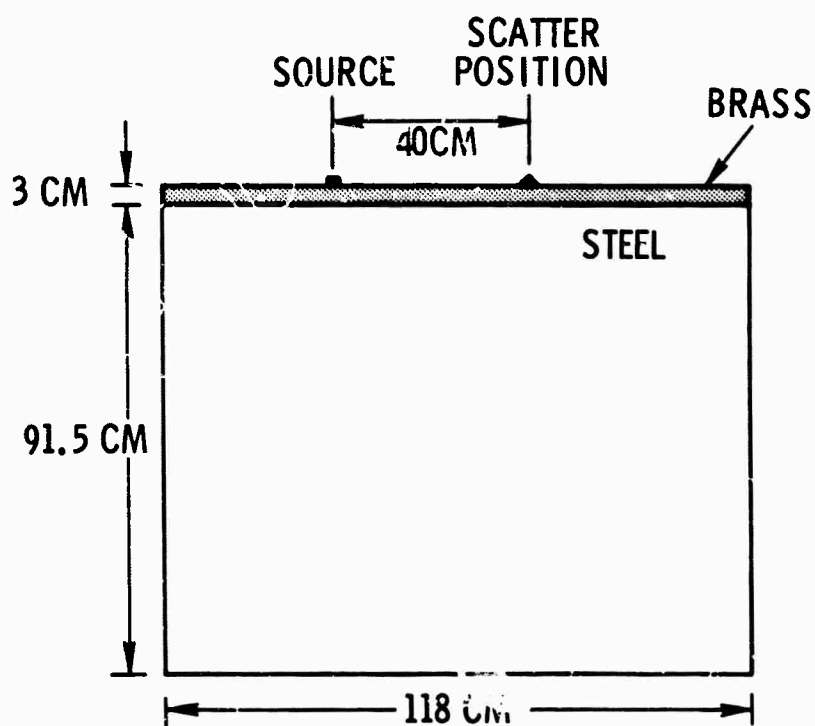
ELASTIC PARAMETERS

		BRASS		STEEL	
P	velocity	3.91	mm/μ sec	5.24	mm/μ sec
S	velocity	2.09	mm/μ sec	3.10	mm/μ sec
R	velocity	1.97	mm/μ sec	2.97	mm/μ sec

3 MM |←—10 MM—→| 3 MM |←—10 MM—→|

(A) SCATTERER 1   (B) SCATTERER 2
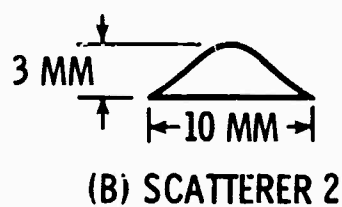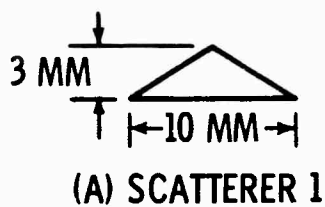
Figure III-6.   Diagram of Model H-6 (Thin End) with Surface Scatterers;
(a) scatterer 1, (b) scatterer 2

science services division
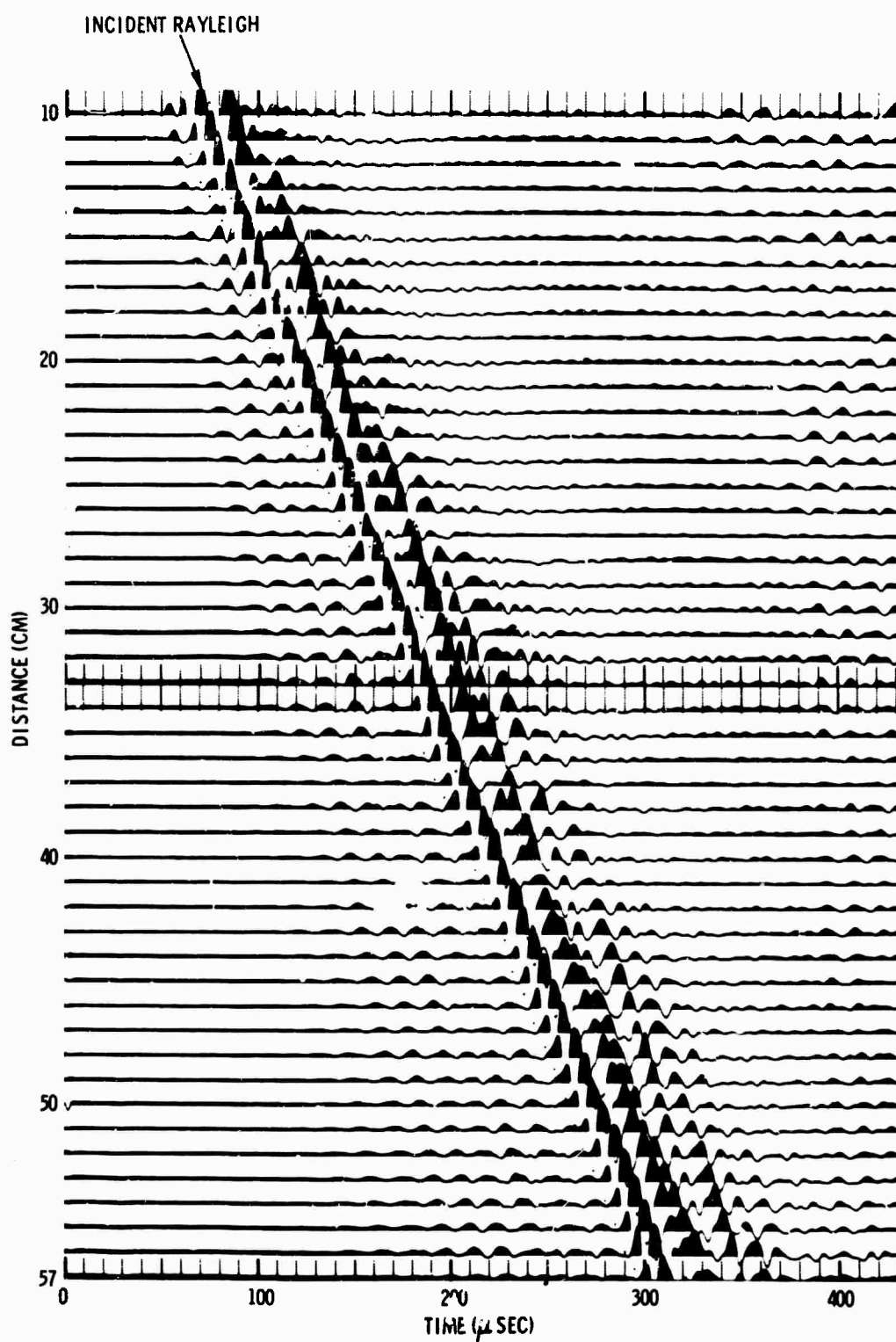
Figure III-7. Low-Gain Vertical Recordings Obtained from Model H-6
(Distance from the source ranges from 10 to 57 cm)

III-13

Figure III-8 shows recordings taken over the same profile when scatterer 1 (triangular-shaped) was in position. A pulse reflected from the scattering center, propagating back toward the source at Rayleigh velocity, is observed.

Recordings with scatterer 2 (Gaussian-shaped) in place are shown in Figure III-9. A similar backscattered pulse is observed. The peak amplitude of the backscattered Rayleigh wave was approximately 1/5 the amplitude of the incident Rayleigh wave.

A comparison of Figures III-8 and III-9 indicates that backscattered energy from scatterer 2 has more low-frequency components than does backscattered energy from scatterer 1.

To isolate incident and backscattered Rayleigh energies, Pie Slice[*] (wideband velocity filtering) was applied to the output traces at ±2.0 mm/μsec.[6] Outputs of the velocity filtering were for receiver locations of 15.5, 24.5, 33.5, 46.5, and 53.5 cm from the source. Filtering results at ±2.0 and -2.0 mm/μsec are shown in Figures III-10 through III-13.

Power spectra of incident Rayleigh (+2.0 mm/μsec) and backscattered Rayleigh (-2.0 mm/μsec) energy were computed using the time gates shown in the figures for output distances of 15.5, 24.5, and 33.5 cm from the source. Typically, power-spectra values of the backscattered energy were 18 to 36 db below the values of the incident energy. Power spectra curves for both scatterers are shown in Figures III-14 through III-19. Figures III-20 and III-21 show the power spectra of the incident Rayleigh wave at output distances of 46.5 and 53.5 cm for scatterers 1 and 2, respectively.

---

[*]GSI Service Mark
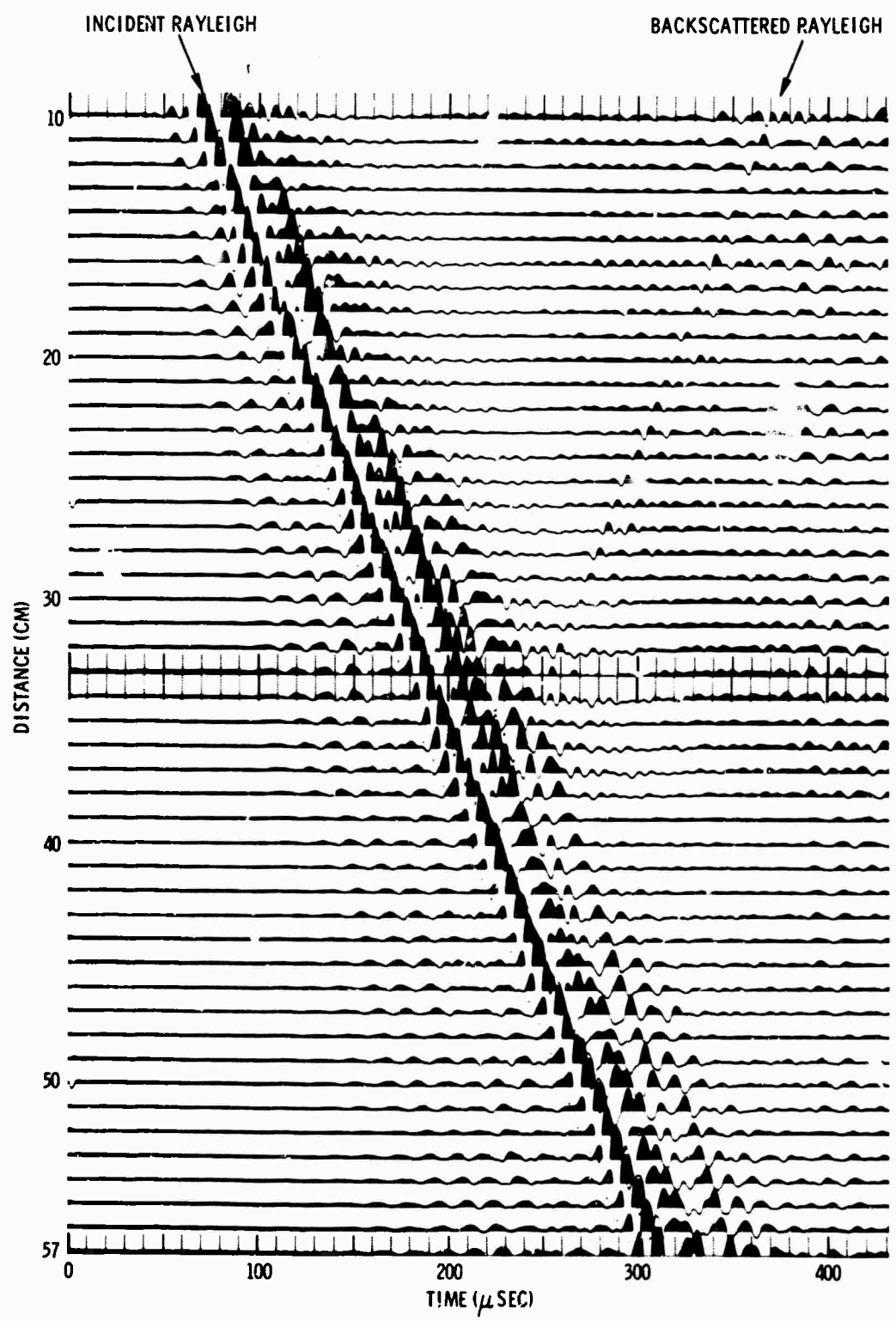
Figure III-8. Low-Gain Vertical Recordings Obtained from Model H-6 with Scatterer 1 (Distance from the source ranges from 10 to 57 cm)

science services division
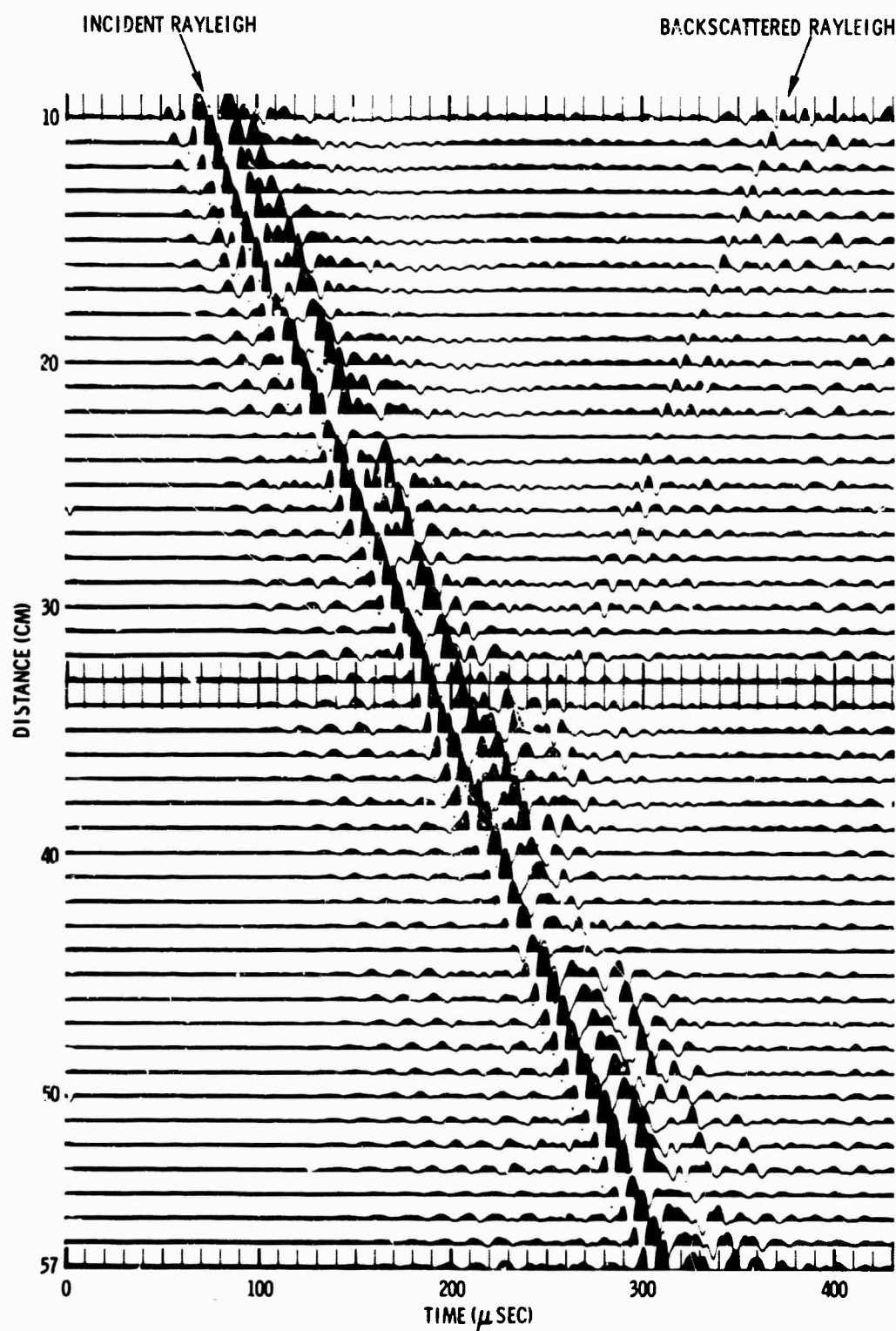
Figure III-9. Low-Gain Vertical Recordings Obtained from Model H-6 with Scatterer 2 (Distance from the source ranges from 10 to 57 cm)

science services division
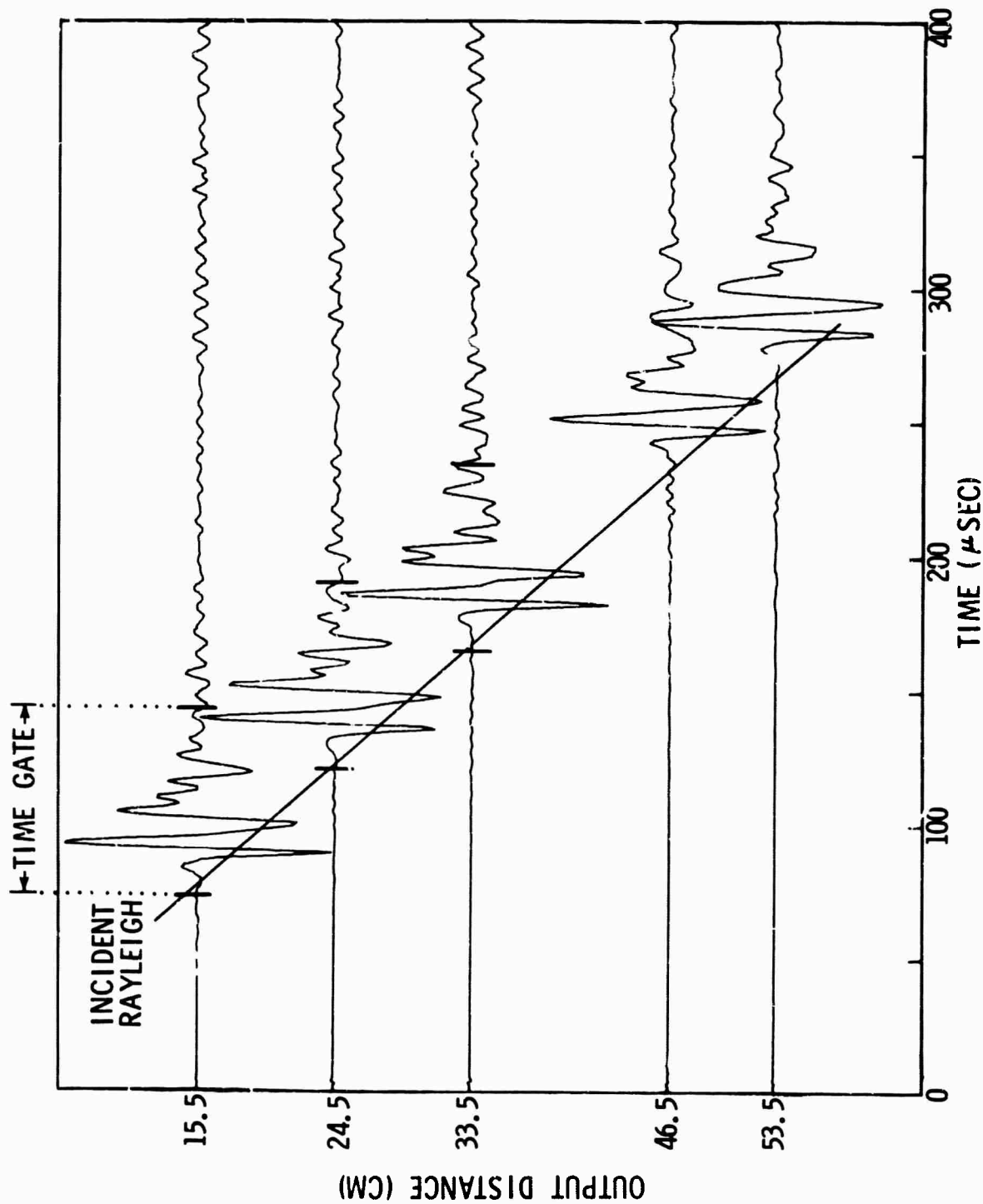
Figure III-10. Pie Slice Output for Scatterer 1 at a Velocity of +2.0 mm/μsec (Output distances are 15.5, 24.5, 33.5, 46.5, and 53.5 cm)
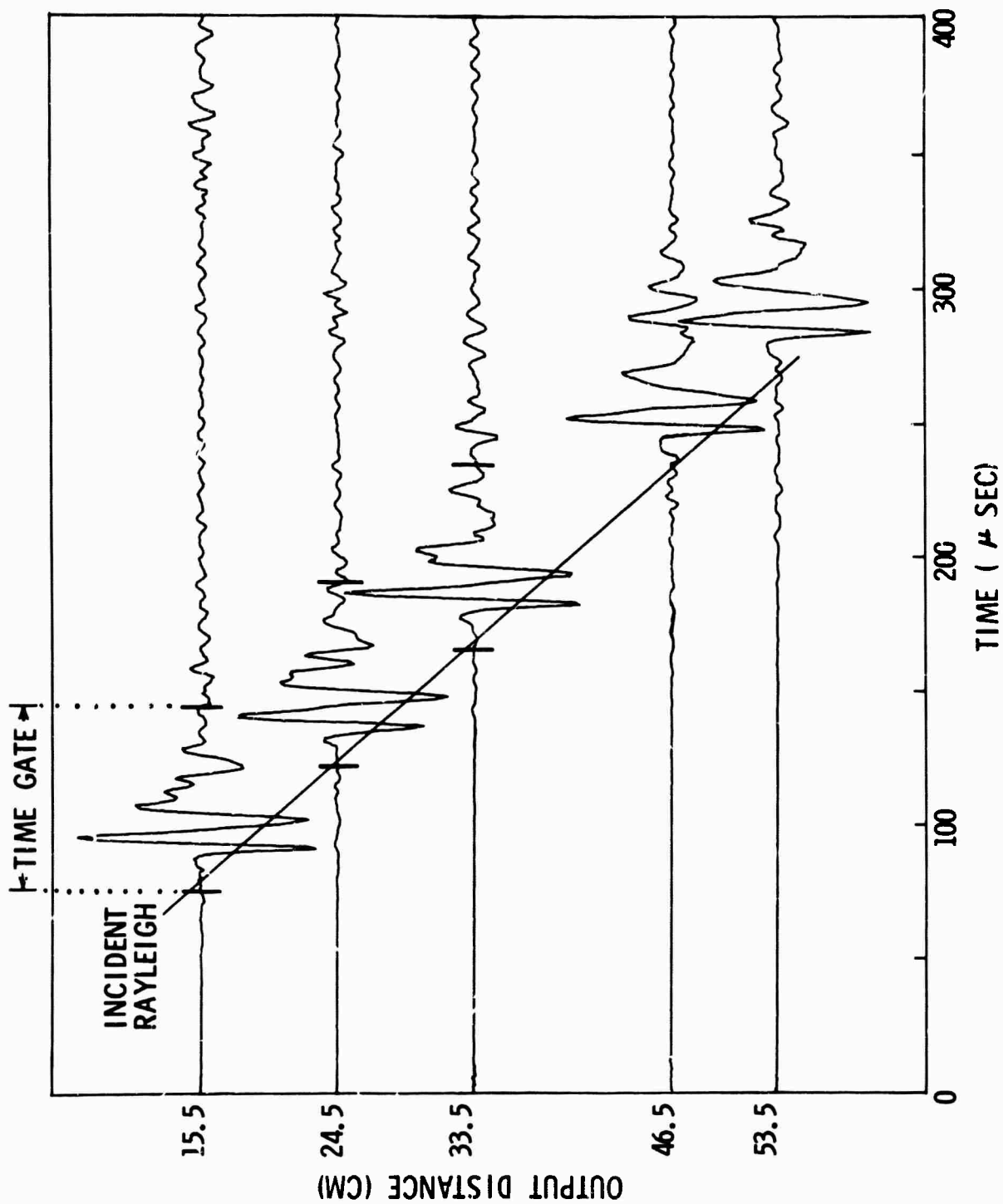
Figure III-11. Pie Slice Output for Scatterer 2 at a Velocity of +2.0 mm/μsec (Output distances are 15 5, 24.5, 33.5, 46.5, and 53.5 cm)

science services division
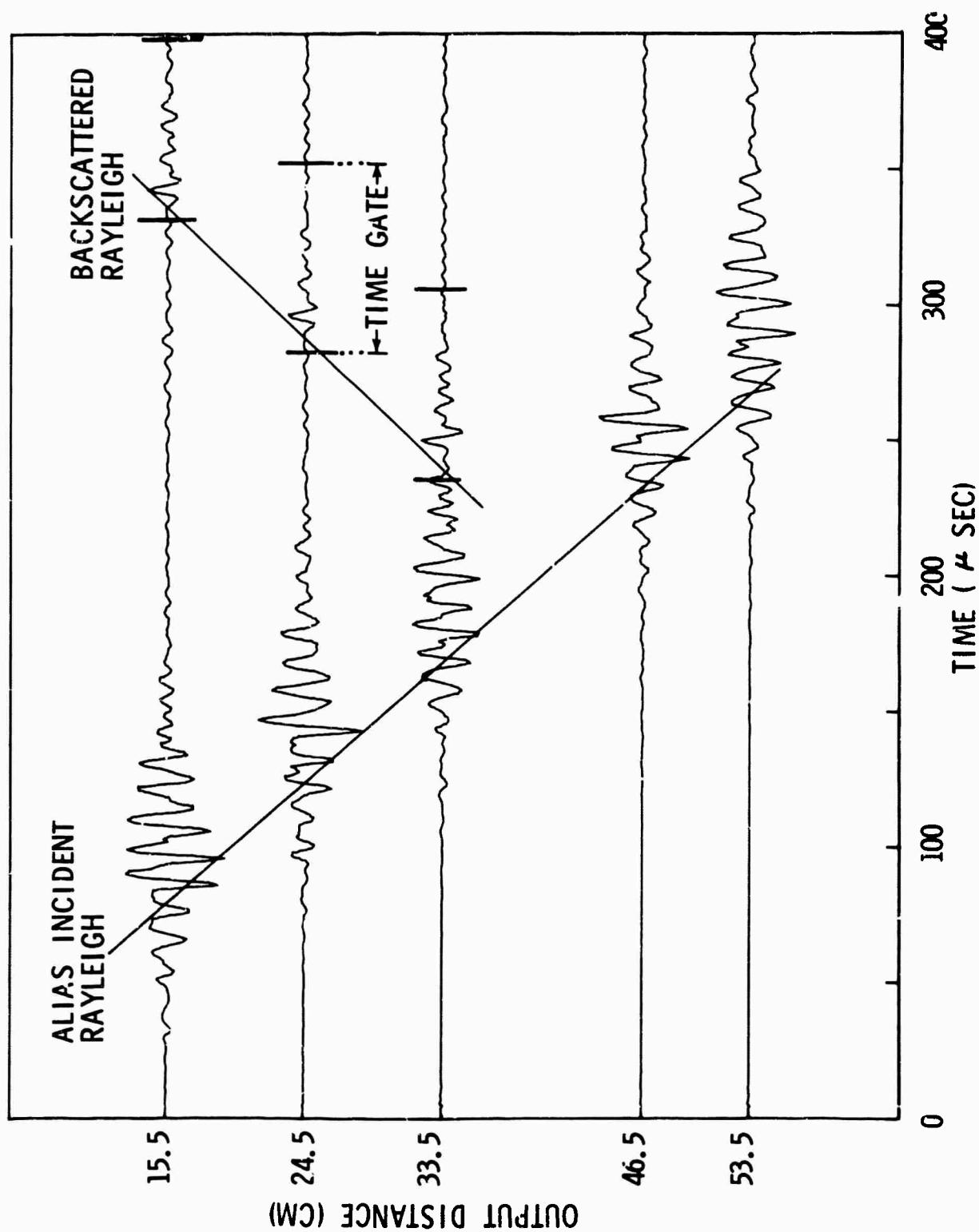
Figure III-12. Pie Slice Output for Scatterer 1 at a Velocity of -2.0 mm/μsec (Output distances are 15.5, 24.5, 33.5, 46.5, and 53.5 cm)

science services division
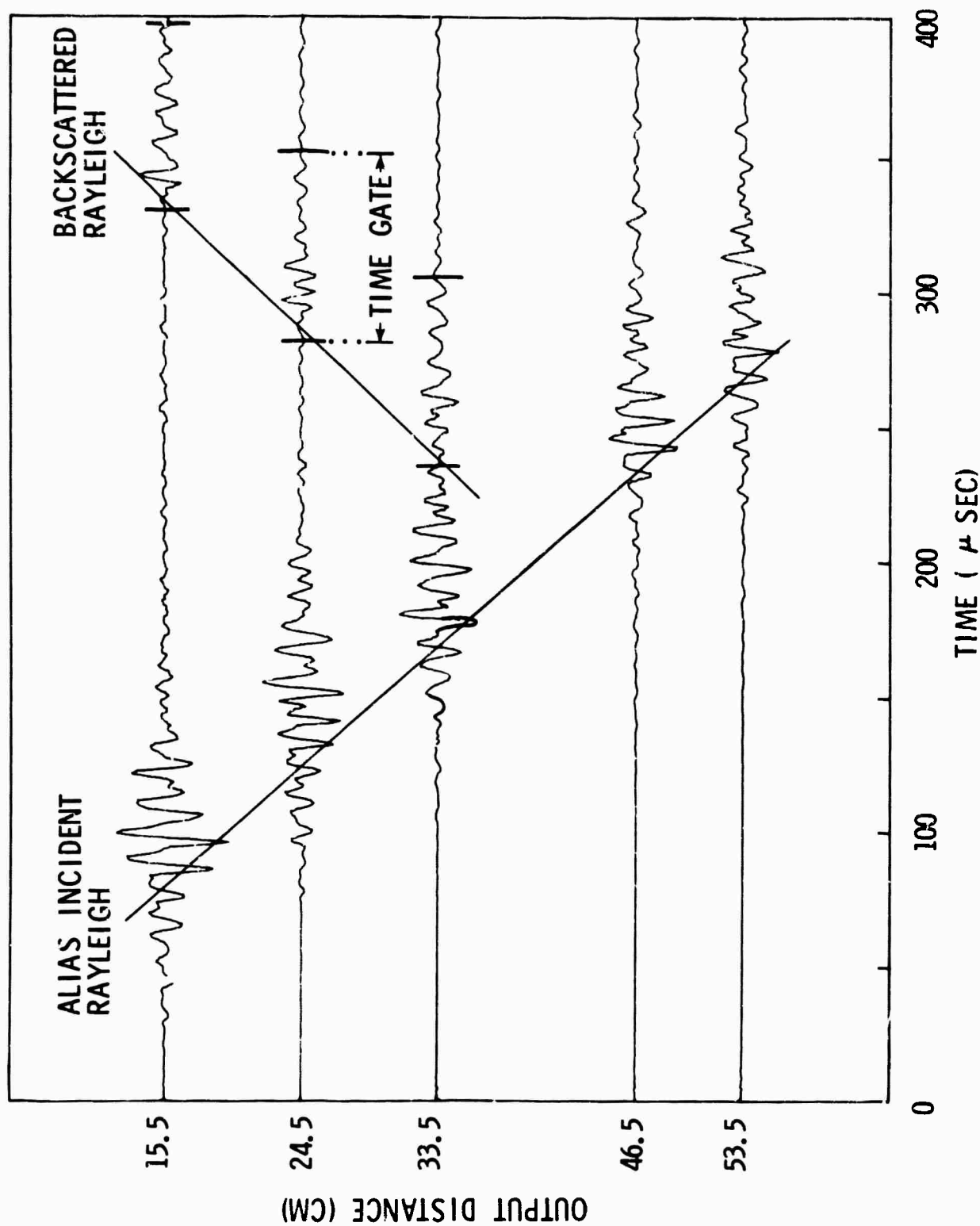
Figure III-13. Pie Slice Output for Scatterer 2 at a Velocity of -2.0 mm/μsec (Output distances are 15.5, 24.5, 33.5, 46.5, and 53.5 cm)

science services division
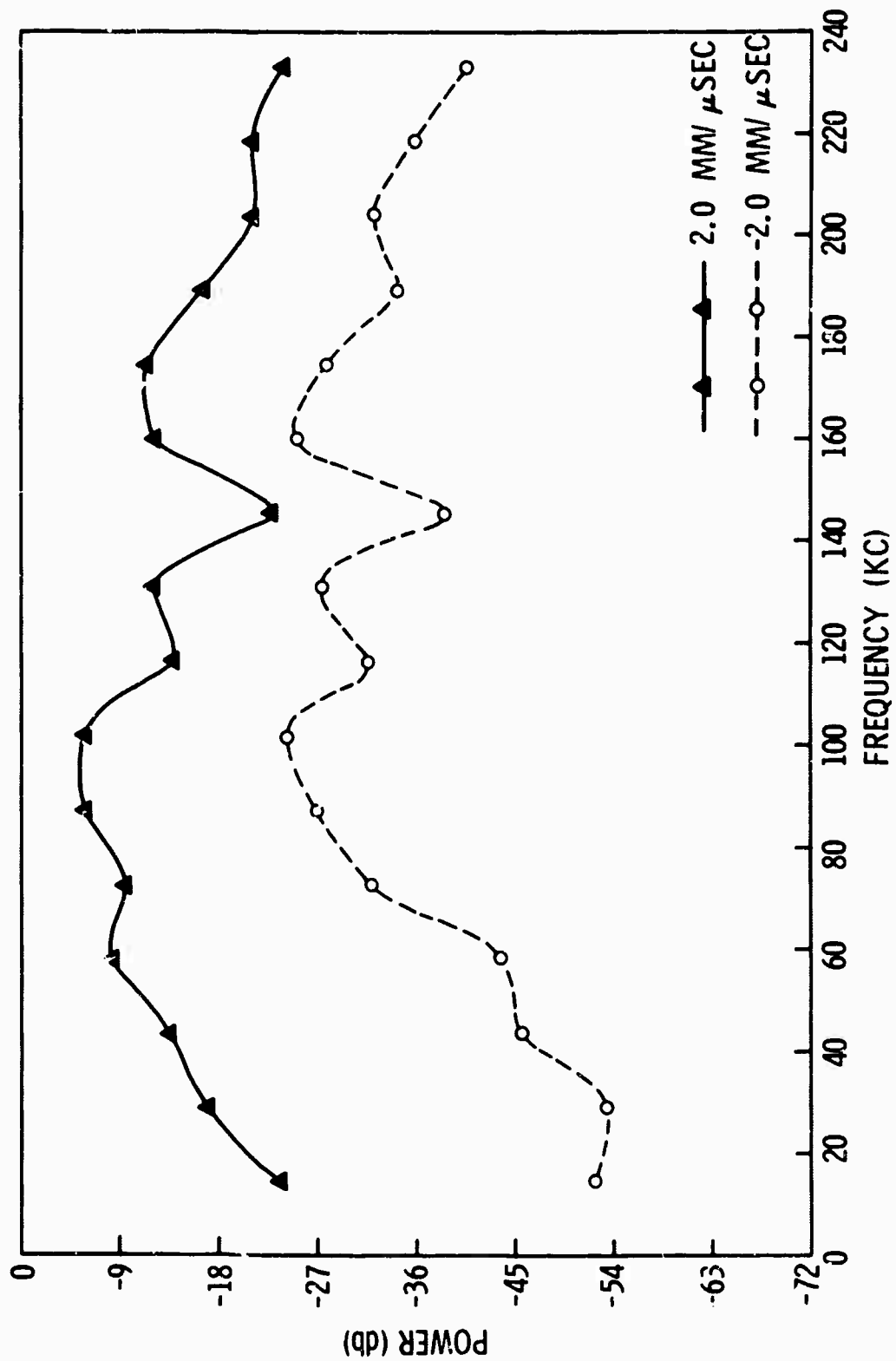
Figure III-14. Relative Vertical Power Spectra of Incident Rayleigh Mode and Backscattered Energy at 15.5 cm from Source Using Scatterer 1

science services division
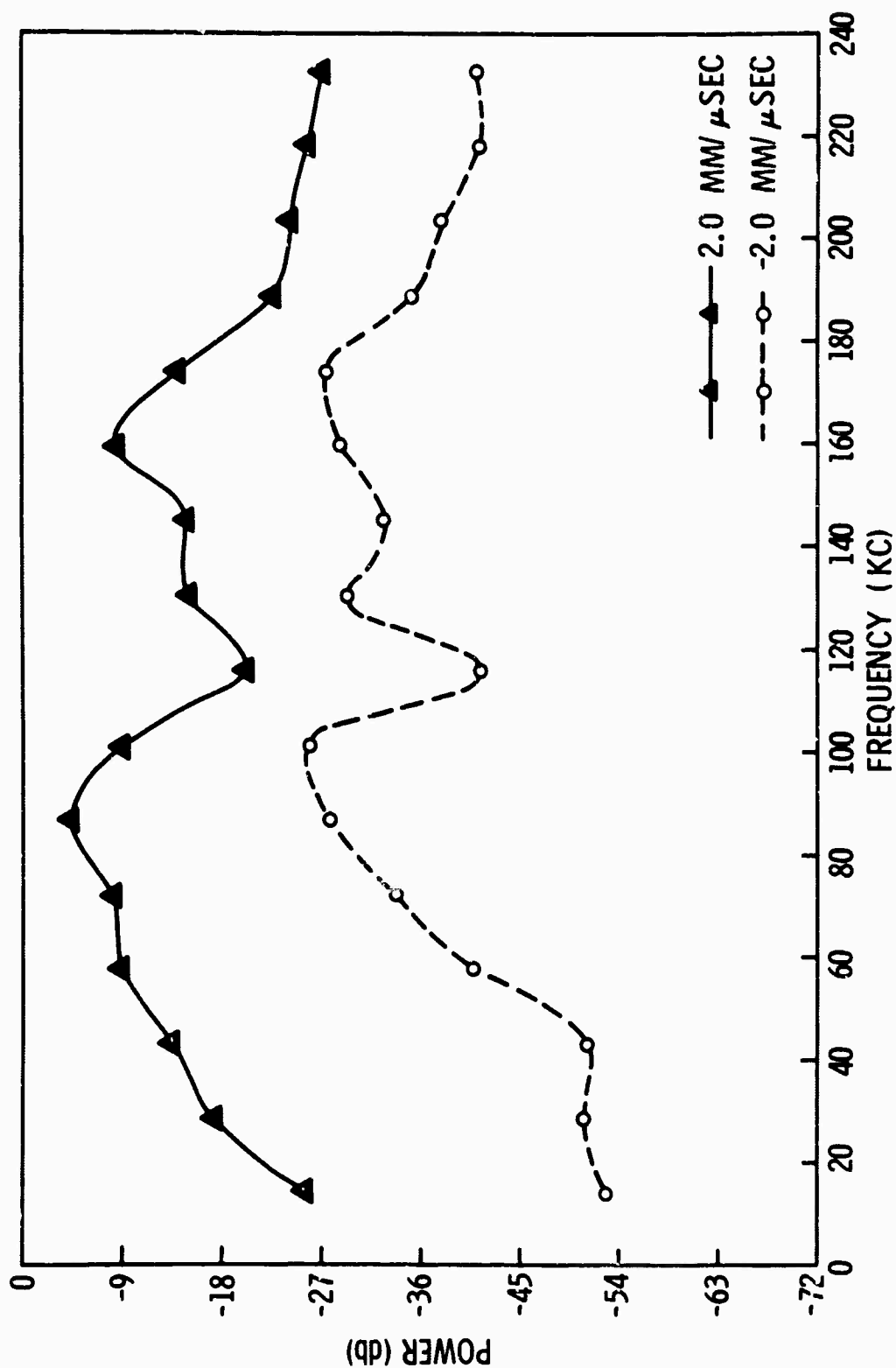
Figure III-15. Relative Vertical Power Spectra of Incident Rayleigh Mode and Backscattered Energy at 24.5 cm from Source Using Scatterer 1

science services division
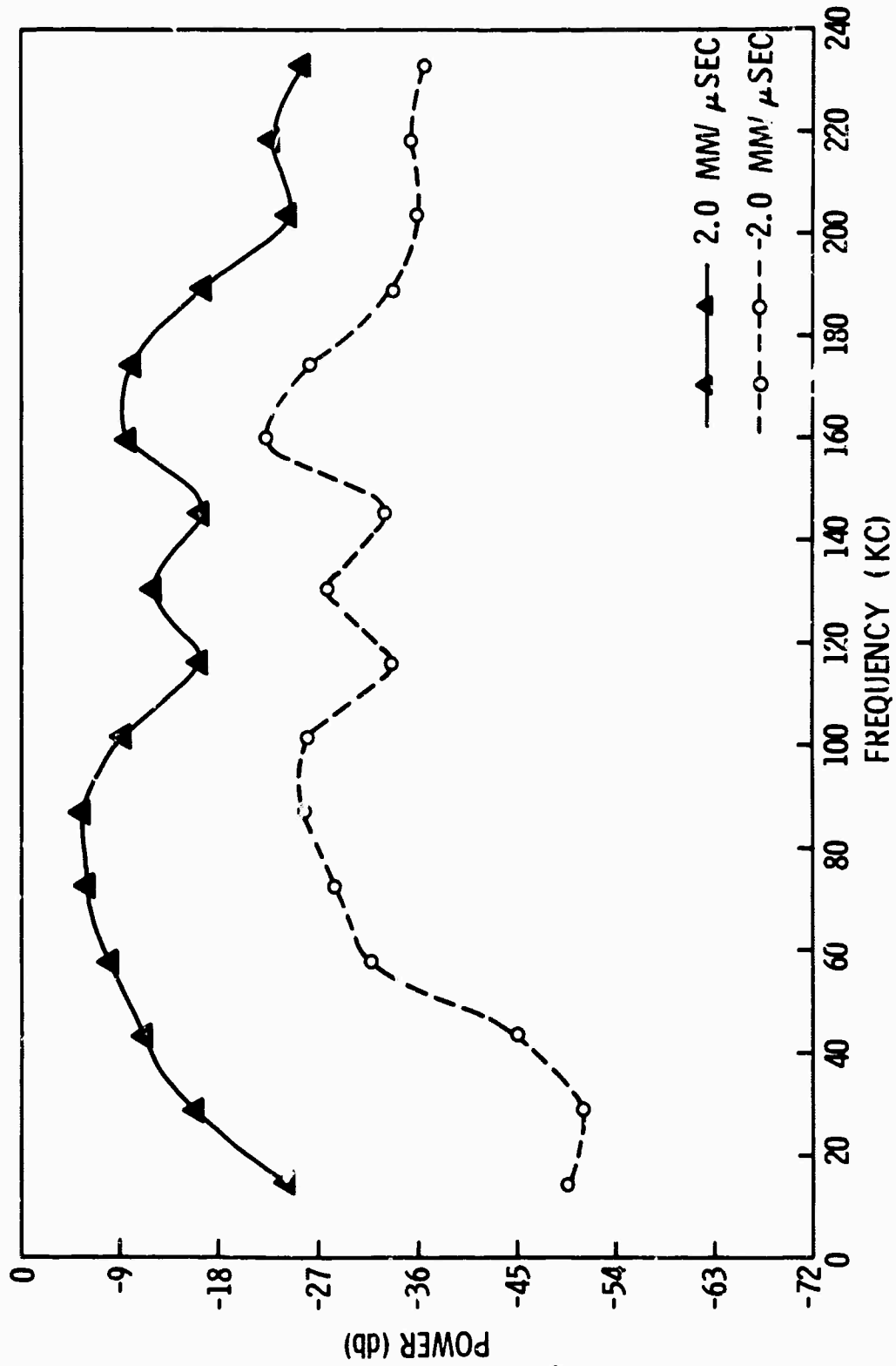
Figure III-16. Relative Vertical Power Spectra of Incident Rayleigh Mode and Backscattered Energy at 33.5 cm from Source Using Scatterer 1

science services division
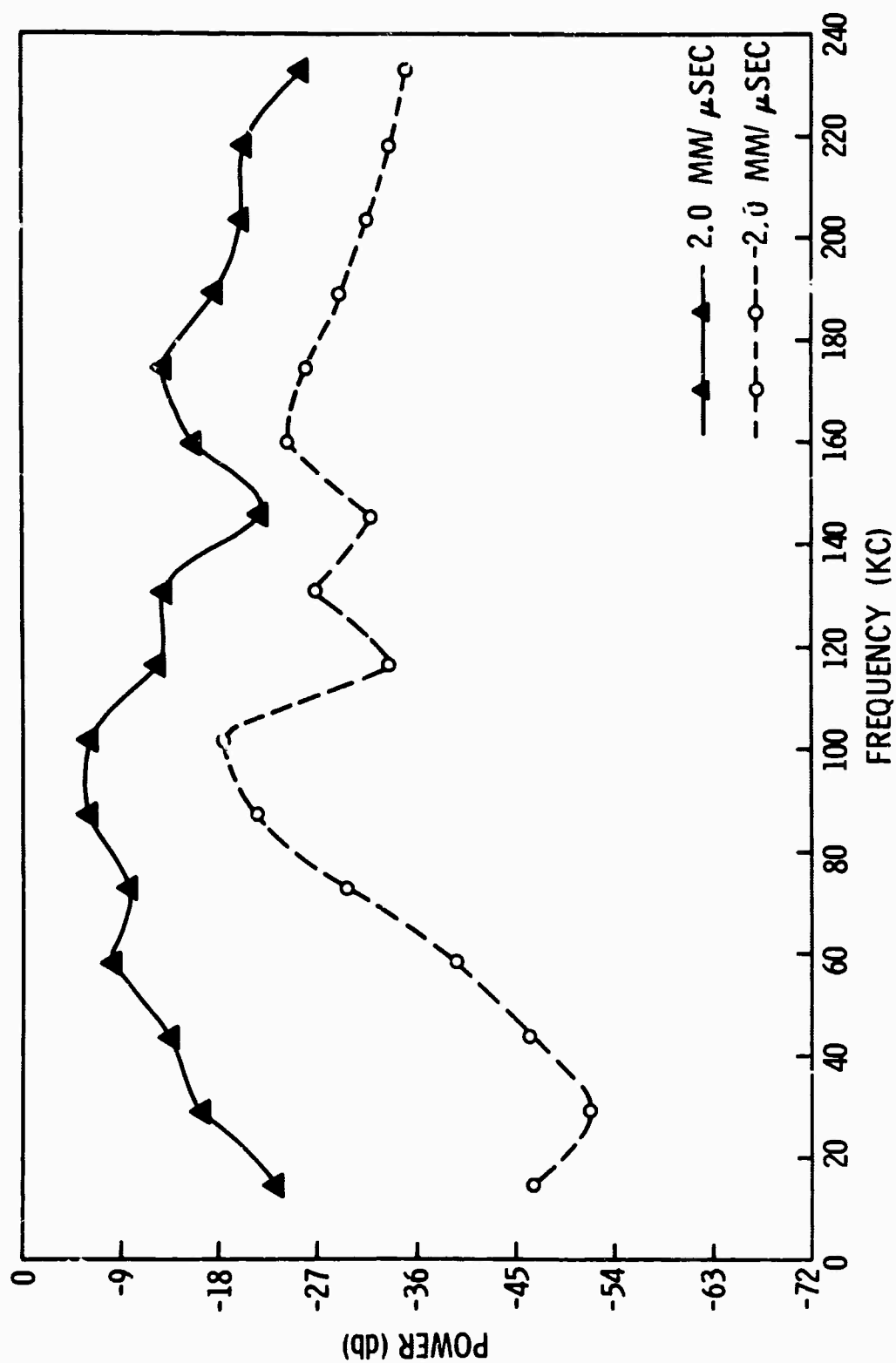
Figure III-17. Relative Vertical Power Spectra of Incident Rayleigh Mode and Backscattered Energy at 15.5 cm from Source Using Scatterer 2
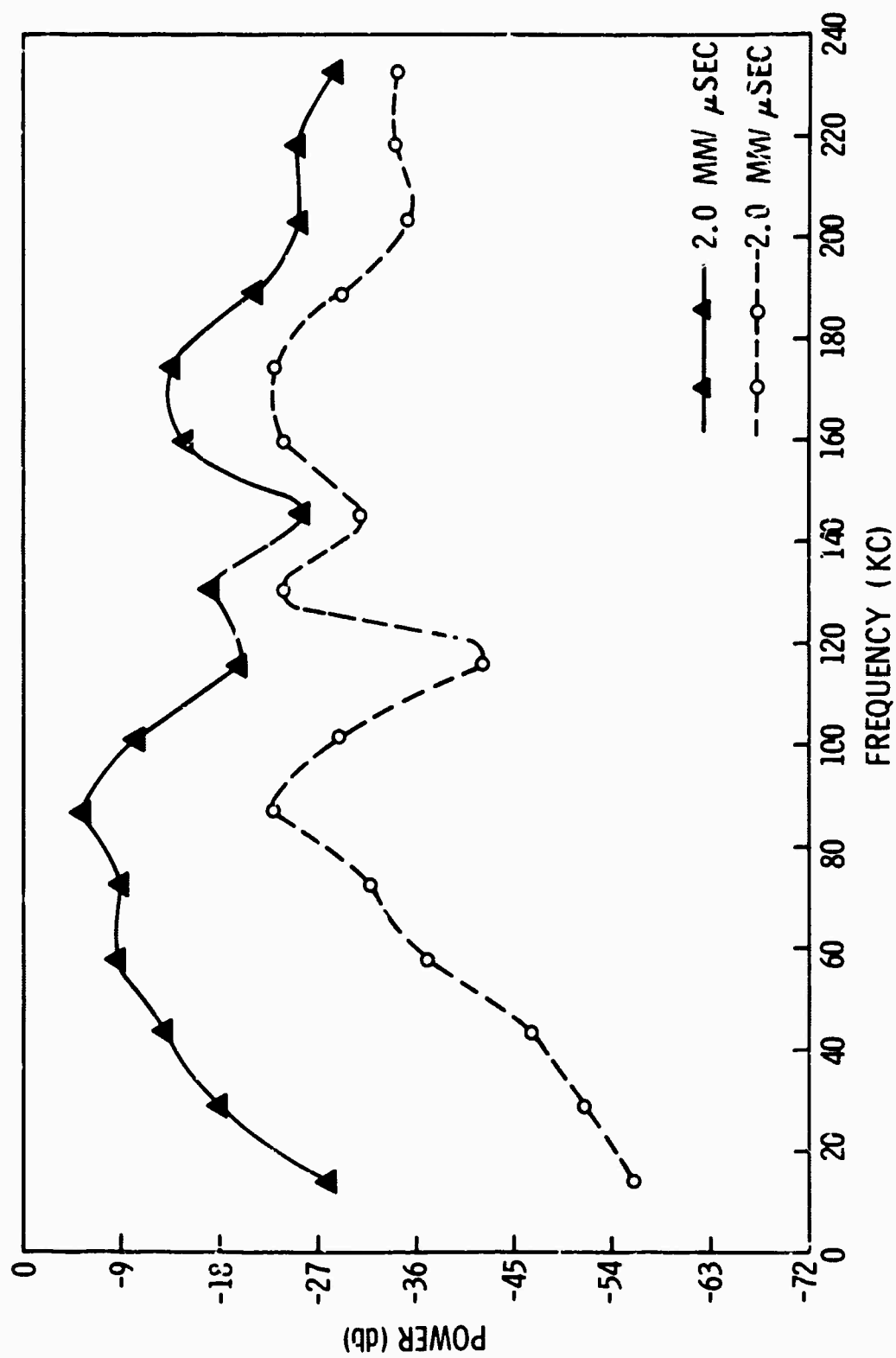
Figure III-18. Relative Vertical Power Spectra of Incident Rayleigh Mode and Backscattered Energy at 24.5 cm from Source Using Scatterer 2

science services division
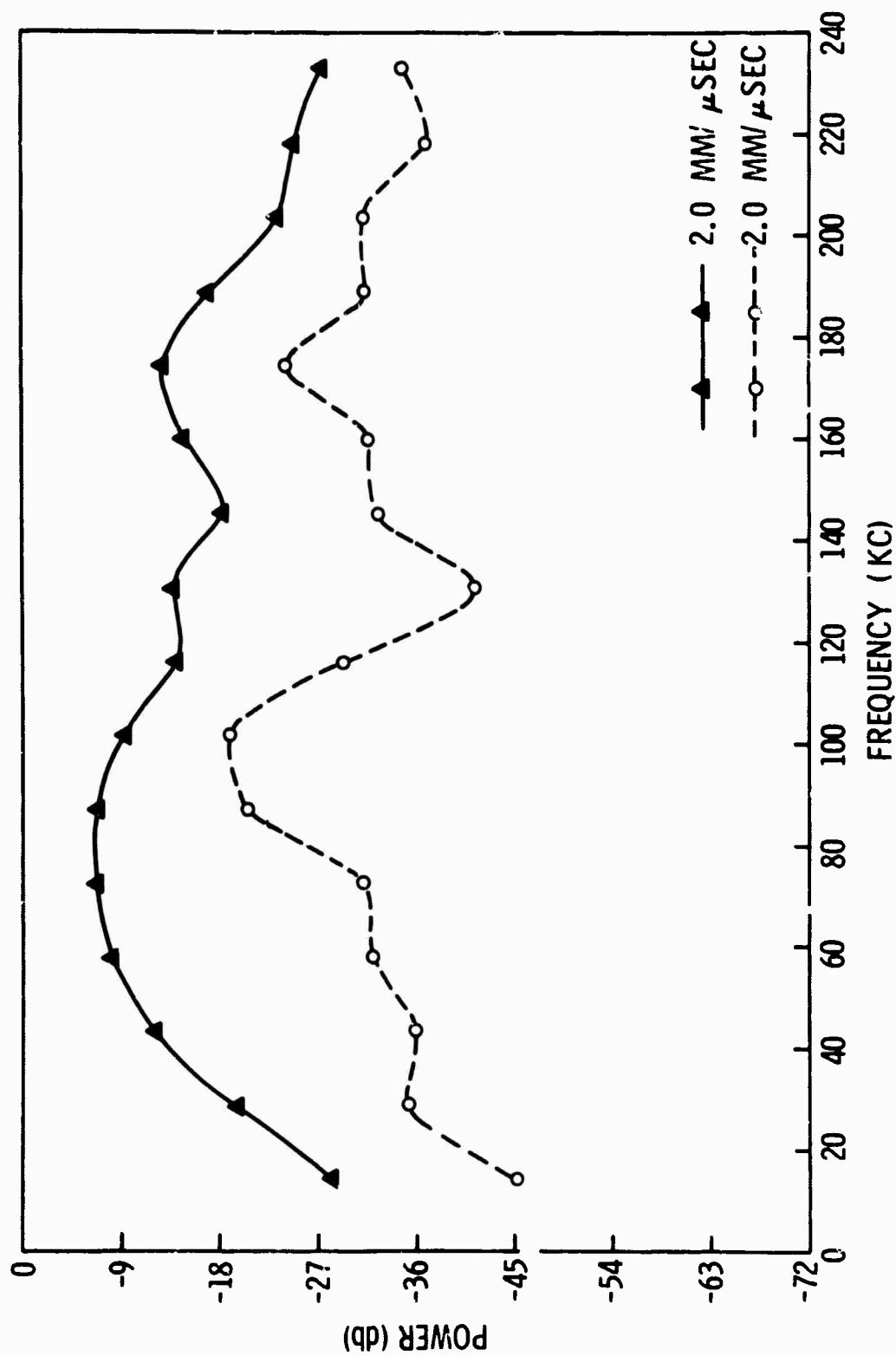
Figure III-19. Relative Vertical Power Spectra of Incident Rayleigh Mode and Backscattered Energy at 33.5 cm from Source Using Scatterer 2

science services division
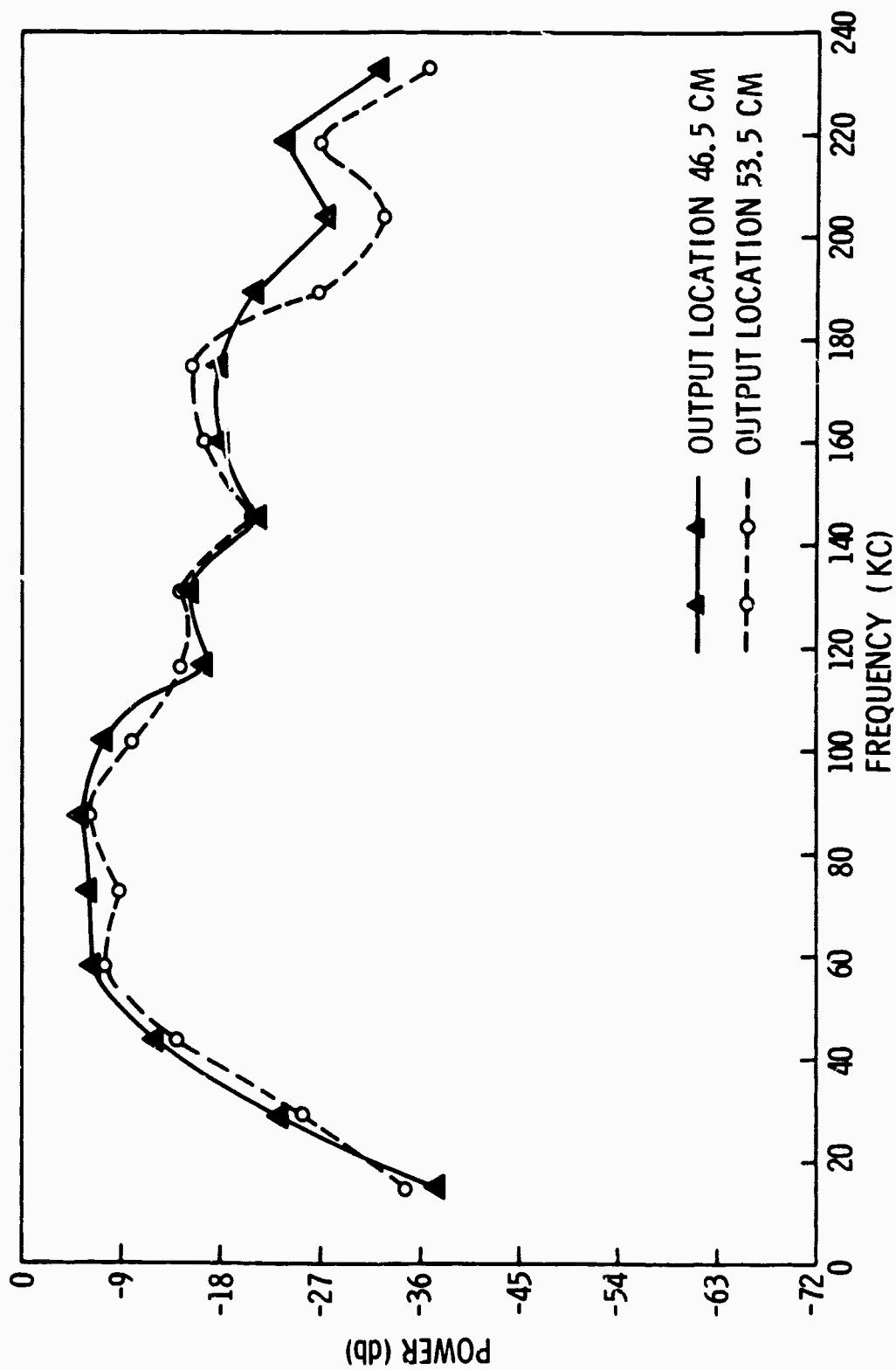
Figure III-20. Relative Vertical Power Spectra of Incident Rayleigh Mode at 46.5 and 53.5 cm from Source Using Scatterer 1
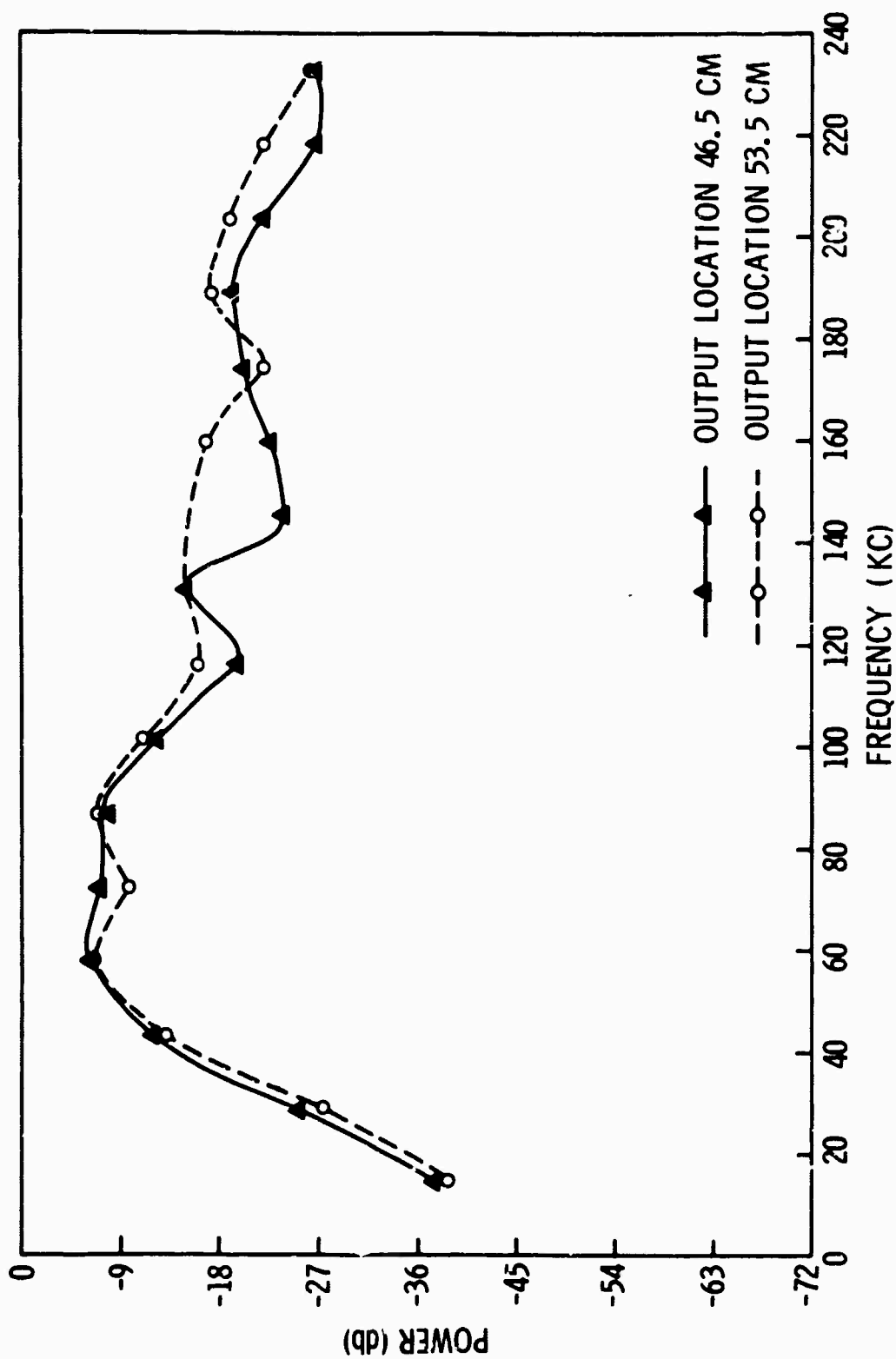
Figure III-21. Relative Vertical Power Spectra of Incident Rayleigh Mode at 46.5 and 53.5 cm from Source Using Scatterer 2

Transfer functions (Figures III-22 and III-23) which change the incident Rayleigh energy into the velocity-filtered backscattered energy were computed for both scatterers at output distances of 15.5, 24.5, and 33.5 cm. Since the calculations were performed for more points in the frequency domain, these results are refinements of those previously reported.

The 17-pt transfer functions were calculated at a 14.69-kc Δf from that part of the time trace within the 69-μsec gate shown in Figures III-10 through III-13. Plots of these transfer functions in db are shown in Figures III-24 and III-25 for scatterers 1 and 2. It is seen by comparisons with Figures III-14 through III-19 that these transfer functions carry the incident power spectra into the backscattered power spectra.

The power spectra curves exhibit both structure and variability. To better understand the effects of the scatterers, the transfer functions must be referenced continuously to these power spectra. For example, the power level of the incident Rayleigh wave exhibits a sharp decrease at 125 to 150 kc, which might account for the relatively large fluctuations in the transfer-function curves at these frequencies. This decrease suggests that should the incident and backscattered Rayleigh energy be whitened and the the transfer functions computed, undesired power-level fluctuations would be eliminated.

In addition to influencing the shape of the source power spectr m, the transfer functions exhibit a consistent frequency dependence. Frequency dependence may be divided approximately into low- (0 to 80 kc), intermediate- (80 to 170 kc), and high-frequency (more than 170 kc) regimes.

Energy in the low-frequency regime falls principally between 40 and 80 kc. For these frequencies, the amplitudes of the transfer functions (Figures III-22 and III-23) are small, indicating that long wavelengths do not interact with the scatterer. This behavior is seen more clearly by comparing the amplitudes in the low-frequency regime with those in the high-frequency regime. Such a comparison shows that the short-wavelengths in the high-frequency regime are interacting most effectively with the scatterer.

science services division
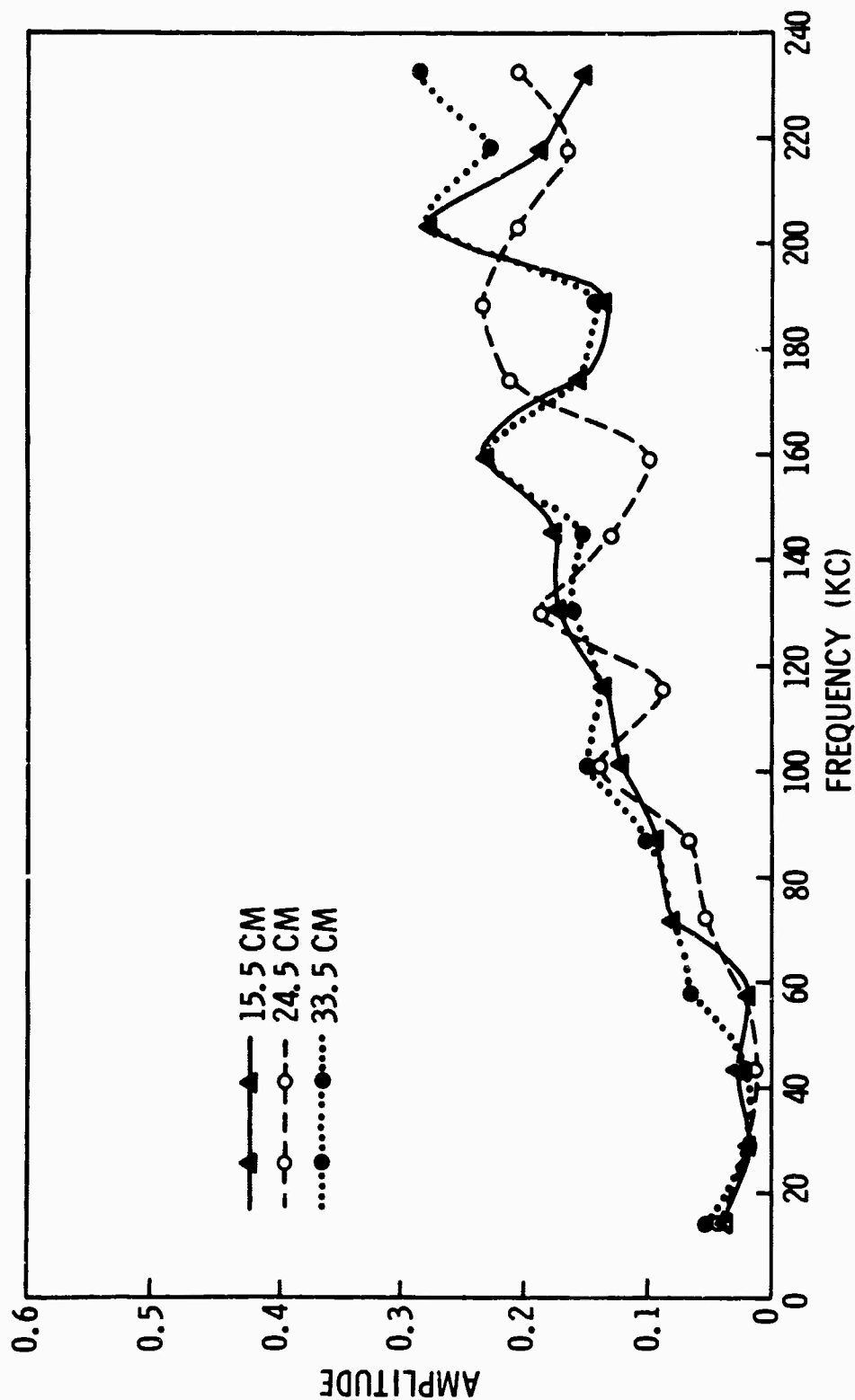
Figure III-22. Amplitude of Transfer Function for Scatterer 1 at 15.5, 24.5, and 33.5 cm

science services division
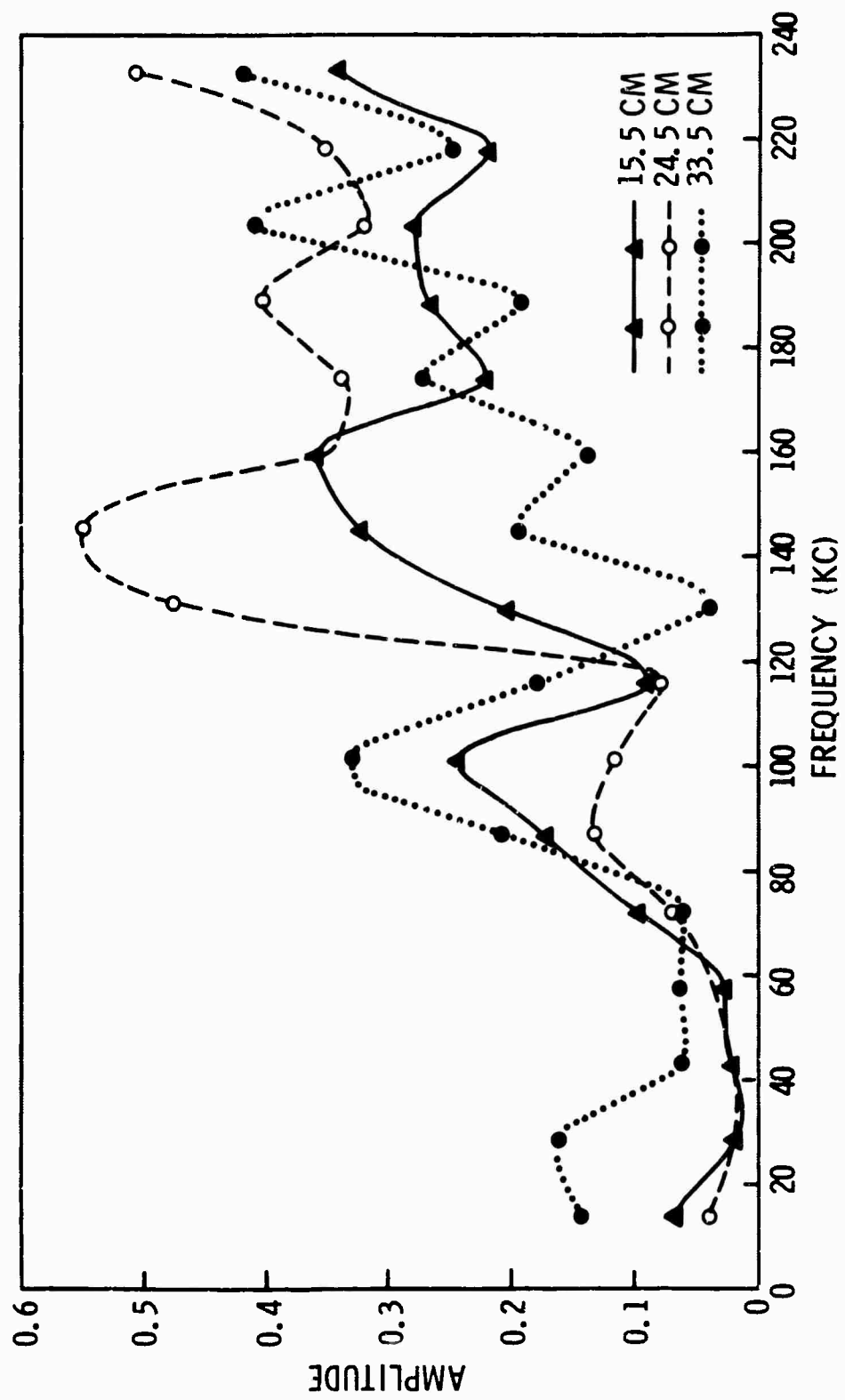
Figure III-23. Amplitude of Transfer Function for Scatterer 2 at 15.5, 24.5, and 33.5 cm
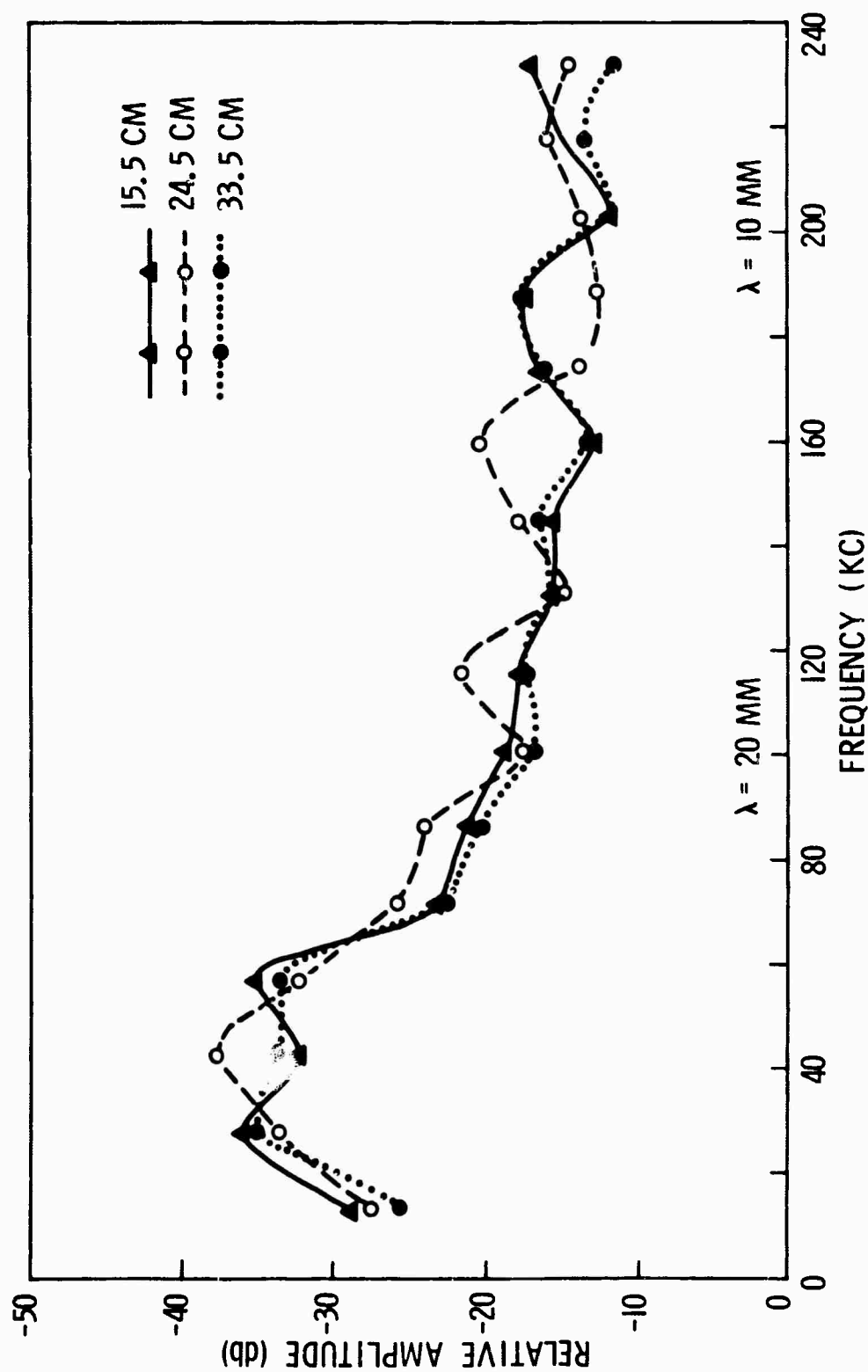
Figure III-24. Transfer Function in db for Scatterer 1 at 15.5, 24.5, and 33.5 cm

science services division
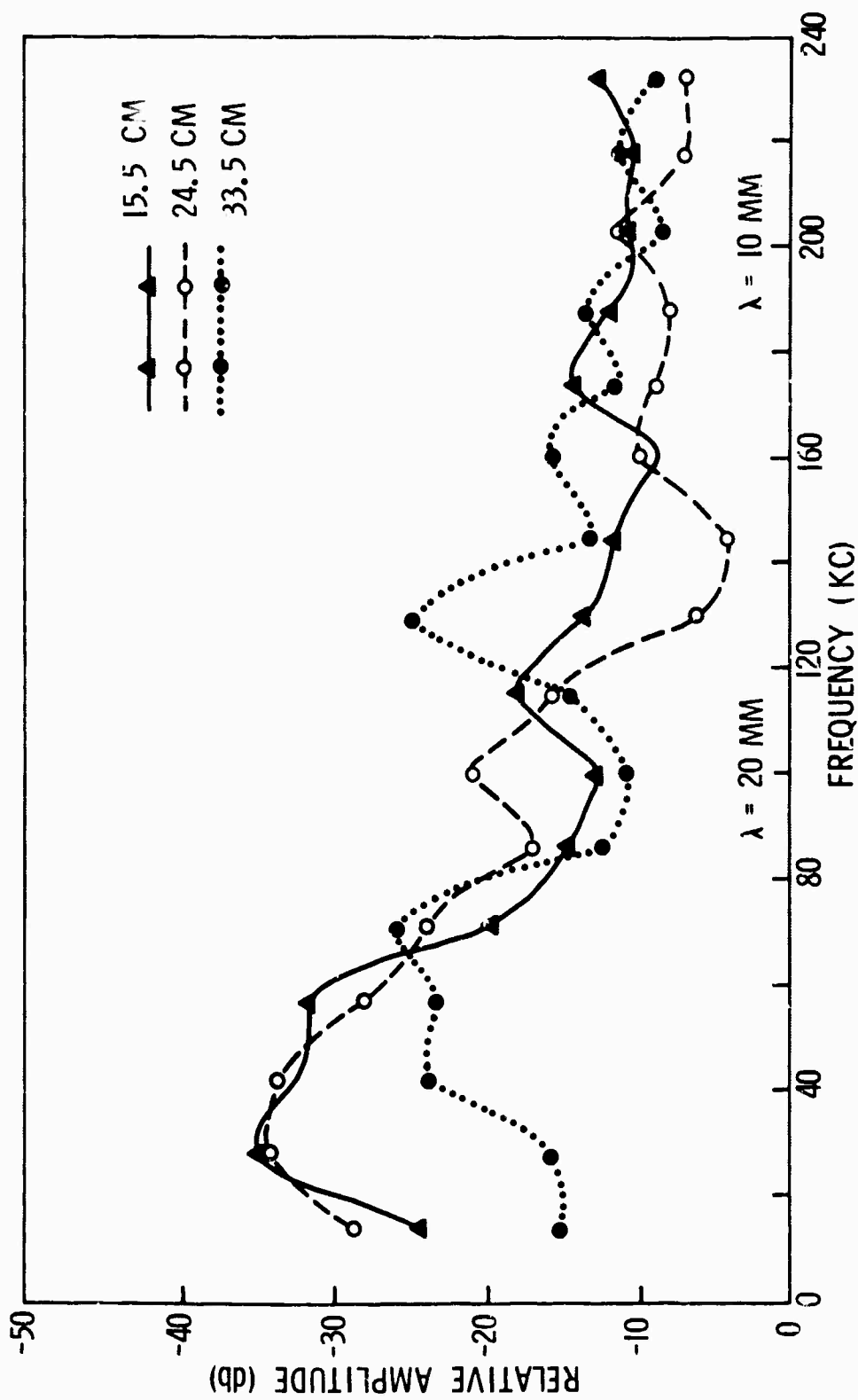
Figure III-25. Transfer Function in db for Scatterer 2 at 15.5, 24.5, and 33.5 cm

The character of the transfer function at intermediate frequencies is relatively more complicated than at other frequencies. Although this is partially due to the complicated source spectrum between 100 and 160 kc, it could also be a consequence of the greater sensitivity of the scattering interaction to wavelengths of the same order of magnitude as the scatterer. Physical consideration indicates the scattering interaction is most difficult to describe for wavelengths two to four times the dimension of the scatterer. A frequency of 100 kc corresponds to a wavelength of 20 mm, twice the base length of the scatterer.

Good agreement exists between the transfer functions computed at different output distances. Better agreement is displayed for scatterer 1 than for scatterer 2. For scatterer 1, the agreement is excellent between the 15.5- and 33.5-cm output distances.

Differences in the transfer functions at the three output locations may be attributed partially to crystal-coupling and gain-equalization problems. A small amplitude trace causes variations in output from the wideband velocity filtering process, which partially accounts for differences in the transfer functions. An example of this is shown in Figure III-9, where the recording for the 23-cm output distance displays considerably lower amplitude than adjacent recordings.

In an attempt to assess quantitatively the effect of the scatterer upon the phase spectrum of the incident energy, the phase of the transfer function was calculated. The phase shift was found to approximate closely a linear function of the frequency. It was impossible to determine precisely the phase shifts introduced by the scattering interaction from this analysis.

In conclusion, the only observed scattered energy was backscattered Rayleigh energy. No conversion of Rayleigh energy into P- or S-wave energy was observed. The observation of backscattered Rayleigh

science services division

energy is in agreement with Hudson and Knopoff.[7] Results of the experiment
indicate that the shape of the scatterer critically affects the backscattering
efficiency. as suggested by the noticeable difference between the two scat-
terers. There was no apparent change in the transmitted Rayleigh wave as
it propagated the scatterers.

It is desirable to have values computed using the Pie Slice
process at more output locations. Perhaps more significance could be
attached to the transfer functions if this information were available.

D. EFFECTS OF LATERAL INHOMOGENEITY ON AN UPCOMING P WAVE

This study's purpose was to determine the effect of a lateral
inhomogeneity on an upcoming plane P wave. Model H-6 was used to per-
form the studies (Figure III-1). A plane-wave source was approximated by
gluing the source transducer to the bottom of the model directly below the
center of the lateral thickness change. A suite of vertical and horizontal
traces then were digitized at 1-cm spacing across the top of the model from
-20 cm to +20 cm. Zero horizontal distance is the point on the surface
vertically above the source, and the distances given are the horizontal dis-
tances from the zero location. Negative numbers indicate distances mea-
sured from the zero point toward the thin end, while positive numbers are
measured toward the thick end. These vertical and horizontal seismograms
are presented in Figures III-26 and III-27, respectively.

Theoretical travel-time curves which were computed for
several of the expected arrivals are shown in Figure III-28, which overlays
both the vertical and horizontal recordings. Figure III-29 identifies the ray
paths for the theoretical curves. Curve A is the direct P wave from the
source; curve B is the direct S wave from the source; curves C and D are
expected arrival times when the corners on the thin and thick ends act as
point sources. These events follow the direct P wave so closely that the only
evidence of them is a distortion in the waveform of the direct P wave.

science services division
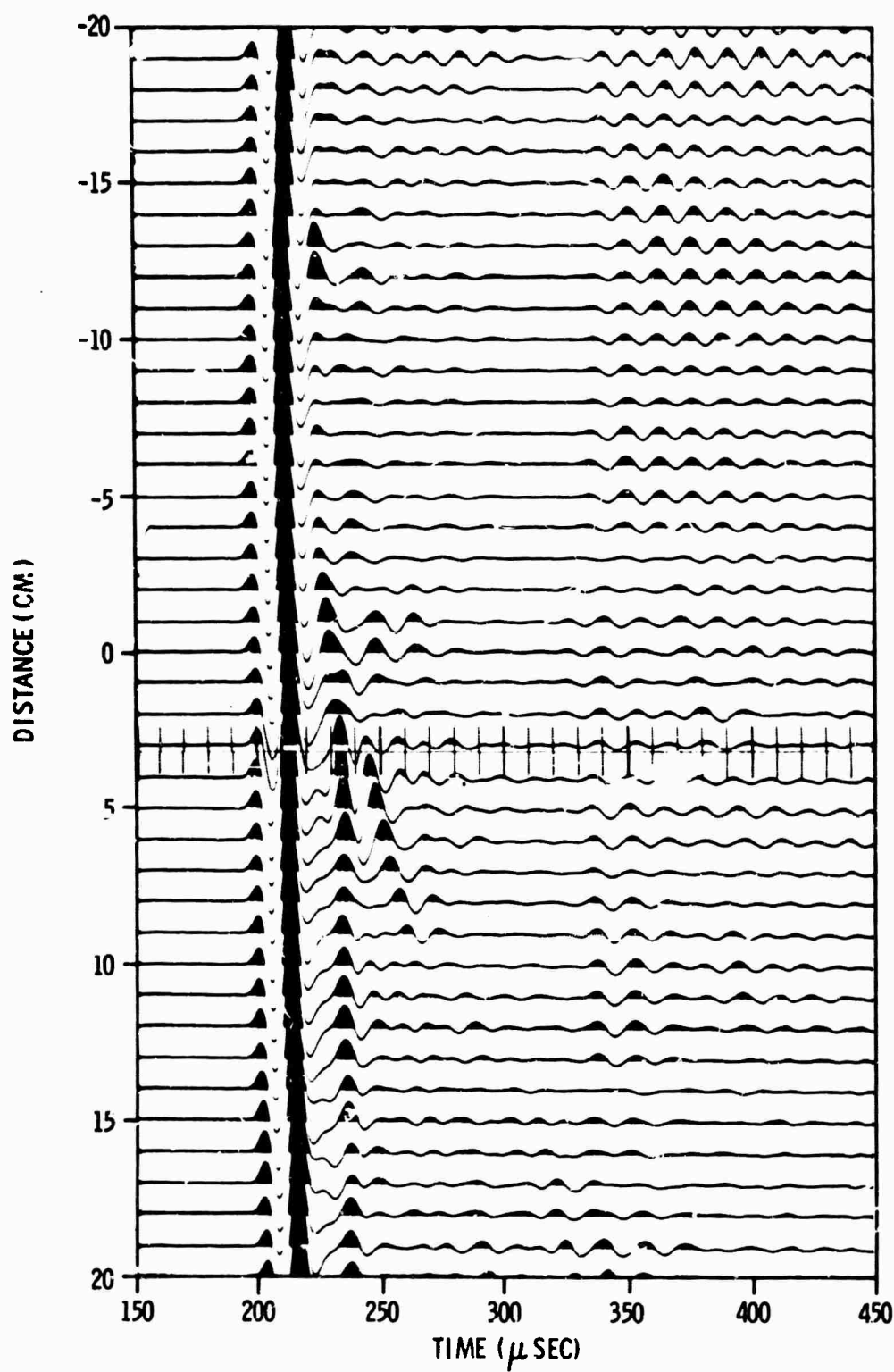
Figure III-26. Vertical Recordings Obtained from Model H-6 with the Source Located on the Bottom of the Model (Horizontal distance range -20 to +20 cm)

THIN END

THICK END

-3

DIP

+3

CURVE A
CURVE B
CURVE C
CURVE D
CURVE E
CURVE F
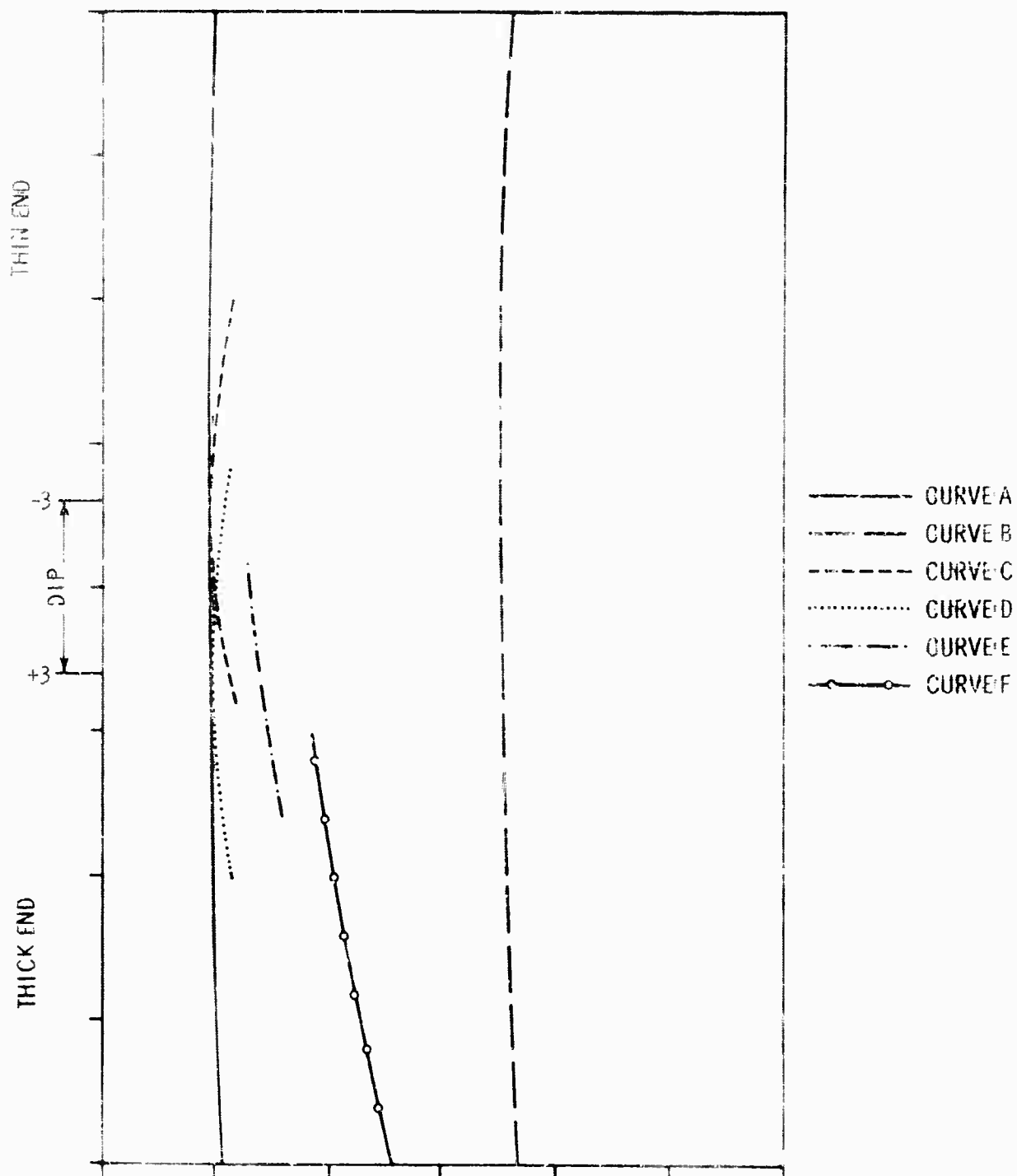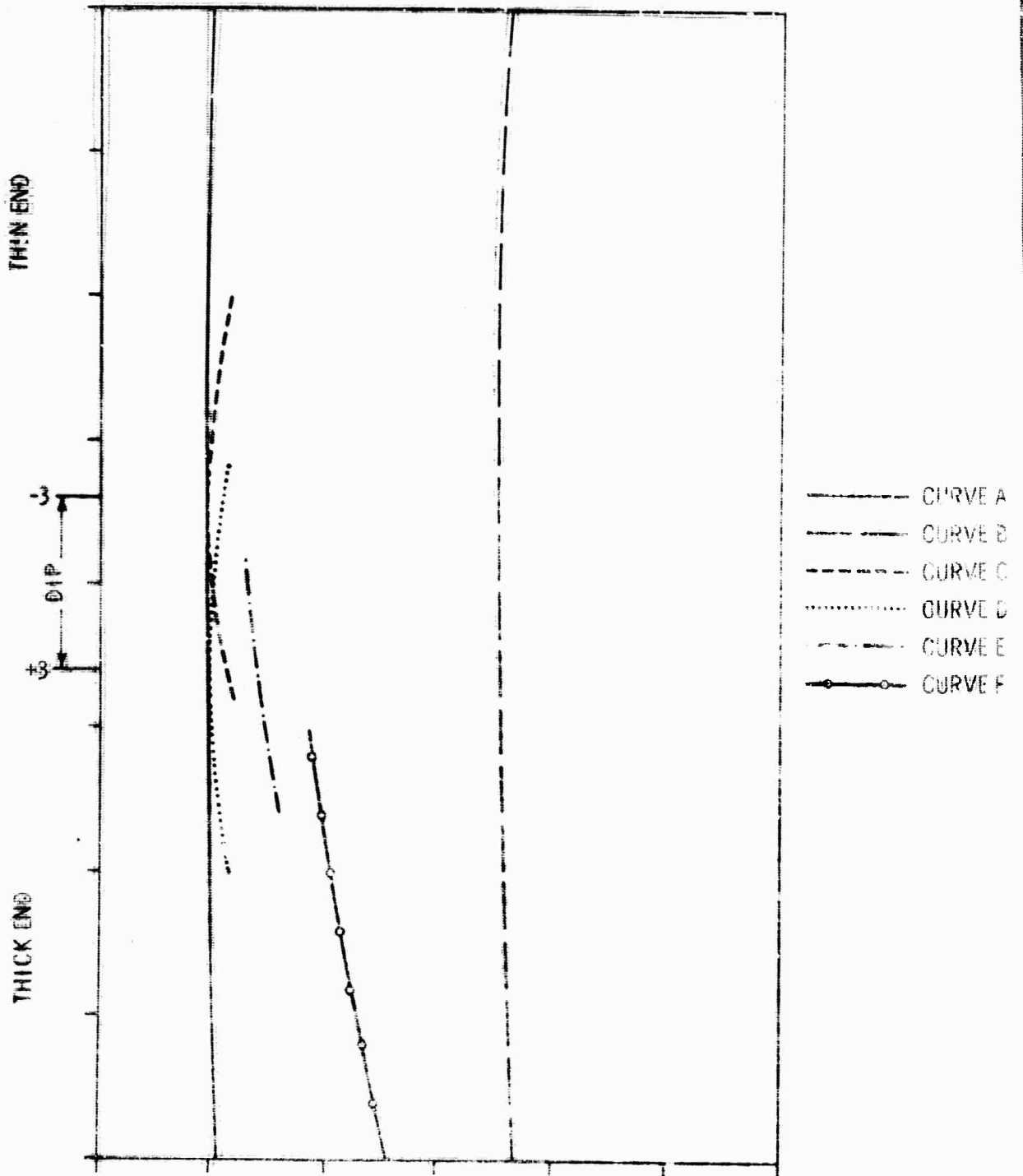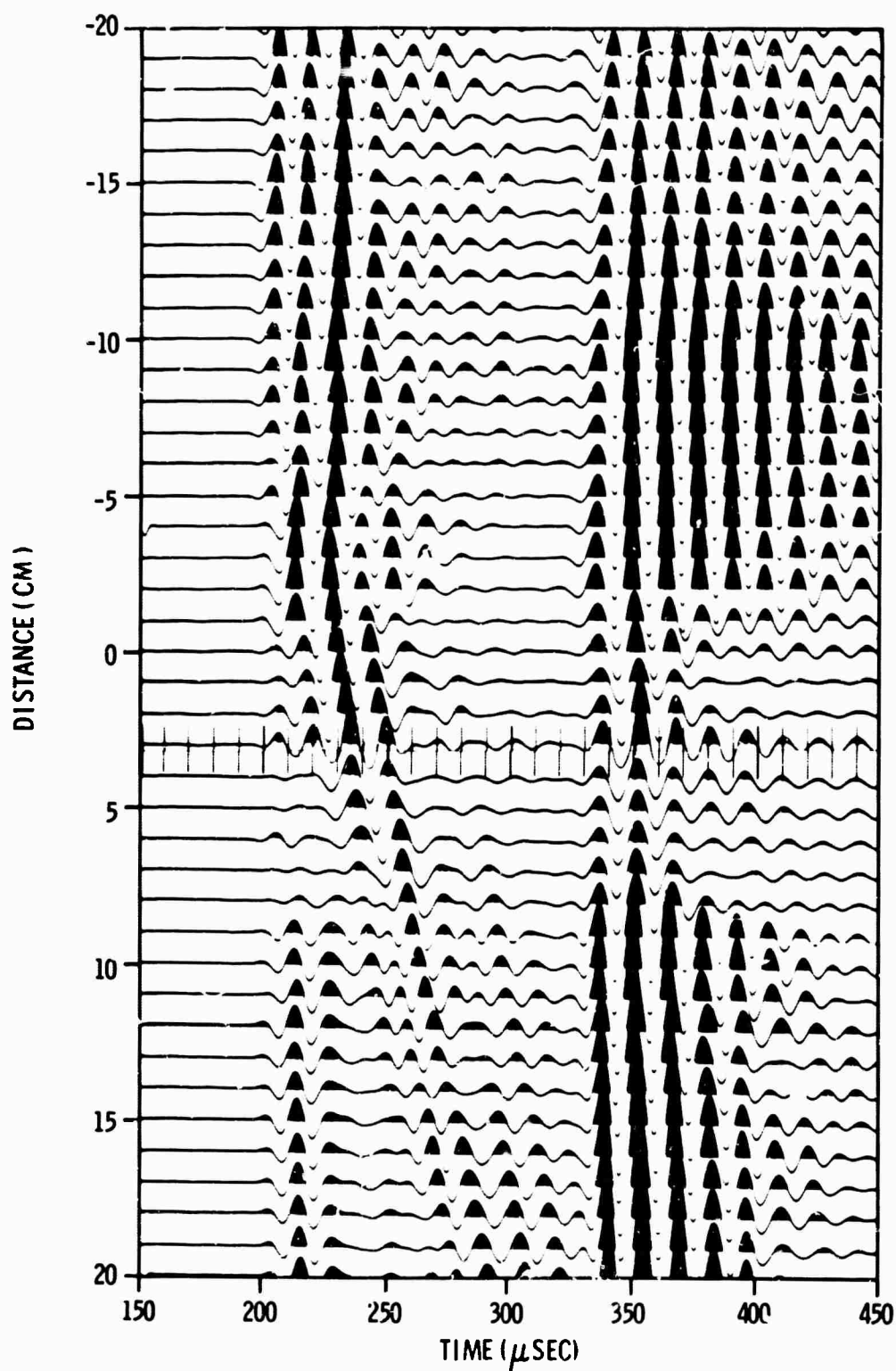
Figure III-27. Horizontal Recordings Obtained from Model H-6 with the Source Located on the Bottom of the Model (Horizontal distance range -20 to +20 cm)

science services divis' n
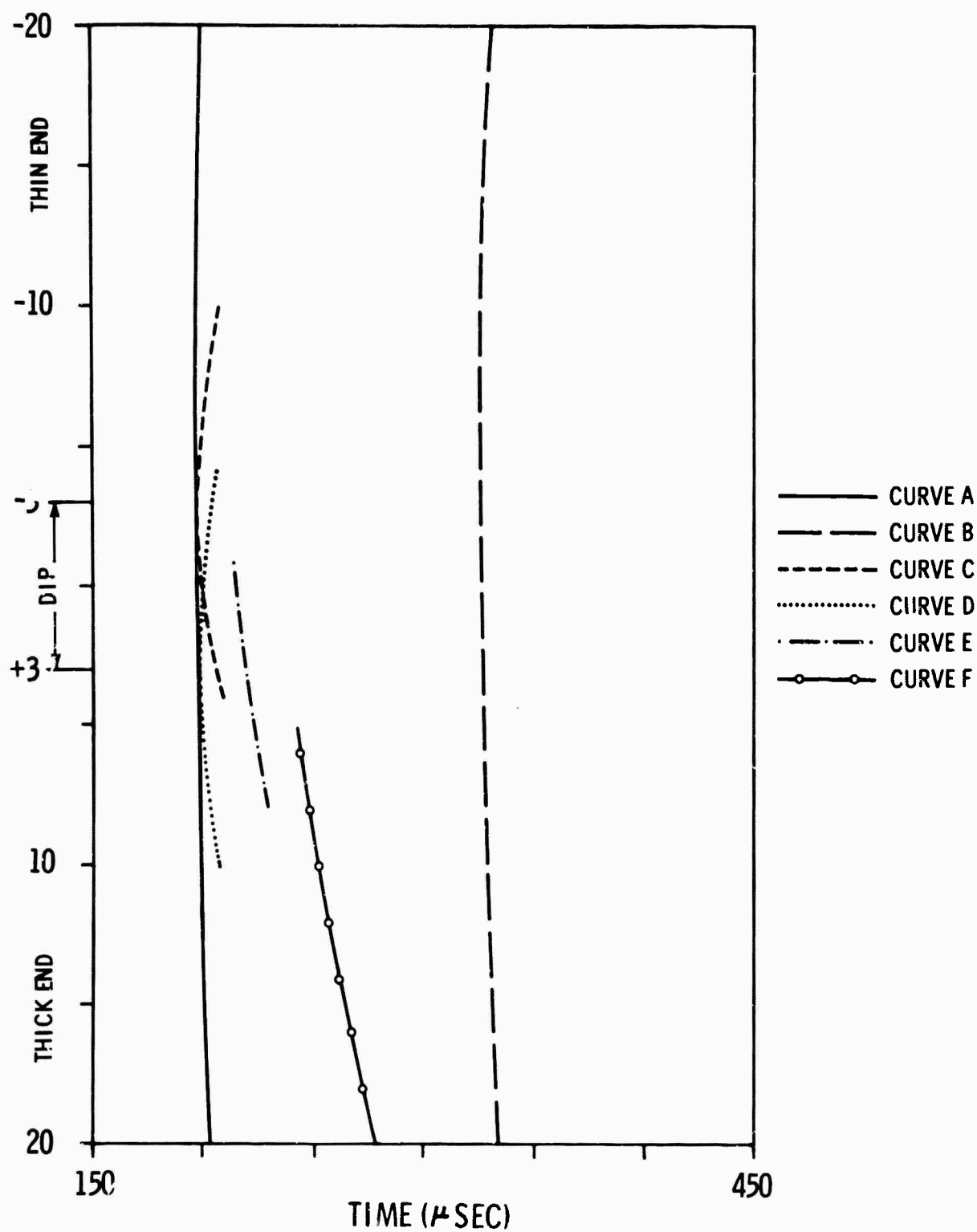
Figure III-28. Theoretical Travel-Time Curves for Model H-6 with the
Source Located on the Bottom of the Model

science services division
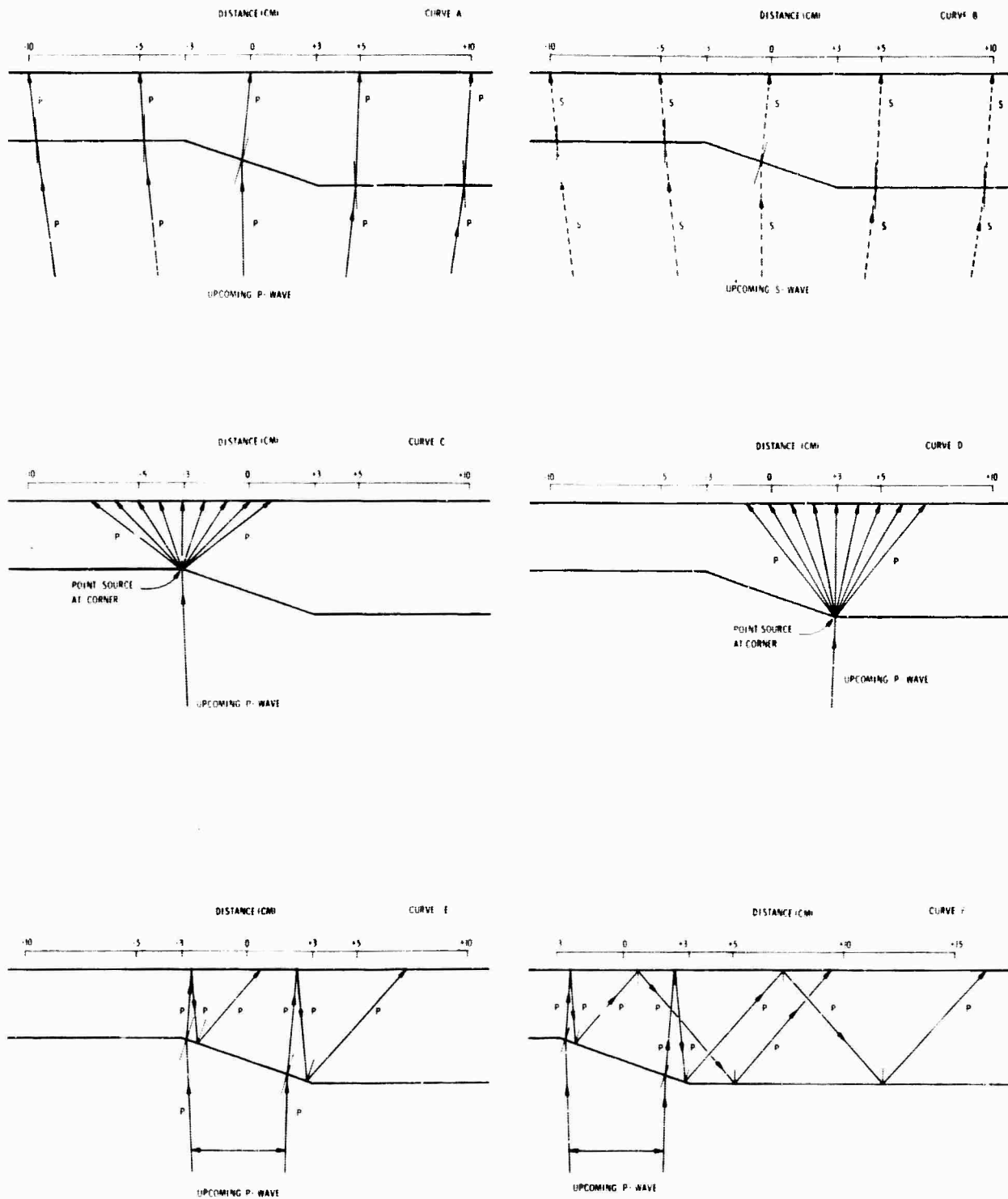
Figure III-29. Ray Paths for the Six Theoretical Travel-Time Curves Shown in Figure III-28

Curve E results when the P wave, refracted through the dipping segment of the layer, reflects downward from the surface and is reflected upward again by the dipping segment. Direct P energy reflected from the surface on each side of this dipping segment (from -20 to -3 cm and +3 to +20 cm) is largely transmitted back into the half-space, since the reflection coefficient is low for the small angle of incidence. However, the direct P energy refracted through the dipping segment and reflected downward from the surface back onto the dipping segment has a larger angle of incidence and hence a larger reflection coefficient. One effect of the dipping segment then is to cause a significant amount of energy to propagate into the thick end at a relatively low phase velocity.

Curve F results from adding one additional P bounce in the thick end to curve E.

P and S conversions occur at each reflection point, giving additional propagation paths which result in complex interference patterns at the surface. The observed vertical component of the direct P wave (Figure III-26) agrees well with ray theory (curve A, Figure III-28). There is good agreement between theory and measurement for the horizontal component of the direct P wave (Figure III-27) for traces recorded outside the influence of the dipping segment (-5 to -20 cm and +9 to +20 cm). Note that the P wave reverses polarity from the thin end to the thick end (Figure III-27). This is consistent with the geometric resolution of the P-wave's horizontal component. The horizontal P-wave component shows considerable distortion between -4 and +3 cm, and a large drop in amplitude is apparent between +4 and +8 cm. This i. attributed to constructive and destructive interference associated with P and S events propagating from the corners of the dipping segment (curves C and D).

Immediately following the direct P wave and preceding the direct S wave, relatively large amplitude sinusoidal waves which last for several cycles are seen on the thin end (Figure III-27). These are S waves generated from the incident P wave (P to S conversion) and associated with reverberation in the plane layer.

The direct S wave is best observed in Figure III-27 (curve B). Photographs of the S wave taken in the half-space show that the source-generated S wave has a maximum in amplitude to the left and right of the source with a null vertically above the source and that the wave changes polarity across this null. The direct S wave observed on the records does not appear to change polarity from the thin end to the thick end; that is, a given peak or trough may be traced completely across the record with no apparent polarity change. In this case, however, the observed travel time does not agree with the theoretical travel time. This is consistent with the known source-radiation pattern, since a given peak on the thin end must go into a trough on the thick end.

The theoretically predicted focusing of energy by the dipping segment into the thick end may be observed on the records (curves E and F). This energy decays with distance, since the reflection angles for these rays (Figure III-29) are less than the angle for critical P refraction along the layer interface. Agreement with these theoretical travel-time curves is fair. The changes in wave shape probably result from waveform interference due to P and S conversions at the reflecting points which yield additional curves that have the same general trend as curves E and F.

E. CRUSTAL REVERBERATION

Theoretical surface displacements caused by a plane P-wave teleseism emerging from the mantle half-space of a one-layer crust were computed for two mathematical models defined in Table III-1. The layer and half-space of the models are allowed infinite lateral (horizontal) dimensions.

Table III-1

ELASTIC PARAMETERS OF MODEL H-6

Layer	Compressional Velocity, α (mm/μsec)	Shear Velocity, β (mm/μsec)	Density (gm/cm^3)	Thickness (mm)
1 (Brass)	3.91	2.09	1.0	30
Half-space (Steel)	5.24	3.10	1.0	∞
1	3.91	2.09	1.0	50
Half-space	5.24	3.10	1.0	∞

Four phase velocities were considered for both models: 25.10 mm/μsec, 33.15 mm/μsec, 49.39 mm/μsec, and 98.38 mm/μsec. The physical parameters and the phase velocities were selected to correspond to portions of the two-dimensional analog model of the earth's crust — model H-6.

A piezoelectric source transducer was placed directly below the lateral discontinuity in the brass crustal layer (Figure III-1). This structure consists of a dipping interface 60-mm long, connecting a 30-mm crust to a 50-mm crust. The slope of the dipping crustal interface (which represents the moho) is approximately 19°, an upper limit for most real earth crusts. In studying this model analytically, a number of crustal reverberation calculations for the plane-layer portions of its geometry were derived. A comparison of the experimental traces, recorded on either side

of the discontinuity, with theoretical predictions from the two mathematical models was attempted. It is assumed that the presence of the dipping interface is negligible at sufficiently great receiver distances.

Travel-time curves for the relevant rays of the experimental model are given in Figure III-30. Horizontal source-receiver separation, with the center of the discontinuity as axis origin, was chosen for the independent variable in this plot. Separations of 5 cm, 10 cm, 15 cm, and 20 cm correspond to phase velocities of 98.38 mm/μsec, 49.39 mm/μsec, 33.15 mm/μsec, and 25.1 mm/μsec. These curves are useful in identifying phases on the theoretical seismograms. For a phase velocity of 98.38 mm/μsec, the time differences between P and other phases are tabulated for both 30-mm and 50-mm crusts in Table III-2.

Horizontal- and vertical-amplitude spectra for displacement at the surface due to a plane-wave source are shown in Figure III-31. These amplitude spectra were Fourier transformed to obtain the sesimograms shown in Figures III-32 and III-33. The plane-wave source spectrum was white at the base of the crust, and the frequency calculations were carried out to 0.5 cycle/μsec with a Δf of 0.0133 cycle/μsec. This allows a time resolution of 1 μsec, the sample rate of the analog model data.

The 0.5 cycle/μsec ringing on the records is due to the mathematical truncation of the spectrum and can be neglected. The P, PPP, and PPPPP arrivals are indicated by arrows on the vertical traces. The horizontal seismograms are an order of magnitude below the vertical ones in amplitude and exhibit several more phases than the latter. The P, S, PPP, PPS, and SSS phases are evident, while a combination of PSS and PPPPP is present but difficult to resolve in time. Amplitude of the horizontal PPP suggests that PPPPP is very weak on the horizontal records. The vertical traces appear simpler than the horizontal ones because the P to S conversion efficiency yields S-phase amplitudes whose vertical components are much smaller than those of the P phases.
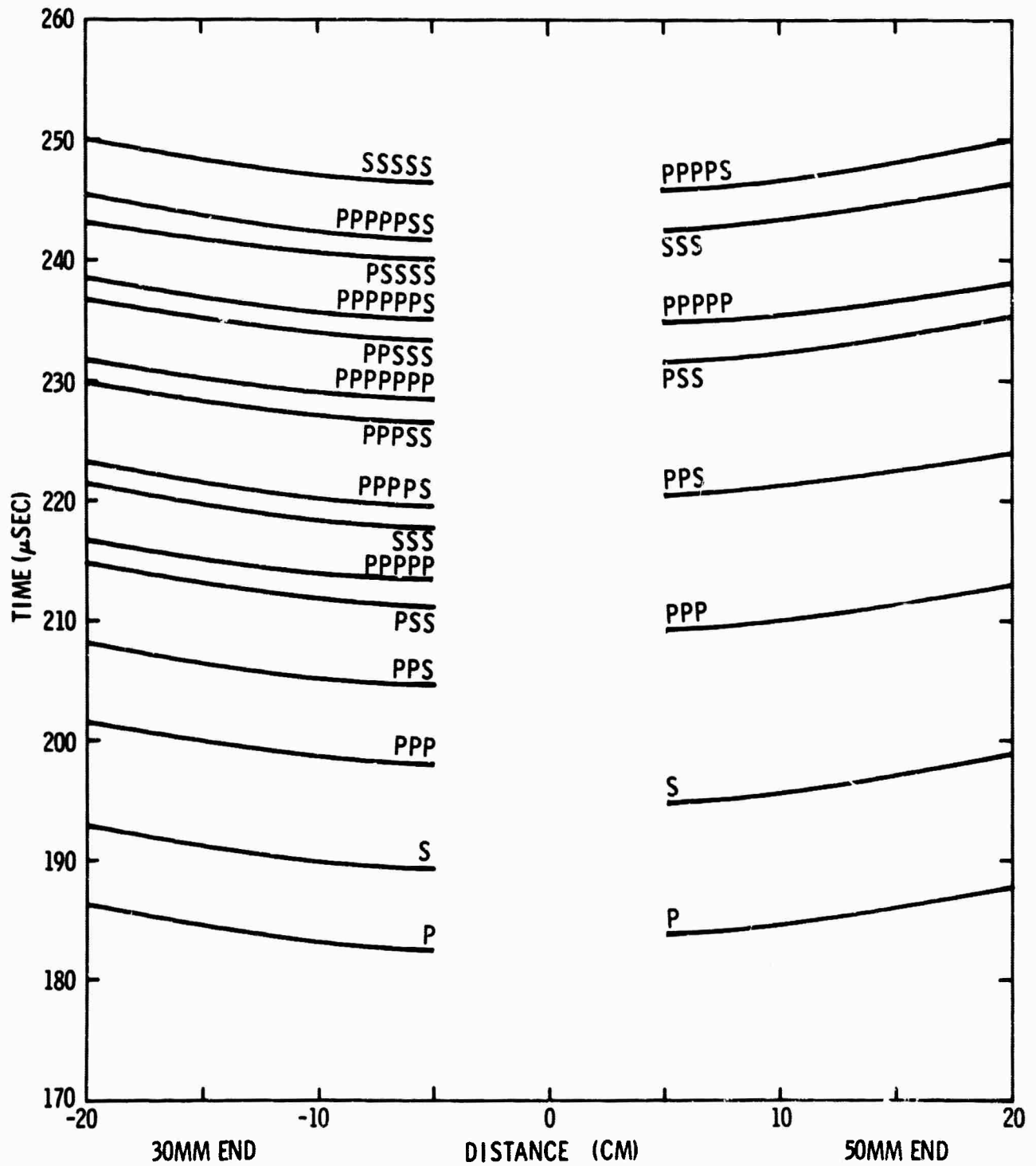
Figure III-30. Ray Theory Travel-Time Curves for Important Phases of the Two Crustal Models of Table III-1

Table III-2
TIME DIFFERENCES BETWEEN PHASES*

Phase	Travel-Time Relative to P Phase	
	30-mm Crust (μsec)	50-mm Crust (μsec)
S	6.5	11.0
P^3	15.5	25.0
P^2S	22.0	36.5
PS^2	28.5	47.5
P^5	31.0	50.5
S^3	35.0	58.5

*Phase velocity = 98.38 mm/μsec

On the other hand, the horizontal components of the P to S conversions do have amplitudes comparable with those of the S phases. The vertical amplitude spectra are correspondingly more simple than the horizontal amplitude spectra. Interference between the multiple phases PS^2 and P^3 in the horizontal seismograms makes their distinct identification as ray events difficult.

For the frequencies at which these calculations were performed, the plane wave may possess wavelengths ($\lambda = C/f$) of several hundred mm, much in excess of the layer thickness.

On the 30 mm and 50 mm vertical traces, the largest pulses are separated by 15 to 25 μsec, respectively. This corresponds to the reverberation time τ of the first P bounce, i.e., the two-way travel time of a compressional wave through the crust. τ dominates the structure of the vertical spectra, causing a periodic modulation approximately every $1/\tau$ cycle/μsec. Thus, the thin crust has a greater frequency separation between spectral peaks than does the thick cruse — in the ratio of 3:5, the layer thickness ratio.
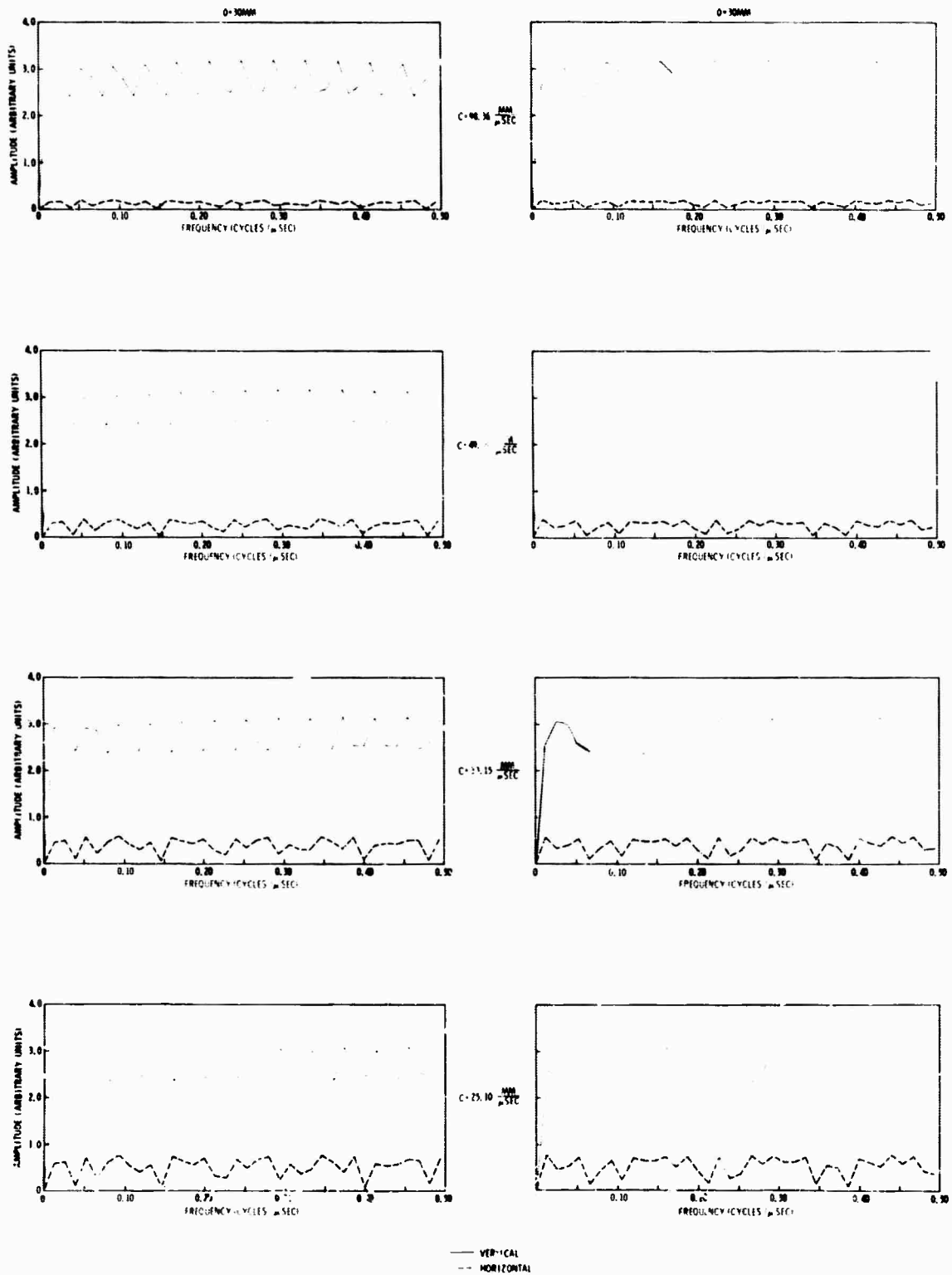
Figure III-31. Horizontal and Vertical Amplitude Spectra for Four Phase
Velocities Observed by a Surface Receiver on the 30-mm
and 50-mm Crustal Models of Table III-1

science services division
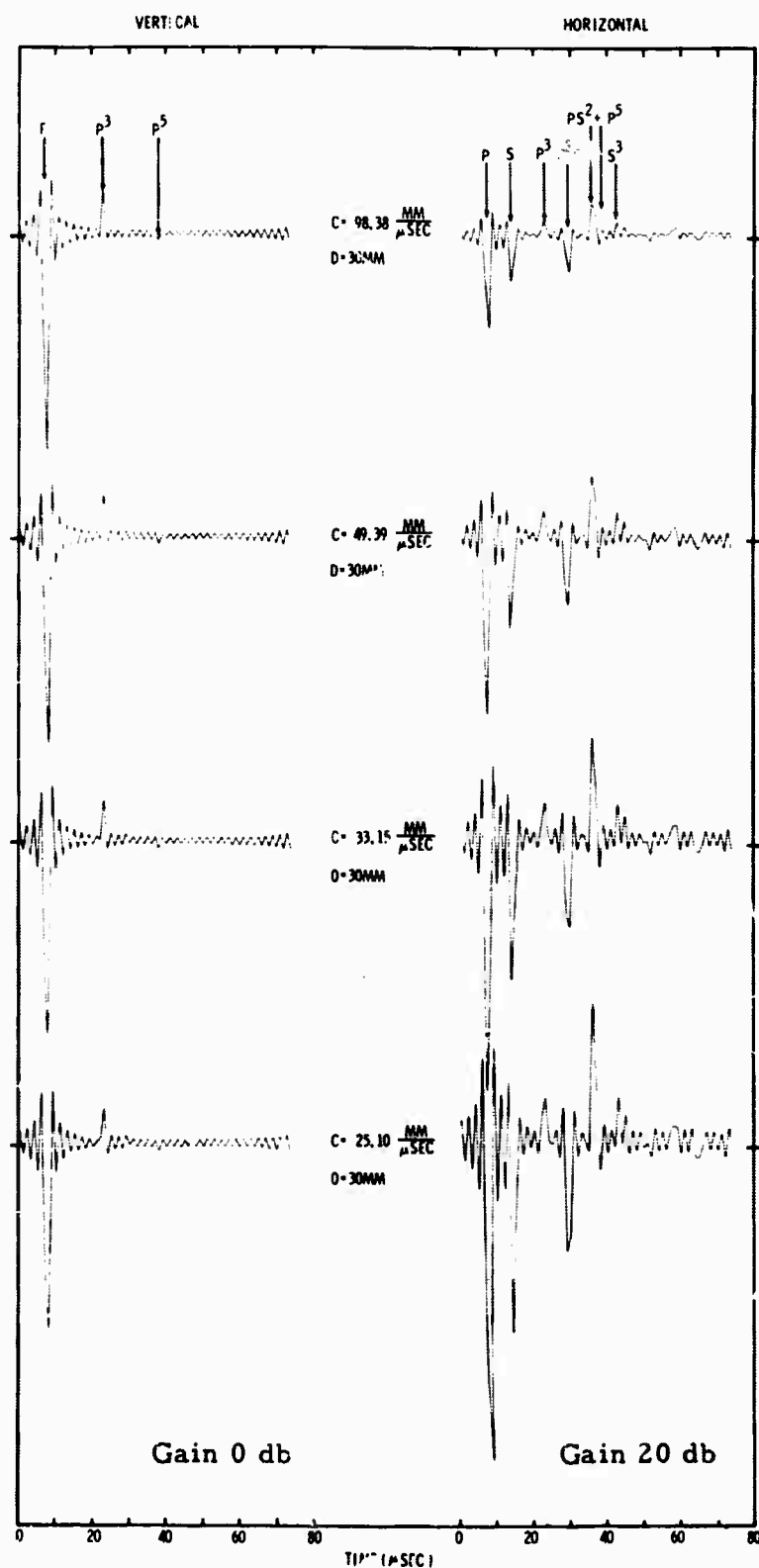
Figure III-32.   Theoretical Seismograms for Four Phase Velocities Observed by
a Surface Receiver on the 30-mm Crustal Model of Table III-1

science services division
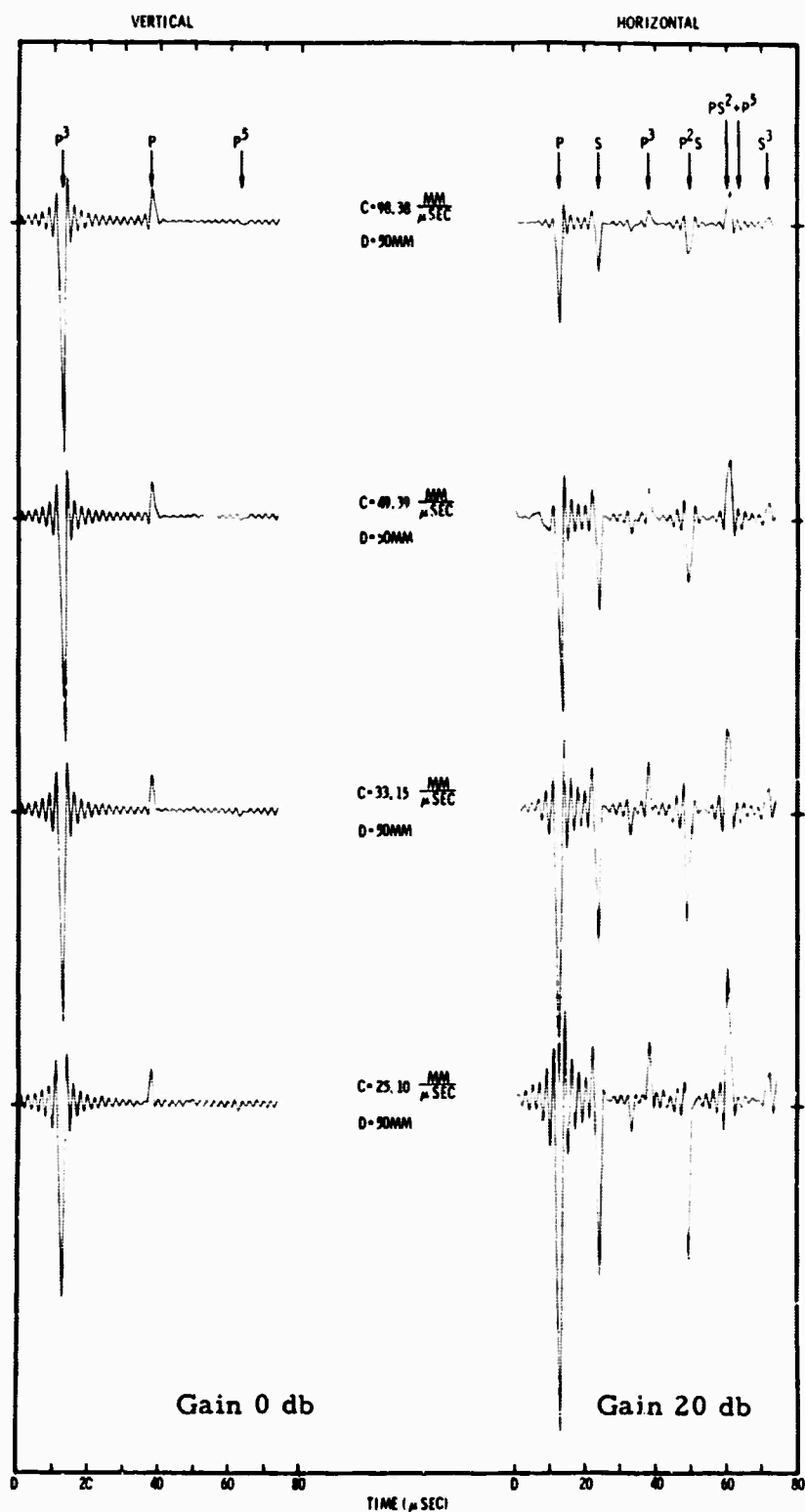
Figure III-33. Theoretical Seismograms for Four Phase Velocities Observed by a Surface Receiver on the 50-mm Crustal Model of Table III-1

Other significant time constants for the horizontal s smograms,
as shown by the travel-time differences of Table III-2, are 6.5 μsec for the
30-mm crust and 11.0 μsec for the 50-mm crust. These two times correspond
roughly to the difference between P and S, P^3 and P^2S, P^2S and PS^2, and PS^2 and S^3.
The complicated horizontal amplitud : spectra are consistent with interference
between these two modulating time constants. For the thin crust, the periodi-
city in the horizontal spectra are determined by both 1/15.5 and 1/6.5 cycle,,sec.

As expected, the spectral structure does not change very much
among the four phase velocities for a given crust, since the change in the
dominant multiple arrival times of either the 30-mm or 50-mm layer for the
phase velocities considered are on the order of 1 μsec and the associated
characteristic reverberation times are 15 and 25 μsec, respectively. This
implies an order of magnitude variation in spectrum modulation for the thick
crust of 8 percent (2/25 = 0.08) and results in a negligible frequency shift.

Agreement between the spectra of Figure III-31 and th. ex-
perimental spectra of Figure III-34 was inconclusive. There are several
possible reasons for this result. The spectral peaks of the laboratory data
are partially masked by the shape of the source spectrum, which makes a
determination of their frequency dependence imprecise.

Placement of the barium titanate receiver transducer may be
slightly in error. A 1-mm error is equivalent to a 1-km error in the real
earth. Also, the receiver passband does not have a fla'. response from 0 to
0.5 cycle/μsec, and the influence of the epoxy bond at the model interface
may be significant.

Amplitude spectra for a receiver 2 mm below the surface
were developed to determine quantitatively the alteration in spectral shape
with depth. The resulting horizontal and vertical spectra are presented in
Figure III-35. The modulation caused by the reverberation time constants
is still present in unchanged form. An additional, slower modulation of the
spectra is visible, corresponding to the time difference between the direct
and surface reflected ray, i.e., a ghost effect.

Figure III-34. Experimental and Black Theoretical Power Spectra Obtained from Time Traces at the -20 cm Location
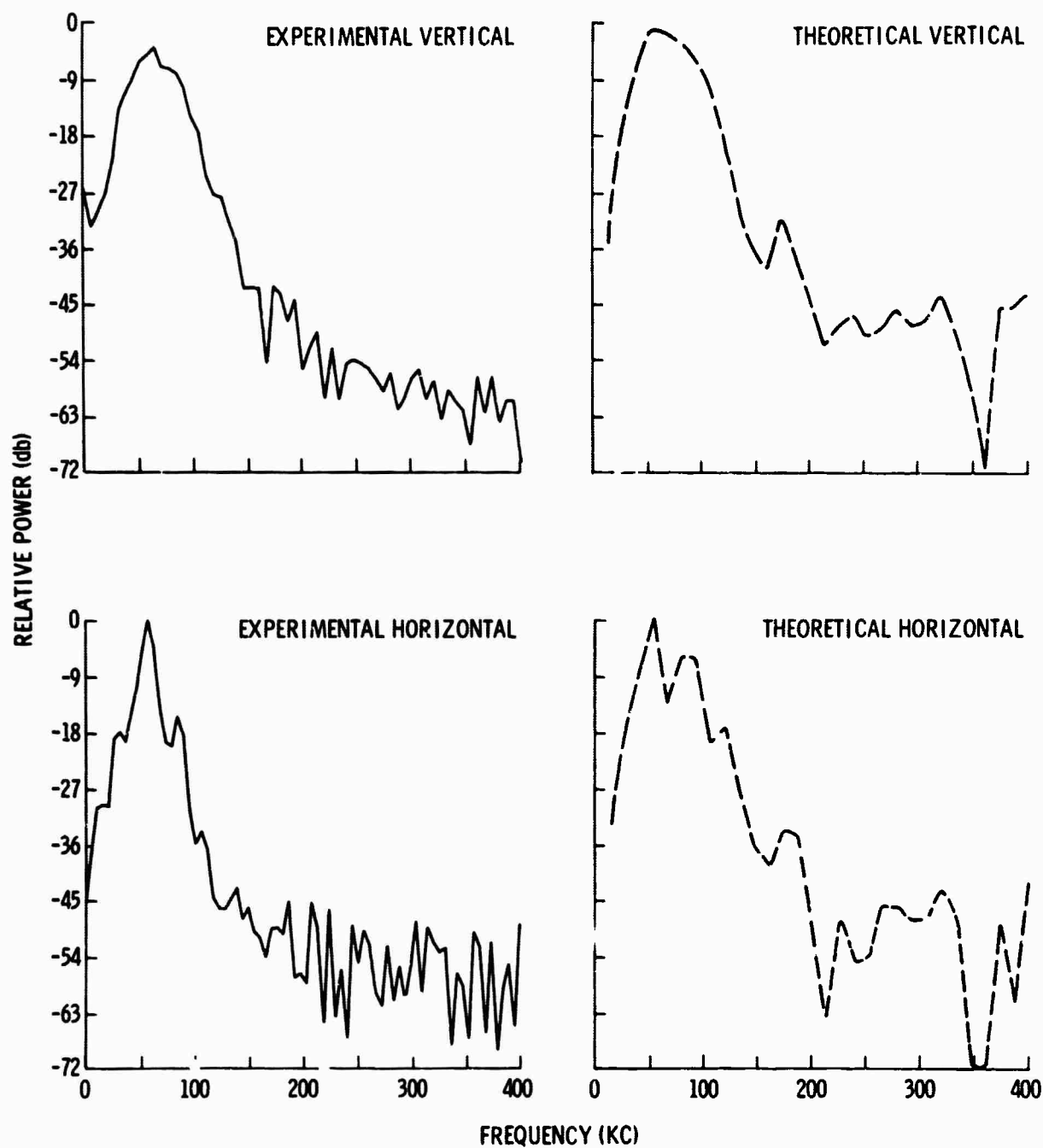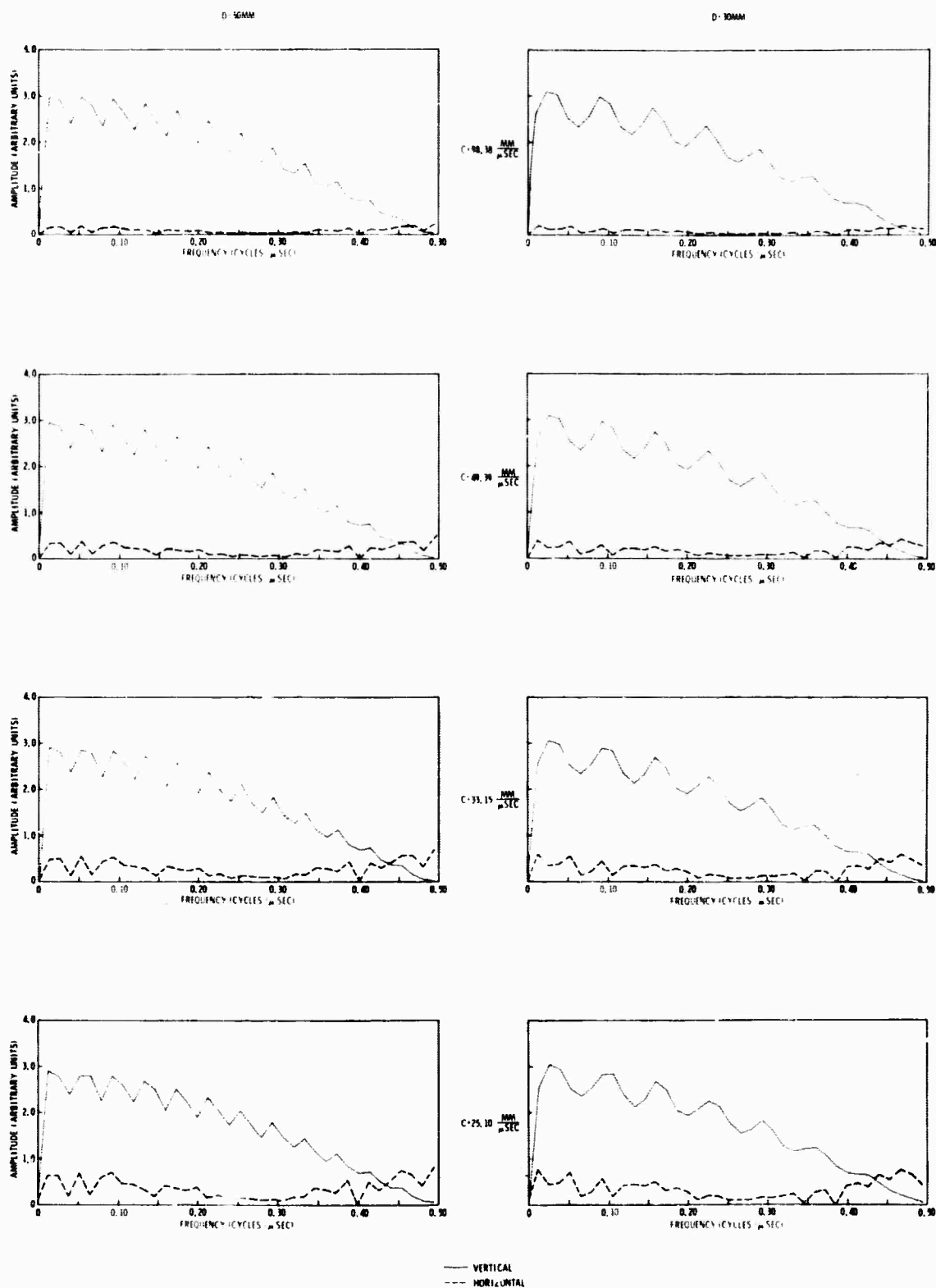
Figure III-35. Horizontal and Vertical Amplitude Spectra for Four Phase
Velocities Observed by a Receiver 2 km Below the Surface
of the 30-mm and 50-mm Crustal Models of Table III-1

science services division

Since the spectral peaks in the theoretical calculations are not shifted by a change in receiver depth, the placement of the receiver transducer on the analog model should not critically affect the spectral structure in the frequency band of interest. The experimental power is concentrated around 0.06 cycle/μsec, with three and possibly more small spectral peaks between 0.03 and 0.12 cycle/μsec.

For better comparison of the experimental and theoretical data, the latter were shaped by the digitized P pulse observed in the steel half-space of the analog model. The P pulse and its power spectrum are displayed in Figure III-36. The pulse length is approximately 75 μsec and has a dominant period of about 20 μsec. The resulting "black" theoretical power spectra are shown in Figure III-37. Again, the horizontal spectra possess much more structure than do the vertical spectra. They have three noticeable peaks comparable to some of the peaks in the experimental spectra in the frequency band where the power is concentrated. The peaks fall about 0.05, 0.08, and 0.12 cycle/μsec. Note that the presence of the lateral discontinuity makes a legitimate comparison of these spectra possible only at the lowest phase velocities. Moreover, the energy focused into the 50-mm layer by the dipping crustal segment may alter even the 25.1 mm/μsec spectrum.

The theoretical vertical spectra are notably smoother than the experimental spectra. The complexity of the theoretical and experimental horizontal spectra is comparable. Only for the thick crust do the blackened vertical spectra begin to show evidence of fine structure, and this part of the model data is unreliable. The P to S conversions, so prevalent in the horizontal theoretical predictions, are primarily responsible for any agreement between the calculations and the model. If the peaks in the experimental vertical results are also due to conversions, the implication is strong that the model P to S conversion is more potent than the theory is predicting.
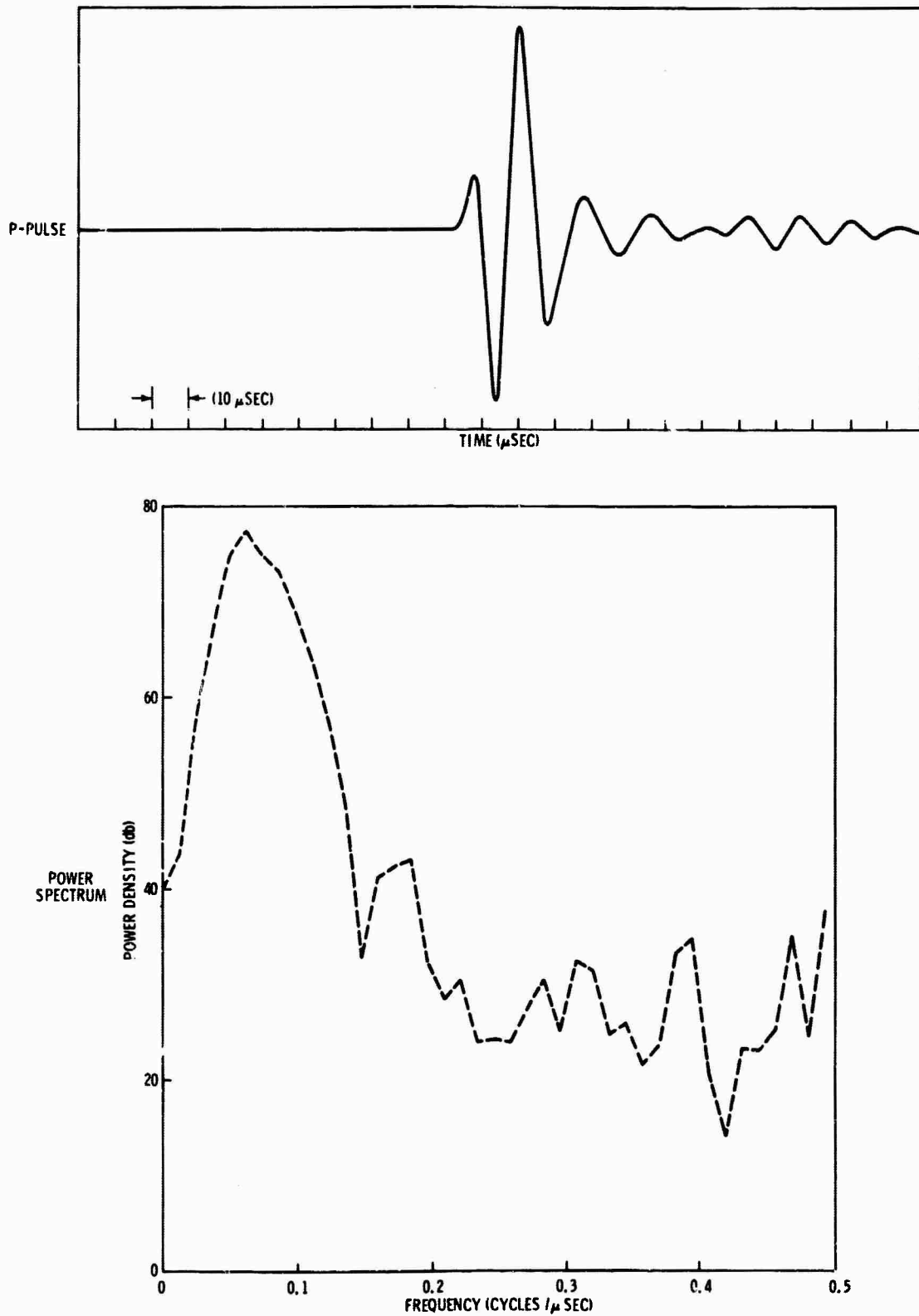
science services division

Figure III-36. P-Pulse Waveform and Power Spectrum Observed in the Steel Half-Space of Model H-6
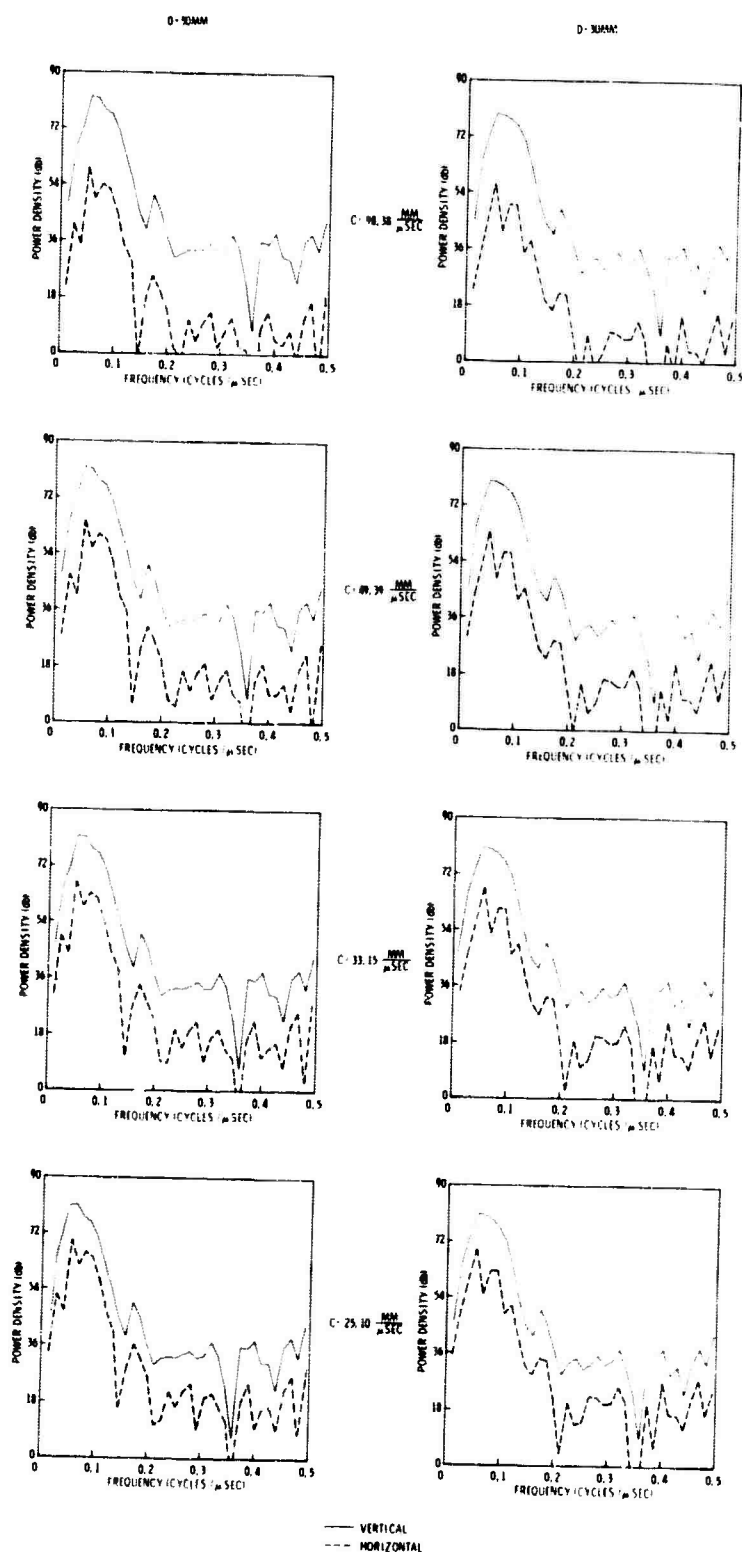
Figure III-37. Horizontal and Vertical Power Density Spectra for Four Phase Velocities for the 30-mm and 50-mm Crusts of Table III-1 (Spectra shaped by the P pulse observed in model H-6)

science services division

Such a conclusion suggests the epoxy bond in the model might cause significant conversion in the model P wave, which must be considered. Amplitude spectra (Figure III-38) were therefore developed for the crustal models defined in Table III-3.

It is evident that the epoxy bond, even if thinner than assumed here, can exert appreciable influence on the magnitude of the spectral peaks. However, the frequency dependence of the peaks remains relatively stable. The black spectra of Figure III-37 have been Fourier transformed to yield the synthetic seismograms of Figure III-39. The first portion of these time traces agrees well with the experimental time traces (Figure III-40), while the latter part of the records does not compare as favorably. This is consistent with the possibility of a disparity between the theoretical P-S conversion efficiency and the experimental time traces.

Finally, the experimental amplitude spectra were whitened by application of the inverse P-pulse spectrum to eliminate the adverse source-receiver spectral influence and isolate the fine structure caused by crustal reverberation. The whitened experimental spectra are presented in Figure III-41. Only the frequency band between about 0.04 and 0.2 cycle/μsec is pertinent, as this frequency interval contained all of the power in the source P pulse. The flat appearance of the whitened experimental spectra for the 50-mm crust suggests that the reverberatory character of the theoretical data is not present. This conclusion is consistent with the appearance of the experimental time traces (Figures III-26 and III-27) and the presence of the lateral discontinuity.

science services division

Figure III-38. Horizontal and Vertical Amplitude Spectra for Two Phase Velocities Observed by a Surface Receiver on the 30-mm and 50-mm Crustal Models of Table III-3

science services division

Table III-3

ELASTIC PARAMETERS FOR MODEL H-6
WITH EPOXY BOND INCLUDED

Layer	Compressional Velocity, α (mm/μsec)	Shear Velocity, β (mm/μsec)	Density (gm/cm^3)	Thickness (mm)
1 (Brass)	3.91	2.09	1.0	30
2 (Epoxy)	2.7	1.5	0.5	0.25
Half-space (Steel)	5.24	3.10	1.0	∞
1	3.91	2.09	1.0	50
2	2.70	1.50	0.5	0.25
Half-space	5.24	3.10	1.0	∞
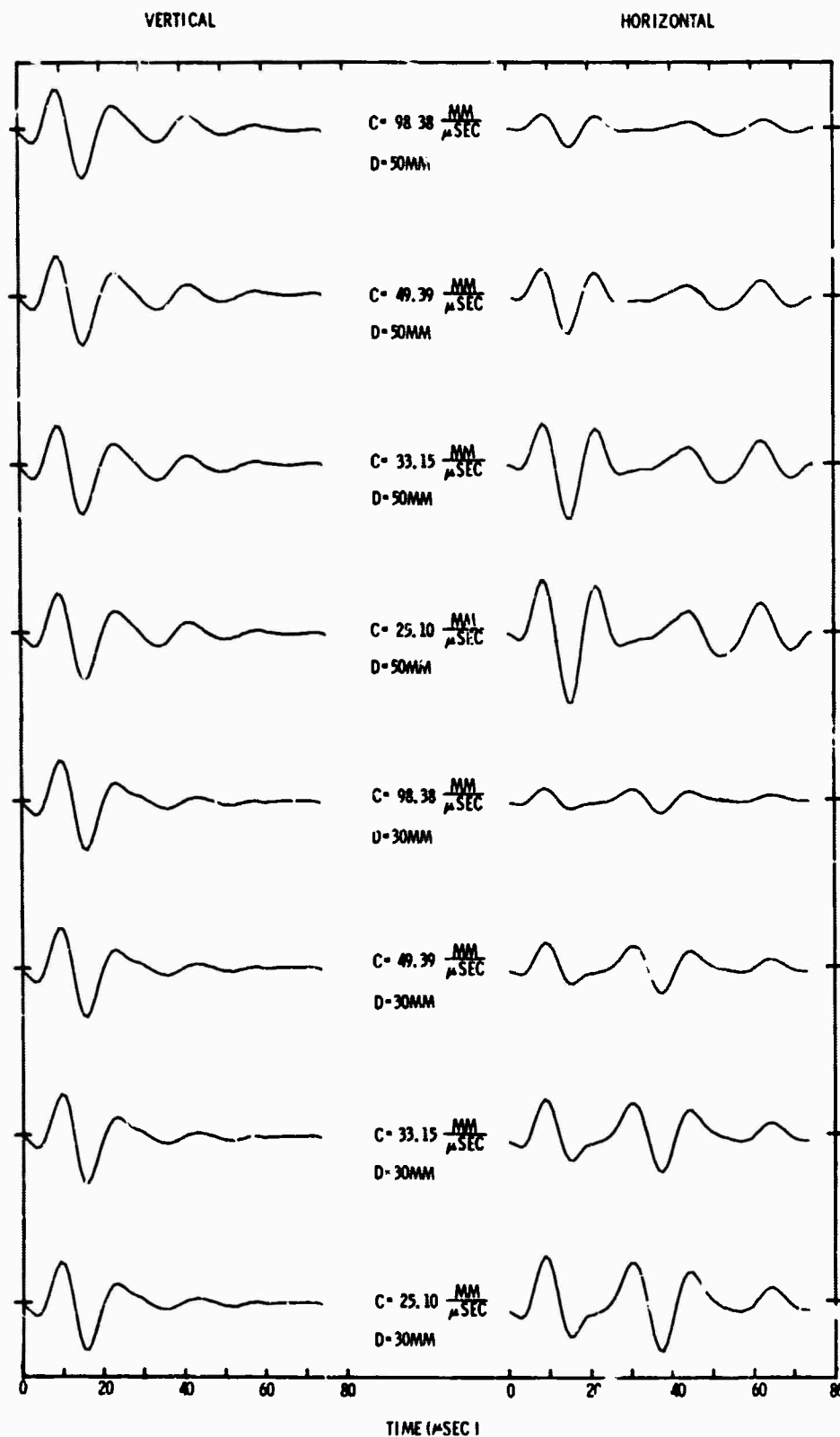
Figure III-39. Theoretical Seismograms for Four Phase Velocities for the 30-mm and 50-mm Crusts of Table III-1 (Spectra shaped by P pulse of model H-6)

science services : 'vision
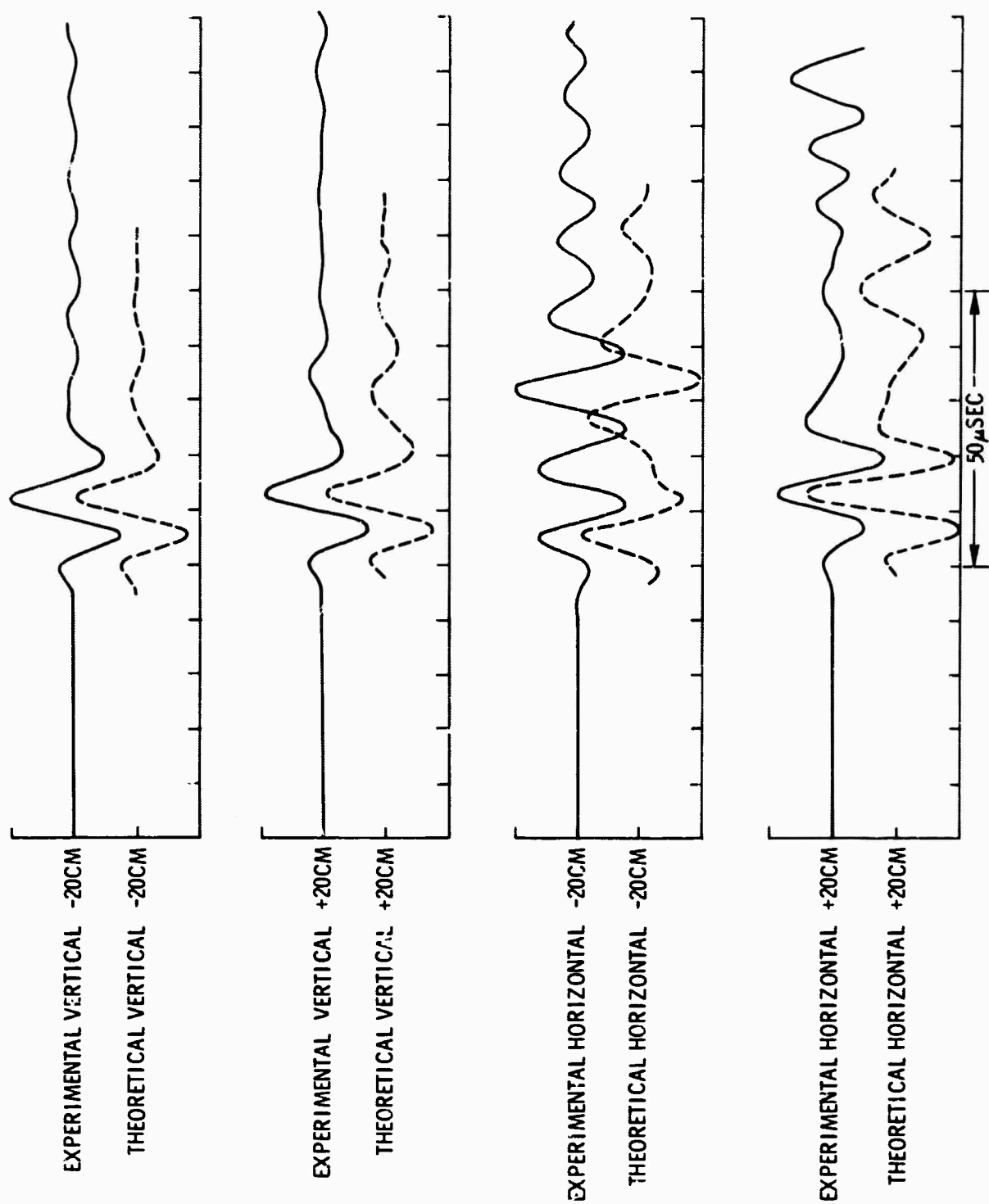
Figure III-40. Experimental and Black Theoretical Time Traces. (-20 and +20 cm correspond to a phase velocity of 25 mm/µsec)
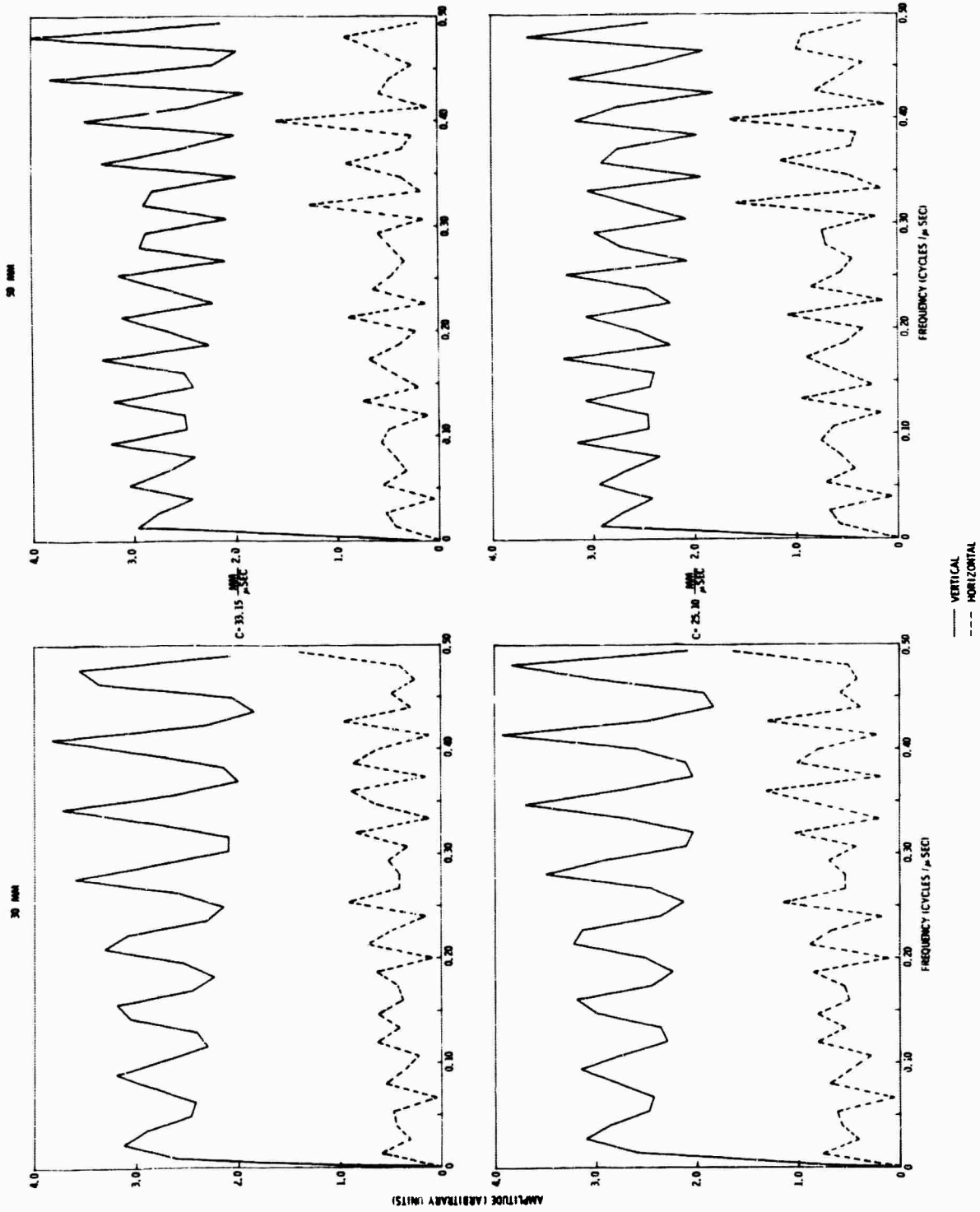
science services division
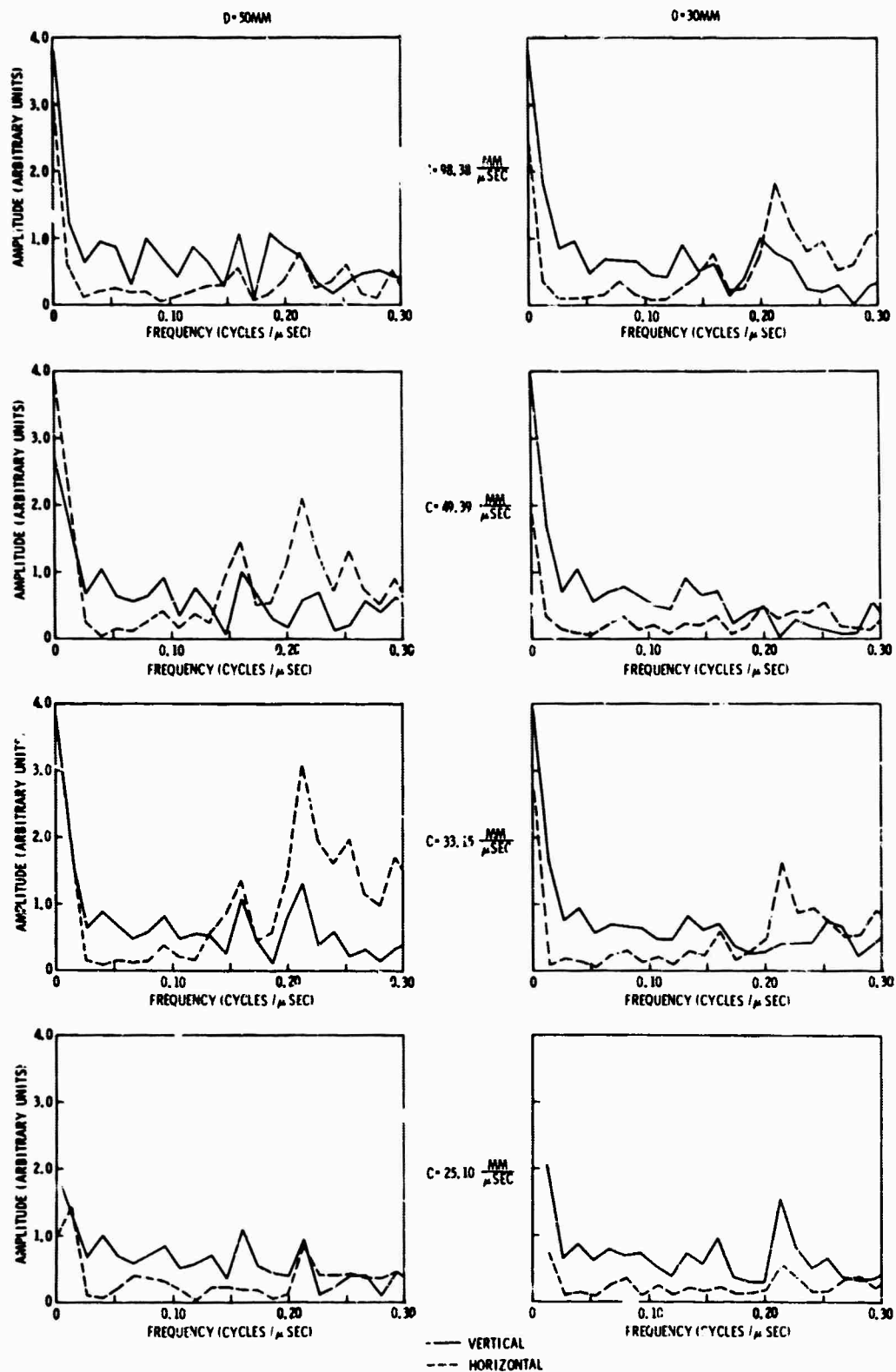
Figure III-41. Whitened Horizontal and Vertical Amplitude Spectra for Four Phase Velocities Observed by a Surface Receiver on the 30-mm and 50-mm Layers of Model H-6

SECTION IV

REFERENCES

1. Texas Instruments Incorporated, 1967: Continuation of Basic Research in Crustal Studies Annual Rpt., Contract AF 49(638)-1588.

2. Steinhart, John S. and Robert P. Meyer, 1961: Explosion Studies of Continental Structure, Carnegie Inst. of Wash., Publication 622, Washington, D.C.

3. Laster, Stanley J. and A. Frank Linville, 1966: Application of Multi-channel Filtering to the Separation of Dispersive Modes of Propagation, J. Geophys. Res., v. 71, n. 6, p. 1699-1701.

4. Knopoff, L. et al, 1966: Structure of the Crust and Upper Mantle in the Alps from the Phase Velocity of Rayleigh Waves, Bull. Seism. Soc. Am., v. 56, n. 5, Oct., p. 1009-1044.

5. Laster, Stanley J., Joe G. Foreman, and A. Frank Linville, 1965: Theoretical Investigation of Modal Seismograms for a Layer Over a Half-Space, Geophys. v. XXX, n. 4, Aug., p. 571-596.

6. Embree, Peter, J. B. Burg, and Milo M. Backus, 1963: Wideband Velocity Filtering — the Pie Slice Process, Geophys., v. XXVIII, n. 6, Dec., p. 948-974.

7. Hudson, J. A. and L. Knopoff, 1967: Statistical Properties of Rayleigh Waves Due to Scattering by Topography, Bull. Seism. Soc. Am., v. 57, n. 1, Feb., p. 83-90.

8. Tatel, Howard E. and Merle A. Tuve, 1955: Seismic Exploration of a Continental Crust, Geol. Soc. Am., Spec. Paper 62, p. 35-50.

APPENDIX

SUMMARY OF CRUSTAL STUDIES
ANNUAL REPORT, JANUARY 1967

APPENDIX

This annual technical report deals with work performed during the period 1 Janaury 1966 to 31 December 1966. The work was divided into two major areas. Section II is a discussion of mode theory and its applications, and scattering due to inhomogeneities is discussed in Section III.

A. MODE THEORY AND APPLICATION

Applications of theoretical computations which lead to modal seismograms for a given section of the earth are discussed in this report.

Theoretical crustal models were constructed for the Tonto Forest Seismological Observatory (TFO) and for the Large Aperature Seismic Array (LASA). The model used for TFO consisted of four layers and a half-space. The 5-layer model crust for LASA is based on measurements of Steinhart and Meyer.[1]

A long-period event with epicenter in Southern California recorded at TFO was time-partitioned, and the Rayleigh wave dispersion in the frequency range 0.025 to 0.17⁻ ⁻ⁿs was derived. Theoretical and experimental dispersion curves were compared at these frequencies. The model was perturbed slightly, and no significant changes resulted.

Theoretical computations predict that 10 higher-order normal modes may be expected in the TFO crust for frequencies up to 1.0 cps, and their amplitudes will be relatively small compared to the amplitude of M_{11}. The long period field recordings available were band-limited in such a manner that only the two lowest order modes may be observed.

Mode separation processors were designed and applied to separate the M_{21} mode from the M_{11} mode in the frequency range 0.0 to 0.25 cps using a TFO event whose epicenter was in Jalisco, Mexico. Two array processing schemes were used for mode separation. The first makes use of the frequency-velocity and amplitude relationships, and the second makes additional use of the 2-component (horizontal-vertical) relationships.

The theoretically computed mode separation processors did not reject the dominant M_{11} mode as much as was predicted by the computed filter response. Further investigation of the Jalisco event revealed that the Rayleigh mode had anomalous f-k characteristics; i.e., the Rayleigh mode dispersion estimates computed between various pairs of stations were inconsistent.

B. SCATTERING STUDIES

Analog models may be used in order to verify the theory and understanding of elastic wave propagation. In addition, these laboratory studies, although somewhat idealized, can be performed to give insight into the nature of practical geophysical problems.

Scattering studies were performed using an anlog model having a crustal layer with an abrupt thickness change (transition zone). There is a well developed leaking mode (PL_{22}) propagating in the thin end. Theory indicates that this PL_{22} mode in the thin end approximately corresponds to the PL_{23} mode in the thick end.

The shear mode portion of the recording shows a definite decrease in velocity occurring just past the transition zone. Theoretical dispersion curves show that if M_{21} on the thin end is scattered into M_{21} on the thick end, a decrease in phase velocity at each frequency results. Frequency-wavenumber analysis was used in an attempt to measure this velocity change.

DOCUMENT CONTROL DATA - R & D

(Security classification of title, body of abstract and indexing annotation must be entered when the overall report is classified)

1. ORIGINATING ACTIVITY (Corporate author)	2a. REPORT SECURITY CLASSIFICATION
Texas Instruments Incorporated	UNCLASSIFIED
Sciences Services Division	2b. GROUP
P. O. Box 5621, Dallas, Texas 75222	

3. REPORT TITLE

CONTINUATION OF BASIC RESEARCH IN CRUSTAL STUDIES, FINAL REPORT

4. DESCRIPTIVE NOTES (Type of report and inclusive dates)

Scientific - Final

5. AUTHOR(S) (First name, middle initial, last name)

Miller, Max K.
Harris, Hugh K.
Linville, A. Frank

6. REPORT DATE	7a. TOTAL NO. OF PAGES	7b. NO. OF REFS
15 July 1967	116	8

8a. CONTRACT OR GRANT NO.	9a. ORIGINATOR'S REPORT NUMBER(S)
AF 49(638)-1588	ARPA Order No. 292
b. PROJECT NO.	Amendment 20
c. 8652	9b. OTHER REPORT NO(S) (Any other numbers that may be assigned this report)
d. 625061R	AFOSR 67-1581

10. DISTRIBUTION STATEMENT

Distribution of this document is unlimited. .

11. SUPPLEMENTARY NOTES	12. SPONSORING MILITARY ACTIVITY
	Air Force Office of Scientific Research (SRPG), 1400 Wilson Blvd., Arlington, Va. 22209

13. ABSTRACT

The final report of work performed under the Crustal Studies Contract AF 49(638)-1588 is divided into two main areas: (1) theoretical dispersion calculations and experimental measurements of the fundamental Rayleigh wave at the Large Aperture Seismic Array (LASA) in Montana, and (2) a study of teleseismic signals using analog model data. Two earthquakes recorded on the long-period seismometers at LASA, were used for dispersion analysis. Epicenters of these two events were located off the northern California coast and in the Greenland Sea. Good agreement in the dispersion estimates was obtained using three recording stations. The significance of the results, which covered a frequency band of 0.025 through 0.0625 cps, lies in the fact that this frequency band is, theoretically, where the greatest dispersion occurs. The results obtained agree qualitatively with previously known results. An analog model having a crustal layer with an abrupt thickness change (3 to 5 cm) was used for studies of surface-wave scattering from surface irregularities and a lateral inhomogeneity. The analysis of surface-wave scattering was a continuation of work previously done. The model also was used for a study of teleseismic signals by placing the source crystal on the bottom of the model. For an upcoming-plane P wave, reverberation effects, the lateral inhomogeneity (including the expected focusing of energy into the thick end by the dipping segment of the crustal layer), and P- and S-wave conversions at the crustal layer interface caused a complex interference pattern that was observed on the surface recordings.

DD FORM 1473
1 NOV 65

14. KEY WORDS	LINK A		LINK B		LINK C	
	ROLE	WT	ROLE	WT	ROLE	WT
Theoretical dispersion calculations						
Rayleigh wave dispersion at LASA						
Long-period seismometers						
Analog model of a crustal layer having a lateral inhomogeneity						
Surface-wave scattering						
Teleseismic signals						
Reverberation effects						